Dilaton-Axion Wormhole Partition Function Away from the BPS Endpoint *

Soo-Jong Rey

Kwangwoon University, Seoul 01897 Korea

sjrey@kw.ac.kr

hexagon:2611.00960v1

Abstract

I determine the leading finite-radius correction to the two-boundary response of a charged axion wormhole near its BPS endpoint. With $\delta = a_*^2$, exact radial matching in a product axion–dilaton/saxion system gives a boundary eigenvalue that vanishes as $O(\delta)$ and an off-diagonal Hessian entry of order $O(\delta^2)$. Their combination produces a cross-boundary covariance linear in δ, with a negative first sub-leading correction on the branch studied here. I determine the semiclassical range in which the quadratic approximation remains controlled and identify the first finite-radius angular resonance, $\delta^2 \log(\delta/\delta_0)$. Under a uniform rescaling of all active charges, the coefficient of the linear cross-boundary response scales as the inverse square of the charge scale. I then average the inverse response over the chiral Gaussian ensemble describing the BPS endpoint. Boundary reduction preserves the hard-edge index. Multiplication by the matched BPS sector weight converts the normalized response into the leading finite-radius two-source coefficient.

Contents

1 Introduction **2**
- 1.1 Paper-I: the saddle and its physical fluctuations 4
- 1.2 Paper-II: the coefficient and its charge transform 5
- 1.3 Paper-III: the endpoint spectrum and its microscopic measure 5
- 1.4 This Paper: the finite-radius response 6

2 Geometry, boundary data, and the physical response **8**

3 Finite-radius response and its range of validity **10**
- 3.1 Linear response from exact radial matching 10
- 3.2 Angular matching and the semiclassical interval 11

4 Charge dependence and endpoint spectral response **12**
- 4.1 Charge dependence across sectors 12
- 4.2 Endpoint spectral response 13

5 Outlook **14**

*https://doi.org/10.5281/zenodo.23396648

A Boundary data and the physical quadratic problem **16**
A.1 Notation, domains, and regulators 16
A.2 Boundary conditions and source coefficients 17
A.3 Constraint reduction and Gaussian integration 19

B Finite-radius expansion and boundary Hessians **22**
B.1 Local coefficients, matching, and finite elimination 22
B.2 One radial region and its value-to-momentum map 24
B.3 Gaussian gluing for one harmonic 25
B.4 Assembly, functional determinants, and the full source coefficient 26
B.5 Further boundary elimination 28
B.6 Charge sensitivities of the radial problem 30
B.7 The deformation and the observable 31

C Exact radial solution and validity of the expansion **33**
C.1 Fixed-charge action at the minimal three-sphere 33
C.2 Small-radius background expansion 37
C.3 Product axion–dilaton/saxion model and boundary covariance 41
C.4 Cubic and quartic corrections 46
C.5 Range of the quadratic approximation 50
C.6 Coupled angular modes and radial resonance 54
C.7 Exact angular matching and the gravity mode 58

D Charge structure and endpoint spectrum **64**
D.1 Charge dependence 64
D.2 BPS matrix ensemble and finite-radius correction 68

E Statistics and bulk spectrum **73**
E.1 Spectral averages and microscopic measure 73
E.2 Large-matrix limit and spectral correlations 76

F Finite matrix identities **80**

1 Introduction

The finite-radius axion-wormhole branch departs from a fixed-charge BPS instanton. A nonzero minimal radius couples the boundary data across the wormhole interior and generates a connected response between the two asymptotic ends [1]. I determine the onset of this response, convert it into the corresponding fixed-charge source coefficient, and carry that coefficient into the axion-angle representation of the wormhole partition function.

I parameterize the saddle family by

$$\delta = a_*^2,$$

where a_* is the radius of the minimal three-sphere. I hold the axion charge $\boldsymbol{\nu}$ and the right asymptotic dilaton/saxion data fixed. Smooth continuation through the interior then determines the left asymptotic data. For one homogeneous fluctuation transverse to the background trajectory, let

$$q = (q_L, q_R)^T \tag{1.1}$$

[1] I use the terms *asymptotic boundary*, *minimal three-sphere*, and *wormhole interior* throughout. These correspond to "mouth," "neck," and "throat," respectively, in the literature.

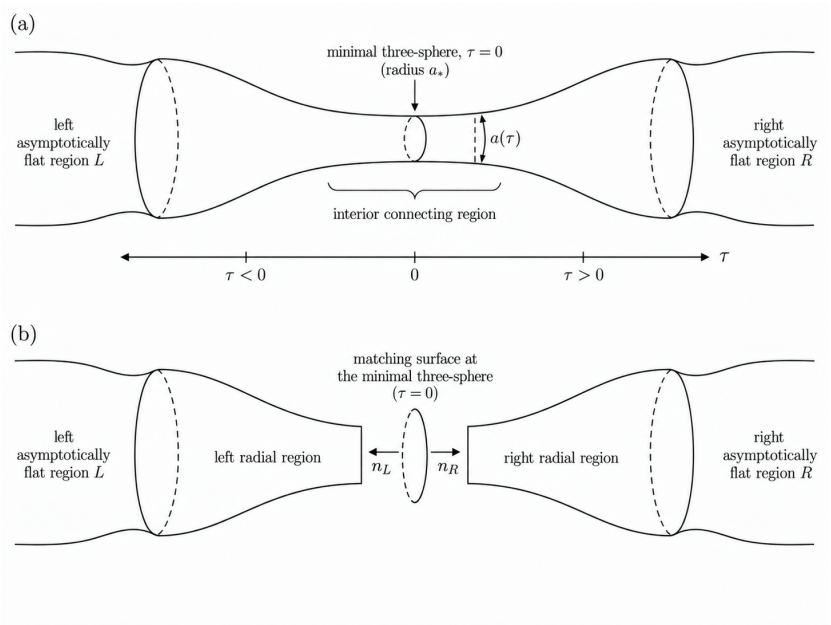


Figure 1: *Geometry and radial split of the bipartite wormhole used in the calculation. Panel (a) depicts a Euclidean wormhole with left and right asymptotically flat regions joined through the interior and a minimal three-sphere of radius a_* at the reflection-symmetric point $\tau = 0$. Panel (b) depicts the split at $\tau = 0$ into left and right radial regions; $\mathbf{n}_L$ and $\mathbf{n}_R$ are the outward normals at the matching surface.*

denote its two boundary values. The reduced on-shell action and the connected boundary covariance take the form

$$I^{(2)}_{\rm on} = \frac{A}{2} q^T K(\delta) q, \qquad G(\delta) = A^{-1} K(\delta)^{-1}, \tag{1.2}$$

with $A > 0$. Exact radial matching in the product axion–dilaton/saxion system gives

$$K_{LL} = O(\delta), \qquad K_{RR} = O(1), \qquad K_{LR} = O(\delta^2). \tag{1.3}$$

One eigenvalue of K therefore vanishes linearly with δ, while the second approaches a positive constant. The inverse soft eigenvalue supplies one power of δ^{-1} and yields

$$G_{LR}(\delta) = g_{1,\boldsymbol{\nu}}\delta + g_{2,\boldsymbol{\nu}}\delta^2 + O(\delta^3). \tag{1.4}$$

For the subcritical product branch studied here,

$$g_{1,\boldsymbol{\nu}} > 0, \qquad g_{2,\boldsymbol{\nu}} < 0. \tag{1.5}$$

The cross-boundary response consequently rises linearly from the BPS endpoint and bends downward at first sub-leading order. The boundary response therefore detects the opening wormhole interior before it is visible in the fixed-radius outer metric: the connected left–right susceptibility begins at $O(\delta)$, whereas the outer geometry first changes at $O(\delta^2)$.

Matched asymptotics fixes this power counting. At fixed outer radius, the metric departs from the BPS profile at $O(\delta^2)$. In the inner coordinate $a = \sqrt{\delta}\,\rho$, the reduced action instead carries an overall factor of δ. Exact inner–outer matching transports this $O(\delta)$ contribution to the asymptotic boundary form. The boundary response therefore resolves the opening wormhole interior one order earlier than the fixed-radius metric expansion.

The $O(\delta)$ soft eigenvalue supplies the inverse factor δ^{-1} that converts the $O(\delta^2)$ mixed Hessian into an $O(\delta)$ cross-boundary response. The boundary response therefore detects the

opening wormhole interior before it is visible in the fixed-radius outer metric: the connected left–right susceptibility begins at $O(\delta)$, whereas the outer geometry first changes at $O(\delta^2)$.

Papers I–III establish the three endpoint ingredients used in this calculation. Paper-I constructs the physical fixed-charge BPS Hessian and factorizes it as

$$\mathcal{H}_{\boldsymbol{\nu},0} = \mathcal{Q}_{\boldsymbol{\nu}}^{\dagger}\mathcal{Q}_{\boldsymbol{\nu}}. \tag{1.6}$$

Paper-II organizes the coefficient sequence

$$C_{\boldsymbol{\nu}}^{ij} \xrightarrow{R_b} W_{\boldsymbol{\nu}}[b] \xrightarrow{\sum_{\boldsymbol{\nu}} e^{i\boldsymbol{\nu}\cdot\boldsymbol{\theta}}} Z_{\mathrm{wh}}(\boldsymbol{\theta}; b). \tag{1.7}$$

Paper-III identifies the nonzero endpoint spectrum with squared singular values and supplies its Laguerre/chiral hard-edge measure. These results fix the endpoint operator, the boundary reduction, and the endpoint spectral statistics. The present paper computes the finite-radius deformation that joins them.

I first solve the homogeneous boundary problem through the first subleading order and determine the semiclassical range of the quadratic response. I then derive the first angular resonance, the charge dependence of the linear coefficient, and the spectral average of the inverse response. Matching the complete fixed-sector measure to its finite BPS weight converts the covariance slope into the leading unnormalized two-source coefficient. The reduction data b then produce $W_{\boldsymbol{\nu}}[b]$, and the charge sum produces the dependence on the asymptotic axion angle.

1.1 Paper-I: the saddle and its physical fluctuations

Paper-I formulates the saddle at fixed conserved axion charge [1]. At fixed charge, the BPS instanton is the endpoint of the non-BPS wormhole branch. Physical fluctuations preserve the fixed charge. Varying the charge moves to another saddle. This distinction determines the fluctuation domain and the boundary terms in the variational problem.

Figure 1 shows the finite-radius geometry of the saddle and the radial split used below. Away from the BPS endpoint, the minimal radius $a_* > 0$ defines a smooth three-sphere at $\tau = 0$. Its extrinsic curvature vanishes, and the scale factor is reflection symmetric about this surface. The axion and dilaton/saxion profiles obey the charged radial equations and need not share this reflection symmetry. Splitting the smooth solution at $\tau = 0$ produces left and right radial regions with opposite outward normals. Their outward canonical momenta cancel when the two regions are joined.

Paper-I then constructs the physical Hessian at the BPS endpoint. The Hamiltonian constraint removes the redundant metric variable. Gauge fixing and the boundary conditions define the physical domain. Collective zero modes are removed from the determinant and treated separately. Linearization of the BPS equations on the remaining domain gives a first-order map $\mathcal{Q}_{\boldsymbol{\nu}}$. The physical Hessian is its adjoint square:

$$\mathcal{H}_{\boldsymbol{\nu},0} = \mathcal{Q}_{\boldsymbol{\nu}}^{\dagger}\mathcal{Q}_{\boldsymbol{\nu}}, \qquad \langle \eta, \mathcal{H}_{\boldsymbol{\nu},0}\eta\rangle = \|\mathcal{Q}_{\boldsymbol{\nu}}\eta\|^2. \tag{1.8}$$

Here $\boldsymbol{\nu}$ denotes the fixed charge sector and η denotes a physical perturbation. The adjoint is taken on the same boundary domain. Equation (1.8) makes the BPS quadratic form positive semidefinite and identifies its nonzero eigenvalues with squared singular values of $\mathcal{Q}_{\boldsymbol{\nu}}$. This factorization holds at the BPS endpoint.

I use this BPS operator as the endpoint reference for the finite-radius problem. The non-BPS solution changes the radial background, the radial interval, and the matching at the minimal three-sphere. I compute these changes explicitly in a product axion–dilaton/saxion system.

Paper-I also identifies where the two-end response enters the long-distance source operator. Each asymptotic boundary supports local source insertions. Eliminating the wormhole interior produces a quadratic coefficient for these sources. Expanding the total source over parent components gives the same-component and different-component terms of the same quadratic form. I compute the response between the left and right asymptotic boundaries before assigning the two insertions to parent components.

1.2 Paper-II: the coefficient and its charge transform

Paper-II organizes the wormhole amplitude in the charge representation before transforming to the asymptotic axion angle [2]. For each fixed charge vector $\boldsymbol{\nu}$, the saddle calculation produces a two-end coefficient matrix $C_{\boldsymbol{\nu}}^{ij}$ in the space of boundary insertions. A prescribed reduction R_b then converts this matrix into the scalar sector coefficient

$$C_{\boldsymbol{\nu}}^{ij} \xrightarrow{R_b} W_{\boldsymbol{\nu}}[b].$$

The data b specify the contractions, projections, insertions, source normalization, contour, and fields eliminated in this reduction. Only after this operation, I form the axion-angle representation,

$$Z_{\rm ax}(\boldsymbol{\theta}; b) = \sum_{\boldsymbol{\nu}} W_{\boldsymbol{\nu}}[b]\, \mathrm{e}^{i\boldsymbol{\nu}\cdot\boldsymbol{\theta}}. \tag{1.9}$$

The vector $\boldsymbol{\theta}$ is the compact Fourier variable conjugate to the quantized charge vector $\boldsymbol{\nu}$. Its phase factor in Eq. (1.9) is kinematic. The charge dependence generated by the saddle, fluctuations, measure, contour, and reduction resides in $W_{\boldsymbol{\nu}}[b]$.

This ordering separates properties of the two-end coefficient from properties of the final charge transform. Before reduction, a positive coefficient matrix constrains its mixed and diagonal source entries through quadratic-form inequalities. After reduction, the scalar sequence $W_{\boldsymbol{\nu}}[b]$ may be positive, signed, or complex. A positive sequence defines a charge probability law and obeys moment inequalities. A complex sequence retains its phase sector by sector in Eq. (1.9). The reduction therefore determines which analytic and positivity statements apply to the resulting wormhole partition function.

Paper-II also separates existence of the complexified coefficient from convergence of its charge sum. Complex continuation of $\boldsymbol{\theta}$ first defines a complexified boundary-value problem. The resulting coefficients must then decay sufficiently rapidly along the charge lattice for the Fourier series to converge. For several axions, this condition is directional in charge space. The dilute Bessel or Skellam form arises only after positivity, independent dilute events, charge symmetry, and unit-charge dominance have been imposed.

The present paper supplies the finite-radius input to this construction. I first compute the deformation of the physical two-boundary response in a fixed charge sector. For fixed boundary values, the quadratic action is governed by the boundary Hessian K. After Gaussian integration over those boundary variables, the connected source response is governed by K^{-1}. Multiplication by the complete fixed-sector weight gives the unnormalized two-end coefficient, and the Paper-II reduction R_b then produces $W_{\boldsymbol{\nu}}[b]$. Thus the finite-radius geometry is determined before the boundary reduction and before the charge transform in Eq. (1.9).

1.3 Paper-III: the endpoint spectrum and its microscopic measure

Paper-III resolves the BPS endpoint operator into its singular-value data [3]. For the fixed-charge physical Hessian

$$\mathcal{H}_{\boldsymbol{\nu},0} = \mathcal{Q}_{\boldsymbol{\nu}}^{\dagger}\mathcal{Q}_{\boldsymbol{\nu}},$$

the associated chiral double is

$$\mathcal{D}_{\boldsymbol{\nu}} = \begin{pmatrix} 0 & \mathcal{Q}_{\boldsymbol{\nu}}^{\dagger} \\ \mathcal{Q}_{\boldsymbol{\nu}} & 0 \end{pmatrix}, \qquad \mathrm{Spec}_{\neq 0}\, \mathcal{D}_{\boldsymbol{\nu}} = \{\pm s_j\}, \qquad \mathrm{Spec}_{\neq 0}\, \mathcal{H}_{\boldsymbol{\nu},0} = \{s_j^2\}. \tag{1.10}$$

The s_j are the nonzero singular values of $\mathcal{Q}_{\boldsymbol{\nu}}$. The adjoint-square structure pins the physical spectrum to the non-negative axis and makes zero a hard spectral edge. A small s_j^2 represents a weak restoring direction of the BPS quadratic form and enhances any inverse response with nonzero overlap onto that mode.

Paper-III represents this endpoint by a finite chiral ensemble that preserves the index, antiunitary class, and endpoint boundary form of the physical BPS map. For the central Gaussian representative, the squared singular values obey a Laguerre–Wishart law. Its microscopic scaling limit at zero is the corresponding Bessel hard-edge ensemble. The hard-edge index records the rectangular defect of the finite representation of the first-order map, while the Dyson class records its real, complex, or quaternionic structure. These data determine the local endpoint statistics used below.

The D(−1)/D3 ADHM system supplies the microscopic Type-IIB realization considered in Paper-III. Its bifundamental sector contains a rectangular first-order block, and singular-value reduction produces the same Laguerre structure. The matching to the gravitational endpoint is performed at the level of edge data. The axion charge $\boldsymbol{\nu}$, the ADHM instanton number, the rectangular defect, and the gravitational hard-edge index are distinct labels. A microscopic identification requires the charge dictionary, physical fluctuation domain, zero-mode quotient, hard-edge index, and antiunitary class to agree. The resulting ADHM/chiral-Wishart integral represents the microscopic fixed-sector contribution to the coefficient discussed in Paper-II.

Paper-III supplies the statistical law of the BPS endpoint spectrum in each fixed charge sector. The finite-radius deformation is a separate gravitational input. In the present paper, radial matching determines the deformed boundary matrix and the effective source vectors before the endpoint ensemble is averaged. The resulting inverse response depends on how these physical probes and the finite-radius deformation project onto the BPS endpoint eigenmodes. Paper-III therefore supplies the endpoint spectral statistics, while the present calculation determines the observable that probes them.

This separation also fixes the roles of the two Bessel structures inherited from Papers II and III. In Paper-II, modified Bessel functions arise in the dilute specialization of the charge-sector sum that constructs the axion-angle representation. In Paper-III, the Bessel kernel describes microscopic singular-value correlations at the hard spectral edge within one fixed charge sector. The first belongs to the sum over charge sectors; the second belongs to the spectrum inside a sector. I keep these operations distinct throughout the finite-radius calculation.

1.4 This Paper: the finite-radius response

This paper computes the departure of the fixed-charge two-boundary response from its BPS endpoint. I work charge sector by charge sector and parameterize the non-BPS saddle family by

$$\delta = a_*^2.$$

I hold the conserved charge vector and the right asymptotic dilaton/saxion data fixed. Smooth continuation through the minimal three-sphere at $\tau = 0$ then determines the left asymptotic data. For each sector, I first compute the finite-radius boundary response, then apply the Paper-II reduction, and finally average the resulting response with the Paper-III endpoint measure. This sequence keeps the geometric deformation, the boundary reduction, and the endpoint spectral average as distinct operations.

The leading response is fixed by matched radial asymptotics. At fixed outer radius, the background metric first departs from its BPS profile at $O(\delta^2)$. Near the shrinking minimal three-sphere, the rescaling $a = \sqrt{\delta}\,\rho$ instead produces a reduced inner action proportional to δ. Exact radial matching carries this inner contribution to the asymptotic boundary quadratic form. For one homogeneous dilaton/saxion mode transverse to the background scaling trajectory, the boundary Hessian obeys

$$K_{LL} = a_1\delta + O(\delta^2), \qquad K_{RR} = r_0 + O(\delta^2), \qquad K_{LR} = b_2\delta^2 + O(\delta^3), \qquad a_1, r_0 > 0, \quad b_2 < 0.$$

One eigenvalue therefore softens linearly in δ, while the second approaches a finite positive limit. With $G = A^{-1}K^{-1}$, the connected cross-boundary covariance becomes

$$G_{LR}(\delta) = g_{1,\boldsymbol{\nu}}\delta + g_{2,\boldsymbol{\nu}}\delta^2 + O(\delta^3), \qquad g_{1,\boldsymbol{\nu}} > 0, \qquad g_{2,\boldsymbol{\nu}} < 0.$$

The inverse soft eigenvalue supplies the factor δ^{-1} that converts the $O(\delta^2)$ mixed Hessian into an $O(\delta)$ cross-boundary response. The exact radial solution fixes the first curvature of this response and makes it negative on the branch studied here. I impose the finite endpoint matching $Z_{\boldsymbol{\nu}}[0;\delta] \to Z_{\boldsymbol{\nu},0}$ for the complete fixed-sector weight. The corresponding unnormalized source coefficient then has the leading form

$$C^{LR}_{\boldsymbol{\nu}}(\delta) = \delta\, Z_{\boldsymbol{\nu},0} g_{1,\boldsymbol{\nu}} + o(\delta).$$

The same boundary formulation fixes the domain of this linear response. A fixed positive quadratic term in the soft boundary direction lifts the small eigenvalue to $O(1)$ and moves the cross-boundary covariance from $O(\delta)$ to $O(\delta^2)$. Cubic and quartic vertices control the opposite limit, where the growing soft-mode variance invalidates the Gaussian expansion. Together with the outer small-radius expansion, they define the semiclassical interval

$$\frac{C_{\mathrm{ctl}}}{A} \ll \delta \ll L^2.$$

Within this interval, the homogeneous mode gives the linear response above. The coupled angular problem contains a separate finite-radius effect. The first correction lowers the BPS radial weight by four units. The candidate resonances in the lower harmonics cancel under the compatibility condition, while the $\ell = 3$ branch connects the BPS indices 1 and -3 with nonzero projection. It therefore produces the first finite-radius logarithm,

$$\delta^2 \log(\delta/\delta_0). \tag{1.11}$$

Its first derivative vanishes at the BPS endpoint and leaves the linear homogeneous response unchanged. [2]

The leading geometric response has a simple charge scaling in the product system. For a uniform rescaling of all active charges, $\boldsymbol{\nu} \mapsto t\boldsymbol{\nu}$, the stationary target-space trajectory keeps the same shape and

$$g_{1,t\boldsymbol{\nu}} = t^{-2} g_{1,\boldsymbol{\nu}}.$$

Changing the relative charge magnitudes instead moves the stationary trajectory. I determine that response by differentiating the background equations, the fluctuation operator, and the

[2] Kehagias and Riotto [4] obtain logarithmic scalar running near the Euclidean AdS boundary from a Gauss–Bonnet tadpole and verify the Kontsevich–Segal–Witten allowability of their complex background metric. Their logarithm belongs to the asymptotic background solution, whereas the logarithm here arises from a finite-radius fluctuation resonance about the near-BPS wormhole. Both admit a radial-resonance organization and a finite-part prescription. The exact radial transformation used here maps the near-BPS fluctuation equation to an asymptotically AdS form and provides a common analytic representation of the resonance. The two gravitational saddles and their partition functions remain distinct.

source map at fixed asymptotic data. These charge-sensitivity equations propagate the change of charge composition into the finite-radius boundary coefficient.

I finally combine this deterministic deformation with the Paper-III endpoint ensemble. The physical boundary reduction first fixes the endpoint matrix $M_{0,\boldsymbol{\nu}}$, its finite-radius perturbation $D_{1,\boldsymbol{\nu}}$, and the effective source vectors. The inverse response then satisfies

$$\frac{d}{d\delta} M_{\boldsymbol{\nu}}(\delta)^{-1}\Big|_{\delta=0} = -M_{0,\boldsymbol{\nu}}^{-1} D_{1,\boldsymbol{\nu}} M_{0,\boldsymbol{\nu}}^{-1}.$$

Small endpoint eigenvalues therefore enhance the finite-radius response according to their overlap with the deformation and the physical sources. For the central chiral Gaussian representative, eliminating the unobserved columns produces another Wishart matrix with the same rectangularity. The boundary projection therefore preserves the hard-edge index. The resulting negative moments determine the spectral averages of the determinant and inverse response, together with their hard-edge integrability conditions.

The appendices derive the fixed-charge quadratic functional, the boundary Schur complements, the exact homogeneous and angular matching, the interaction bounds, the charge sensitivities, and the endpoint spectral averages.

2 Geometry, boundary data, and the physical response

I describe the finite-radius saddle in proper radial distance τ, with the minimal three-sphere at $\tau = 0$. The metric takes the form

$$ds^2 = \mathrm{d}\tau^2 + a(\tau)^2 \mathrm{d}\Omega_3^2, \qquad \delta = a_*^2, \qquad E = 12\delta^2, \tag{2.1}$$

where $a_* = a(0)$ is the minimum of the scale factor. The radial first integral gives

$$(a')^2 = 1 - \frac{\delta^2}{a^4}, \qquad a(-\tau) = a(\tau).$$

Thus the metric is reflection symmetric and the minimal three-sphere is totally geodesic. The charged matter profile follows its own radial equations. Its scalar momentum at $\tau = 0$ is generally nonzero. Cutting the smooth saddle at this surface produces left and right radial problems with opposite outward normals. Continuity of the fields together with cancellation of the two outward canonical momenta reconstructs the complete two-boundary solution.

I formulate this family at fixed axion charge. After Legendre transforming the axions, the fixed-charge Routhian contains the dilaton/saxion potential $U_{\boldsymbol{\nu}}(\phi)$. The dilaton/saxions evolve in this potential on the radial geometry set by $a(\tau)$. I vary δ while holding $\boldsymbol{\nu}$ and the right asymptotic dilaton/saxion data fixed. Smooth continuation through $\tau = 0$ then determines the left asymptotic values. Their δ dependence contributes the canonical boundary work to the derivative of the on-shell action. All finite-radius derivatives below are taken along this fixed-charge saddle family.

The metric symmetry and the matter boundary problem play different roles. At $\tau = 0$, $a' = 0$, while the scalar first integral fixes the allowed scalar momentum through the charge potential. A smooth charged profile can therefore cross the minimal sphere with nonzero scalar derivative. Parity decomposition of the fluctuations requires reflection symmetry of the complete fluctuation operator and its boundary domain. I instead impose continuity of the fluctuation fields and match their canonical momenta directly across the minimal sphere.

The small-radius expansion contains an outer region and an inner region with different power counting. At fixed outer radius,

$$\frac{\delta^2}{a^4} \ll 1,$$

so the metric first departs from its BPS profile at $O(\delta^2)$. Near the minimal three-sphere I set

$$a = \sqrt{\delta}\,\rho.$$

Then $\delta^2/a^4 = \rho^{-4}$ remains finite, while the reduced inner action acquires an overall factor of δ. The inner problem therefore generates an $O(\delta)$ contribution to the boundary quadratic form. Exact radial matching carries this contribution through the overlap region to the asymptotic boundaries.

This matched expansion defines the derivative at the BPS endpoint. For fixed outer radius, the solution approaches the BPS profile as $\delta \to 0$. For fixed $\rho = a/\sqrt{\delta}$, the inner solution retains a nontrivial finite profile. Their common overlap transfers the shrinking-interior dynamics to the asymptotic response. The resulting boundary variation contains both the deformation of the bulk trajectory and the induced motion of the left asymptotic data.

I next reduce the quadratic problem to its physical boundary variables. At fixed charge, I impose the Hamiltonian constraint and fix the gauge before eliminating the remaining auxiliary and interior fields. For a real bosonic quadratic form written in retained and eliminated coordinates,

$$\frac{1}{2}\begin{pmatrix} x \\ u \end{pmatrix}^T \begin{pmatrix} A & B \\ B^T & D \end{pmatrix} \begin{pmatrix} x \\ u \end{pmatrix}, \qquad D^{-1} \text{ defined},$$

stationarity in u gives the effective boundary Hessian

$$A - BD^{-1}B^T.$$

I use this Schur-complement reduction throughout the finite-radius calculation.

The radial split at $\tau = 0$ provides an equivalent construction. I evaluate the left and right on-shell actions as functions of their common matching value and add them. Extremizing this sum over the matching value imposes canonical-momentum matching and reproduces the smooth full saddle. Eliminating the matching variable before or after assembling the two radial regions gives the same physical outer-boundary functional. The matching surface is therefore an intermediate device; the final boundary Hessian acts on the asymptotic source variables.

For one homogeneous dilaton/saxion mode transverse to the background scaling trajectory, let q_L and q_R denote its asymptotic boundary values. I collect them into

$$q = (q_L, q_R)^T$$

and define the physical boundary Hessian K and connected covariance G by

$$I^{(2)}_{\rm on} = \frac{\mathcal{A}}{2} q^T K q, \qquad q = (q_L, q_R)^T, \qquad G = \mathcal{A}^{-1} K^{-1}. \tag{2.2}$$

Here $\mathcal{A} > 0$ is the overall normalization inherited from the reduced action. The diagonal entries K_{LL} and K_{RR} measure the quadratic cost of fixing each asymptotic value, while K_{LR} measures their coupling in the fixed-boundary action.

I first solve the Dirichlet problem with q_L and q_R fixed. I then integrate these boundary variables with the Lebesgue measure specified by the source functional and with linear sources. Completing the Gaussian square gives

$$\frac{1}{2\mathcal{A}} J^T K^{-1} J$$

in the source exponent. Two source derivatives therefore give G. The distinction is essential: K_{LR} is the mixed coefficient of the fixed-boundary on-shell action, whereas G_{LR} is the connected left–right response after the boundary variables have been integrated.

The boundary state forms part of this observable. Adding a positive quadratic boundary term shifts K by a positive matrix and changes G, while leaving the interior Dirichlet solution unchanged. I therefore use one fixed boundary measure and one fixed boundary state when comparing charge sectors and when forming the subsequent axion-angle representation.

Appendix A defines the fixed-charge source functional, fluctuation domain, and Gaussian reduction. Appendix B constructs the radial value-to-momentum maps, glues the two radial regions, and derives the physical boundary Hessian. Appendix C solves the product axion–dilaton/saxion model and performs the exact radial and angular matching.

3 Finite-radius response and its range of validity

3.1 Linear response from exact radial matching

I now evaluate the finite-radius response in the product axion–dilaton/saxion system. For p axions with canonically normalized dilaton/saxions ϕ_i, the fixed-charge potential is

$$U_{\boldsymbol{\nu}}(\phi) = \sum_i \nu_i^2 \exp(2\beta_i \phi_i), \qquad \beta_i > 0.$$

Introduce

$$\beta^{-2} = \sum_i \beta_i^{-2}, \qquad n_i = \frac{\beta}{\beta_i}, \qquad \phi_i = n_i \sigma + E_{iu} s^u,$$

where the columns of E form an orthonormal basis orthogonal to n. The field σ follows the common scaling direction, while the $p-1$ fields s^u describe relative dilaton/saxion displacements. In these variables,

$$U_{\boldsymbol{\nu}} = \exp(2\beta\sigma) V_{\boldsymbol{\nu}}(s).$$

The stationary transverse trajectory satisfies $\partial_u V_{\boldsymbol{\nu}} = 0$. At this point the normalized transverse Hessian is

$$\frac{\partial_u \partial_v V_{\boldsymbol{\nu}}}{V_{\boldsymbol{\nu}}} = 4\beta^2 \delta_{uv}.$$

Thus every homogeneous transverse direction obeys the same radial equation on the product background. I work on the subcritical branch

$$0 < \sqrt{3}\,\beta < 1.$$

Let q_L and q_R denote the asymptotic values of one transverse mode. These boundary values displace the dilaton/saxions away from their stationary relative configuration. Solving the radial equation with (q_L, q_R) fixed and evaluating the outward canonical momenta determines the boundary Hessian K of Eq. (2.2). The exact solution gives

$$K_{LL} = a_1 \delta + O(\delta^2), \qquad K_{RR} = r_0 + O(\delta^2), \qquad K_{LR} = b_2 \delta^2 + O(\delta^3), \tag{3.1}$$

with

$$a_1 > 0, \qquad r_0 > 0, \qquad b_2 < 0.$$

The couplings, charge vector, and asymptotic data determine these coefficients; Appendix C gives their closed forms. The unequal powers in K_{LL} and K_{RR} follow from the boundary prescription: the right asymptotic data remain fixed along the saddle family, whereas the left data are determined by smooth continuation. The metric itself remains reflection symmetric.

Equation (3.1) contains the mechanism of the leading response. Its determinant is

$$\det K = a_1 r_0 \delta + O(\delta^2),$$

so one eigenvalue softens linearly in δ while the other tends to r_0. Since

$$(K^{-1})_{LR} = -\frac{K_{LR}}{\det K},$$

the connected covariance becomes

$$G_{LR} = g_{1,\boldsymbol{\nu}}\delta + g_{2,\boldsymbol{\nu}}\delta^2 + O(\delta^3), \qquad g_{1,\boldsymbol{\nu}} = -\frac{b_2}{\mathcal{A}a_1 r_0} > 0, \qquad g_{2,\boldsymbol{\nu}} < 0. \tag{3.2}$$

The $O(\delta)$ soft eigenvalue supplies the inverse factor δ^{-1} that converts the $O(\delta^2)$ mixed Hessian into an $O(\delta)$ cross-boundary covariance. The exact radial solution also fixes the first subleading coefficient. Its negative sign makes the response bend downward as the wormhole opens away from the BPS endpoint.

The same solution fixes the sign and regularity of the quadratic form. For sufficiently small positive δ,

$$K_{LL}K_{RR} - K_{LR}^2 > 0,$$

and hence K is positive in this transverse sector. Together with $b_2 < 0$, this gives $G_{LR} > 0$. Direct differentiation of the exact on-shell action reproduces the same canonical momenta and the same boundary Hessian.

The linear law in Eq. (3.2) also exposes the role of the boundary state. The soft contribution to the on-shell action begins as

$$\frac{\mathcal{A}a_1}{2}\,\delta q_L^2.$$

Adding a fixed positive quadratic boundary term for q_L lifts this soft eigenvalue to a finite constant. The mixed entry remains $O(\delta^2)$, while the determinant acquires a nonzero endpoint limit. The corresponding cross-boundary covariance then begins at $O(\delta^2)$. The $O(\delta)$ law therefore follows from the soft boundary direction specified by the source functional used here.

The normalized covariance is only one factor in the unnormalized two-source coefficient. Let $Z_{\boldsymbol{\nu}}[0;\delta]$ denote the complete zero-source sector weight, including the determinant or Pfaffian factors, exact-mode insertions, collective-coordinate measure, boundary normalization, and the remaining fluctuation sectors. I impose the BPS matching condition

$$Z_{\boldsymbol{\nu}}[0;\delta] \longrightarrow Z_{\boldsymbol{\nu},0} \qquad (\delta \to 0^+).$$

Then

$$C_{\boldsymbol{\nu}}^{LR}(\delta) = \delta B_{\boldsymbol{\nu}} + o(\delta), \qquad B_{\boldsymbol{\nu}} = Z_{\boldsymbol{\nu},0}\, g_{1,\boldsymbol{\nu}}. \tag{3.3}$$

The finite limit belongs to the complete fixed-sector measure. The isolated two-variable bosonic Gaussian contains the soft factor $\delta^{-1/2}$ and therefore does not furnish this matching by itself.

Since $G_{LR}(0) = 0$, continuity of the complete sector weight fixes the endpoint slope in Eq. (3.3). When $Z_{\boldsymbol{\nu}}[0;\delta]$ is differentiable, its first derivative enters only at $O(\delta^2)$, together with $g_{2,\boldsymbol{\nu}}$. Thus the leading coefficient factorizes into the BPS sector weight and the positive geometric response $g_{1,\boldsymbol{\nu}}$. Its phase is inherited entirely from $Z_{\boldsymbol{\nu},0}$. Equation (3.3) is the finite-radius input to the Paper-II reduction.

3.2 Angular matching and the semiclassical interval

The higher harmonics introduce a second finite-radius structure. For $\ell \geq 1$, I expand the fluctuations in scalar harmonics of the round three-sphere and retain the coupled axion–dilaton/saxion radial system. Angular axion current prevents the fixed-charge elimination

used in the homogeneous sector, so the axion and dilaton/saxion fluctuations remain coupled. The radial equations, constraints, and boundary conditions together select the physical solutions.

I organize the small-radius expansion around the BPS radial basis. Successive finite-radius corrections shift the radial power by fixed steps. A logarithm appears when one such correction reaches another indicial root with a nonzero compatibility projection. Appendix C evaluates these projections and matches the local Frobenius expansion to the exact angular solutions.

The first two low harmonics illustrate the distinction. For $\ell = 1$, the BPS system contains a repeated index and hence a logarithmic companion, but the first finite-radius correction to the growing branch closes with an ordinary power. For $\ell = 3$, the compatibility projection is nonzero and produces the first finite-radius resonance,

$$\delta^2 \log(\delta/\delta_0),$$

at fixed outer radius. Its derivative is

$$\frac{\mathrm{d}}{\mathrm{d}\delta}\left[\delta^2 \log(\delta/\delta_0)\right] = 2\delta \log(\delta/\delta_0) + \delta \longrightarrow 0 \qquad (\delta \to 0^+).$$

The resonance therefore enters beyond the linear endpoint response and leaves the slope in Eq. (3.2) unchanged.

Finite-cut Dirichlet data fix the angular boundary problem. After the exact field transformation used in Appendix C, the transverse scalar Sturm–Liouville operators have positive potentials, and the Poincaré bound excludes a zero-frequency Dirichlet mode on the finite interval. The translational collective mode lies along the background scaling direction and has vanishing transverse projection. Spatial rotations act trivially on the radial background. These facts isolate the transverse angular sector from the collective coordinates treated separately in the measure.

The homogeneous soft mode sets the complementary limitation on the quadratic approximation. Its variance grows as the soft eigenvalue decreases, so cubic and quartic boundary vertices eventually compete with the Gaussian action. I compute these vertices after allowing the regular scalar fields and the wormhole radius to relax. Their contractions define the dimensionless control coefficient C_{ctl}. For an outer length scale L, the controlled quadratic regime is

$$\frac{C_{\mathrm{ctl}}}{\mathcal{A}} \ll \delta \ll L^2. \tag{3.4}$$

The lower bound suppresses interaction corrections generated by the soft variance. The upper bound keeps the outer small-radius expansion under control. Appendix C gives the dependence of C_{ctl} on the number of transverse modes and on the product couplings.

At fixed $\mathcal{A}$, the interaction bound is reached before the geometric endpoint $\delta = 0$. A controlled approach to the BPS endpoint therefore uses the correlated semiclassical limit

$$\frac{\delta}{L^2} \longrightarrow 0, \qquad \frac{\mathcal{A}\delta}{C_{\mathrm{ctl}}} \longrightarrow \infty.$$

Within this overlap regime, Eq. (3.2) gives the endpoint slope and its first curvature, while the $\ell = 3$ resonance enters only at the higher order $\delta^2 \log \delta$.

4 Charge dependence and endpoint spectral response

4.1 Charge dependence across sectors

I now determine how the linear finite-radius response varies across the charge lattice. All comparisons use the same right asymptotic dilaton/saxion data, the same boundary state,

and the same source prescription. The leading unnormalized coefficient found in Eq. (3.3) is

$$B_{\boldsymbol{\nu}} = Z_{\boldsymbol{\nu},0} g_{1,\boldsymbol{\nu}},$$

so the charge dependence separates naturally into the BPS sector weight $Z_{\boldsymbol{\nu},0}$ and the geometric response $g_{1,\boldsymbol{\nu}}$.

The product model gives an exact scaling law for the geometric factor. At fixed active support, a uniform rescaling $\boldsymbol{\nu} \mapsto t\boldsymbol{\nu}$ multiplies the fixed-charge potential by t^2 without changing the shape of the stationary target-space trajectory. The normalized transverse fluctuation problem is therefore unchanged, while the overall charge scale enters the radial response through $V_{\boldsymbol{\nu}}$. Since

$$V_{t\boldsymbol{\nu}} = t^2 V_{\boldsymbol{\nu}},$$

the linear coefficient obeys

$$g_{1,t\boldsymbol{\nu}} = t^{-2} g_{1,\boldsymbol{\nu}}.$$

Appendix D derives this relation from the exact product solution. The factor $g_{1,\boldsymbol{\nu}}$ is real and positive. Uniform charge rescaling therefore changes the magnitude of $B_{\boldsymbol{\nu}}$ through the geometric multiplier and introduces no new phase.

Charge reversal gives a second exact relation. The product potential depends on each charge through ν_i^2. Hence

$$\nu_i \mapsto -\nu_i$$

leaves the stationary trajectory, the homogeneous boundary Hessian, and $g_{1,\boldsymbol{\nu}}$ unchanged. Sign-related sectors with the same charge magnitudes therefore carry the same finite-radius geometric response. Any difference between their full coefficients $B_{\boldsymbol{\nu}}$ resides in the corresponding BPS sector factors $Z_{\boldsymbol{\nu},0}$.

Changing the relative charge magnitudes is a different deformation. It changes the stationary transverse point and moves the complete background trajectory in target space even when the right asymptotic data are held fixed. I determine this response by differentiating the background equations, the physical fluctuation operator, and the effective source map with respect to the charge data. The resulting sensitivity equations contain both the explicit charge dependence of the fixed-charge potential and the induced displacement of the saddle. Appendix D formulates these equations using independent symmetric charge bilinears and imposes the physical locus $t_{ij} = \nu_i \nu_j$ after differentiation.

The charge dependence therefore separates into two structures. Uniform rescaling is fixed algebraically by the homogeneity of the product solution and gives the inverse-square law above. Redistribution among charge components changes the target-space trajectory and is determined by the charge-sensitivity problem at fixed outer data. This distinction supplies the sector-by-sector finite-radius input for the spectral analysis below.

4.2 Endpoint spectral response

Having determined the charge dependence of the geometric coefficient, I now fix one charge sector and average its finite-radius response over the BPS endpoint spectrum. Let the reduced physical boundary matrix have the expansion

$$M_{\boldsymbol{\nu}}(\delta) = M_{0,\boldsymbol{\nu}} + \delta D_{1,\boldsymbol{\nu}} + O(\delta^2),$$

where $M_{0,\boldsymbol{\nu}}$ is the positive BPS endpoint matrix and $D_{1,\boldsymbol{\nu}}$ is the first finite-radius deformation obtained from the gravitational boundary problem. Differentiating $M_{\boldsymbol{\nu}} M_{\boldsymbol{\nu}}^{-1} = 1$ gives

$$\frac{\mathrm{d}}{\mathrm{d}\delta} M_{\boldsymbol{\nu}}(\delta)^{-1}\Big|_{\delta=0} = -M_{0,\boldsymbol{\nu}}^{-1} D_{1,\boldsymbol{\nu}} M_{0,\boldsymbol{\nu}}^{-1}.$$

A soft endpoint eigenvalue therefore enters the linear inverse response through two inverse factors. For a physical source vector, the contribution of each endpoint mode is fixed by its eigenvalue together with the matrix elements of $D_{1,\boldsymbol{\nu}}$ and the source overlaps in the same eigenbasis.

The Paper-III ensemble supplies the statistics of $M_{0,\boldsymbol{\nu}}$. The observable requires more than its marginal eigenvalue density: it depends on the joint orientation of the endpoint matrix, the finite-radius deformation, and the effective source vectors. I therefore fix the physical reduction and the deformation before taking the endpoint average. Appendix E formulates the corresponding joint matrix averages and retains the correlations between $M_{0,\boldsymbol{\nu}}$ and $D_{1,\boldsymbol{\nu}}$.

For the explicit endpoint law, I represent the Paper-III square-root operator by a central Gaussian matrix

$$\mathcal{Q} = (X\ Y), \qquad X \in \mathbb{F}^{(N+\kappa)\times m}, \qquad Y \in \mathbb{F}^{(N+\kappa)\times(N-m)}.$$

The m columns of X span the retained boundary block, while the $N-m$ columns of Y are eliminated. Their Schur complement gives

$$M_{0,\boldsymbol{\nu}} = X^\dagger X - X^\dagger Y (Y^\dagger Y)^{-1} Y^\dagger X = X^\dagger P_Y^\perp X, \qquad P_Y^\perp = 1 - Y(Y^\dagger Y)^{-1} Y^\dagger.$$

For the central Gaussian ensemble, X and Y are independent and the law of X is invariant under row rotations. Moreover,

$$\operatorname{rank} P_Y^\perp = (N+\kappa) - (N-m) = m + \kappa. \tag{4.1}$$

A row rotation therefore identifies the reduced matrix with

$$M_{0,\boldsymbol{\nu}} \stackrel{d}{=} Z^\dagger Z, \qquad Z \in \mathbb{F}^{(m+\kappa)\times m},$$

where $\stackrel{d}{=}$ denotes identical probability law and Z is again central Gaussian. The boundary elimination preserves the rectangularity κ and therefore preserves the hard-edge index of the Paper-III ensemble. Appendix D derives this reduced Wishart law and its eigenvalue density.

The determinant weight and the source response probe different functions of this spectrum. The bosonic determinant contains inverse square-root powers of the endpoint eigenvalues, while the source covariance contains inverse powers selected by the source overlaps. Their ensemble averages are therefore controlled by different hard-edge negative moments. Appendix D gives the corresponding integrability conditions.

Two soft mechanisms enter the calculation at different stages. The homogeneous transverse mode of Section 3 develops a deterministic eigenvalue proportional to δ as the finite-radius saddle approaches the BPS endpoint. The Paper-III ensemble instead contains random small positive eigenvalues of $M_{0,\boldsymbol{\nu}}$ already at $\delta = 0$. Exact radial matching determines the first mechanism. The BPS hard-edge measure determines the second. After the physical matrix block, $D_{1,\boldsymbol{\nu}}$, and the source vectors have been fixed, their combination gives the endpoint-averaged finite-radius inverse response.

5 Outlook

This paper establishes the local finite-radius expansion of the two-boundary response about the BPS endpoint. Exact radial matching determines the leading geometric response and its first correction, while the BPS endpoint ensemble determines how the same response is weighted by the hard-edge spectrum. The result places the finite-radius deformation, the fixed-charge coefficient, and the endpoint spectral measure within one calculational sequence.

The immediate extension is to carry this expansion beyond the product target. For a general target-space metric, the stationary trajectory, its transverse Hessian, and the source map evolve together along the radial flow. The charge-sensitivity equations developed here provide the natural starting point for this calculation. Higher radial orders will also generate further resonant channels beyond the first $\ell = 3$ logarithm. Together, these extensions determine how much of the near-BPS structure is universal and how much records the detailed target-space geometry.

A more structural question emerges once the finite-radius coefficient is known over many charge sectors. Each sector then carries two kinds of data. The reduced coefficient $W_{\boldsymbol{\nu}}[b]$ determines how that sector enters the axion-angle representation, while the endpoint measure determines the distribution of physical fluctuation eigenvalues inside the same sector. Paper-II and Paper-III treated these structures separately. The present paper supplies the finite-radius response that places them on the same family of saddles. This makes their joint dependence on charge a well-defined observable.

The resulting problem is naturally expressed in two complementary representations. In the charge representation, one follows the sector dependence of the response and its spectral data directly. In the conjugate axion-angle representation, the same information is reorganized by the Fourier transform over the charge lattice. The relevant observables retain the correlation between the sector-resolved spectral data and their Fourier transform to the axion-angle representation. Such observables probe more than the marginal charge distribution or the marginal endpoint spectrum: they probe how spectral information is organized across charge sectors.

This distinction becomes increasingly sharp for several axions. Charge now ranges over a lattice, the axion angle lies on the dual torus, and the endpoint spectral measure can vary with both the magnitude and direction of the charge vector. Directional large-charge behavior, hard-edge data, and finite-radius response coefficients can therefore be assembled into joint charge–spectral observables. Their transformation to the dual angular variables provides a natural way to test which correlations remain visible after reduction and which require access to the full sector-resolved data.

The endpoint ensemble also provides a microscopic route to this question. In a specified Type-IIB compactification, the ADHM description fixes the hard-edge index, symmetry class, microscopic scale, and charge dictionary. Combining these data with the finite-radius deformation derived here produces a microscopic joint measure for the sector label, endpoint spectrum, and physical response. This construction would connect the macroscopic throat geometry to a sector-resolved microscopic description without collapsing the charge sum and the hard-edge statistics into a single distribution.

The sequence developed in Papers I–III and completed here therefore opens a new level of the problem. The BPS endpoint fixes the physical spectral edge. Finite radius determines how the wormhole probes that edge. The charge reduction determines how each sector contributes to the partition function. The next stage is to determine the joint information carried by these structures and to characterize how that information changes when one passes between the charge, axion-angle, and spectral representations.

Acknowledgment

I thank Jonas Haferkamp, Chinmay Nirkhe and Mark Zhandry for informative clarification on forrelation. I acknowledge that this research was in part undertaken at and financially supported by the Institute for Pure & Applied Mathematics (IPAM, USA), the Simons Institute for the Theory of Computing (SIfTC, USA), and the Fields Institute for Research in Mathematical Sciences (FIRMS, Canada). This work was also supported by the National Research

Foundation of Korea (NRF) (RS-2021-NR060112).

AI Statement

I used ChatGPT 5.6 to draw Figure 1 and to check selected high-precision numerical calculations in Appendix C.5.

A Boundary data and the physical quadratic problem

A.1 Notation, domains, and regulators

I fix the charge sector $\boldsymbol{\nu}$, the saddle branch $\mathfrak{s}$, the integration contour, and the source, boundary-state, measure, and reduction data collected in b. Throughout the appendices,

$$\delta = a_*^2. \tag{A.1}$$

The labels B and F denote bosonic and fermionic sectors, respectively. The integer ℓ labels the S^3 harmonic. In the radial calculation, m labels the harmonic degeneracy; in the later random-matrix calculation, the same letter denotes a matrix dimension. These two uses are independent. The indices i, j label external sources.

I regulate the outer radius, the angular sum, and the radial problem independently. At fixed regulators, all Gaussian integrations and Schur complements are finite dimensional. I perform the algebraic eliminations at this regulated level and take the continuum limits afterward. Removing the radial regulator at fixed ℓ restores the infinite radial spectrum, whereas the matching-surface block for each fixed (ℓ, m) remains finite dimensional.

The quadratic objects below depend on

$$(\boldsymbol{\nu}, \mathfrak{s}, \delta, b, \phi_L, \phi_R). \tag{A.2}$$

I display the charge label $\boldsymbol{\nu}$ and suppress the fixed branch $\mathfrak{s}$, the fixed data b, the asymptotic values selected by the saddle family, and repeated arguments in δ whenever no ambiguity arises. Superscripts Σ and ∂ distinguish quantities defined on the artificial matching surface from quantities defined on the physical outer boundaries.

Symbol	Definition
$Z_{\boldsymbol{\nu}}[J;\delta]$	Full fixed-saddle source functional, including the classical weight, fluctuation measure, and prescribed zero-mode insertions.
$\mathcal{H}_{\boldsymbol{\nu},B}(\delta)$	Constraint-reduced bulk bosonic Hessian on the physical boundary domain.
$\mathcal{N}^{\mathrm{out}}_{\boldsymbol{\nu},L/R,\ell}$	One-sided value-to-momentum map from data at the matching surface to the outward canonical momentum on the left or right radial region.
$\mathcal{K}^{\Sigma}_{\boldsymbol{\nu},B,\ell}$	Quadratic Hessian for the common matching-surface value on Σ in one harmonic sector.
$\mathcal{K}^{\partial}_{\boldsymbol{\nu},B}$	Physical outer-boundary Hessian obtained after the radial interiors and the artificial matching data have been eliminated.

$M_{\boldsymbol{\nu},B}$	Further Schur complement obtained after eliminating complementary bosonic variables from the physical quadratic problem.
$\mathbf{b}_{\boldsymbol{\nu},i},\ \mathbf{b}^{\mathrm{eff}}_{\boldsymbol{\nu},i}$	Bulk source vector and the corresponding effective source vector after complementary bosonic variables have been eliminated.
$\mathbf{s}_{\boldsymbol{\nu},\ell m;i}$	Source vector induced on Σ after the left and right radial interiors have been eliminated.
$\mathcal{A},\ \mathcal{A}_{\boldsymbol{\nu},Q},\ \mathcal{A}_{\boldsymbol{\nu},D}$	Overall reduced-action normalization and the source-independent fluctuation factors generated by the two elimination schemes defined below.

The distinction between the interface and the physical boundary is essential. In the homogeneous transverse example,

$$\mathcal{K}^{\partial}_{\boldsymbol{\nu},B} = \mathcal{A}K, \qquad G = \mathcal{A}^{-1}K^{-1}, \qquad \mathcal{A} > 0. \tag{A.3}$$

The matrix K therefore acts on the physical asymptotic values (q_L, q_R). By contrast, $\mathcal{K}^{\Sigma}_{\boldsymbol{\nu},B,\ell}$ acts on the common field value at the artificial radial cut. Moving the cut changes $\mathcal{K}^{\Sigma}$ while leaving the reconstructed outer-boundary functional unchanged.

Bosonic Gaussian integrals use real fluctuation coordinates and real harmonics. A transpose denotes the real bilinear pairing used in these quadratic forms. A dagger denotes the Hermitian pairing used in the spectral analysis. For analytic continuation, I continue the bilinear action along the chosen integration contour. On a real self-adjoint sector, the contour fixes the phase multiplying $|\det H|^{-1/2}$. On a complex sector, I choose and retain a definite branch of $(\det H)^{-1/2}$ throughout the calculation.

A.2 Boundary conditions and source coefficients

I parameterize the non-BPS saddle family by

$$\delta = a_*^2, \qquad E = 12\delta^2. \tag{A.4}$$

Let ϕ_L^A and ϕ_R^A denote the asymptotic dilaton/saxion values. Along the family I hold $\boldsymbol{\nu}$, ϕ_R^A, the reduction data b, the saddle branch $\mathfrak{s}$, and the integration contour fixed. For every $\delta > 0$, smooth continuation through the minimal three-sphere determines the left asymptotic value $\phi^A_{L,\boldsymbol{\nu},\mathfrak{s}}(\delta)$. The finite-radius derivative therefore follows a definite curve in the space of saddles.

For an on-shell quantity $\mathcal{O}_{\boldsymbol{\nu},\mathfrak{s}}$, I define this derivative by

$$D_\delta \mathcal{O}_{\boldsymbol{\nu},\mathfrak{s}} \equiv \frac{\mathrm{d}}{\mathrm{d}\delta}\mathcal{O}_{\boldsymbol{\nu},\mathfrak{s}}[b, \phi_{L,\boldsymbol{\nu},\mathfrak{s}}(\delta), \phi_R; \delta]\,. \tag{A.5}$$

Thus D_δ includes the induced motion of the left asymptotic data. Source derivatives have a different meaning: they act at fixed δ, fixed asymptotic values, and fixed saddle. The boundary measure belongs to b and is held fixed under both operations. Changing that measure defines a different observable.

For one selected saddle branch, write the reduced scalar sector coefficient as

$$W_{\boldsymbol{\nu},\mathfrak{s}}[b;\delta] = \mathrm{e}^{-S^{\mathrm{cl}}_{\boldsymbol{\nu},\mathfrak{s}}(\delta)}\Pi_{\boldsymbol{\nu},\mathfrak{s}}[b;\delta]. \tag{A.6}$$

The classical exponential and the fluctuation/source prefactor are therefore separated before the charge-sector sum is formed. Assume that the classical action has a finite right derivative at the BPS endpoint. Its near-endpoint expansion is

$$S^{\rm cl}_{\boldsymbol{\nu},\mathfrak{s}}(\delta) = S^{\rm BPS}_{\boldsymbol{\nu},\mathfrak{s}} + \widehat{s}_{1,\boldsymbol{\nu},\mathfrak{s}}\,\delta + o(\delta), \tag{A.7}$$

with

$$\widehat{s}_{1,\boldsymbol{\nu},\mathfrak{s}} = D_\delta S^{\rm cl}_{\boldsymbol{\nu},\mathfrak{s}}\big|_{0^+}\,. \tag{A.8}$$

Because $\sqrt{E} = \sqrt{12}\,\delta$, the same expansion may be written as

$$s_{1,\boldsymbol{\nu},\mathfrak{s}} = \frac{\widehat{s}_{1,\boldsymbol{\nu},\mathfrak{s}}}{\sqrt{12}}, \qquad S^{\rm cl}_{\boldsymbol{\nu},\mathfrak{s}}(\delta) = S^{\rm BPS}_{\boldsymbol{\nu},\mathfrak{s}} + s_{1,\boldsymbol{\nu},\mathfrak{s}}\sqrt{E} + o(\sqrt{E}). \tag{A.9}$$

The coefficient in Eq. (A.8) includes the boundary work generated by the motion of $\phi^A_L(\delta)$. I now fix $\mathfrak{s}$ and suppress the branch label.

The source functional distinguishes the unnormalized coefficient from the connected response. I define

$$C^{ij}_{\boldsymbol{\nu}}(\delta) = \partial_{J_i}\partial_{J_j} Z_{\boldsymbol{\nu}}[J;\delta]\big|_{J=0}\,, \tag{A.10}$$

and

$$G^{ij}_{\boldsymbol{\nu}}(\delta) = \partial_{J_i}\partial_{J_j} \log Z_{\boldsymbol{\nu}}[J;\delta]\big|_{J=0}\,. \tag{A.11}$$

The corresponding one-source expectation is

$$g^i_{\boldsymbol{\nu}}(\delta) = \partial_{J_i} \log Z_{\boldsymbol{\nu}}[J;\delta]|_{J=0}\,. \tag{A.12}$$

Direct differentiation gives

$$C^{ij}_{\boldsymbol{\nu}}(\delta) = Z_{\boldsymbol{\nu}}[0;\delta]\left[G^{ij}_{\boldsymbol{\nu}}(\delta) + g^i_{\boldsymbol{\nu}}(\delta) g^j_{\boldsymbol{\nu}}(\delta)\right]. \tag{A.13}$$

For the centered insertions used in the quadratic calculation, $g^i_{\boldsymbol{\nu}} = 0$, and hence

$$C^{ij}_{\boldsymbol{\nu}}(\delta) = Z_{\boldsymbol{\nu}}[0;\delta]\, G^{ij}_{\boldsymbol{\nu}}(\delta). \tag{A.14}$$

The connected response removes all source-independent factors. The unnormalized coefficient retains the classical weight, determinants or Pfaffians, exact-mode measures, collective-coordinate factors, and boundary normalization. Interactions can generate a nonzero one-source expectation and then restore the second term in Eq. (A.13).

To isolate the fluctuation and source prefactor, define

$$\widehat{Z}_{\boldsymbol{\nu}}[J;\delta] = \mathrm{e}^{S^{\rm cl}_{\boldsymbol{\nu}}(\delta)} Z_{\boldsymbol{\nu}}[J;\delta]. \tag{A.15}$$

Its unnormalized two-source coefficient is

$$\widehat{C}^{ij}_{\boldsymbol{\nu}}(\delta) = \partial_{J_i}\partial_{J_j}\widehat{Z}_{\boldsymbol{\nu}}[J;\delta]\Big|_{J=0} = \mathrm{e}^{S^{\rm cl}_{\boldsymbol{\nu}}(\delta)} C^{ij}_{\boldsymbol{\nu}}(\delta). \tag{A.16}$$

For the linear reduction considered here,

$$\Pi_{\boldsymbol{\nu}}[b;\delta] = R_b\Big[\widehat{C}^{ij}_{\boldsymbol{\nu}}(\delta)\Big]\,. \tag{A.17}$$

Equations (A.6) and (A.17) reproduce the Paper-II order of operations: the fixed-saddle source functional first supplies an unnormalized two-end coefficient, the reduction R_b converts that coefficient into the scalar prefactor $\Pi_{\boldsymbol{\nu}}$, and the classical exponential restores the full sector coefficient $W_{\boldsymbol{\nu}}[b;\delta]$. The reduction acts on $\widehat{C}^{ij}_{\boldsymbol{\nu}}$ itself, rather than on a derivative of $\log \widehat{Z}_{\boldsymbol{\nu}}$.

The endpoint relation used in the main text now follows directly. For a centered source component, take

$$G^{ij}_{\boldsymbol{\nu}}(0) = 0, \qquad G^{ij}_{\boldsymbol{\nu}}(\delta) = g^{ij}_{1,\boldsymbol{\nu}}\delta + o(\delta), \qquad Z_{\boldsymbol{\nu}}[0;\delta] \longrightarrow Z_{\boldsymbol{\nu},0}. \tag{A.18}$$

Equation (A.14) then gives

$$C^{ij}_{\boldsymbol{\nu}}(\delta) = Z_{\boldsymbol{\nu},0} g^{ij}_{1,\boldsymbol{\nu}}\delta + o(\delta), \qquad \left.\frac{\mathrm{d}C^{ij}_{\boldsymbol{\nu}}}{\mathrm{d}\delta}\right|_{0^+} = Z_{\boldsymbol{\nu},0} g^{ij}_{1,\boldsymbol{\nu}}. \tag{A.19}$$

Thus the endpoint slope factorizes into the normalized geometric response and the complete BPS sector weight. The existence of the finite limit $Z_{\boldsymbol{\nu},0}$ is a statement about the full fixed-saddle measure, including exact modes, prescribed insertions, and all remaining fluctuation factors. The normalized response alone does not determine this weight.

A.3 Constraint reduction and Gaussian integration

The fluctuation domain is fixed by the constraints, gauge choice, integration contour, outer boundary state, and regulator. After constraint reduction, the centered fixed-saddle source functional takes the form

$$\begin{aligned} Z_{\boldsymbol{\nu}}[J;\delta] = \mathrm{e}^{-S^{\mathrm{cl}}_{\boldsymbol{\nu}}(\delta)} \mathcal{J}^{\mathrm{exact}}_{\boldsymbol{\nu}}(\delta) \int_{\Gamma_{\boldsymbol{\nu},\delta}} \mathrm{d}\eta\, \mathrm{d}\Psi\, \mathrm{d}\bar{c}_{\mathrm{gh}}\, \mathrm{d}c_{\mathrm{gh}} \\ \times \exp\!\left[-\frac{1}{2}\eta^T \mathcal{H}_{\boldsymbol{\nu},B}\eta - \frac{1}{2}\Psi^T \mathcal{D}_{\boldsymbol{\nu},F}\Psi - \bar{c}^T_{\mathrm{gh}} \mathcal{M}_{\boldsymbol{\nu},\mathrm{gh}} c_{\mathrm{gh}} + J_i \mathbf{b}^T_{\boldsymbol{\nu},i}\eta + \frac{1}{2} J_i \mathcal{V}^{ij}_{\boldsymbol{\nu}} J_j - S_{\mathrm{int}}\right]. \end{aligned} \tag{A.20}$$

All quadratic operators and source vectors in Eq. (A.20) depend on δ. The vectors $\mathbf{b}_{\boldsymbol{\nu},i}$ describe linear source insertions, while $\mathcal{V}^{ij}_{\boldsymbol{\nu}}$ contains direct quadratic source terms. The antisymmetric Grassmann form defines $\mathcal{D}_{\boldsymbol{\nu},F}$; an equivalent complex Dirac representation gives the corresponding determinant. First-order fermions carry their own boundary domain.

The factor $\mathcal{J}^{\mathrm{exact}}_{\boldsymbol{\nu}}$ contains the collective-coordinate measure and the prescribed insertions that saturate exact fermion zero modes. I take it to be source independent in the formulas below. A source-dependent saturation insertion must instead be included before the source derivatives are taken. An unsaturated fermion zero mode makes the corresponding saddle coefficient vanish.

I now state explicitly how the physical bosonic Hessian entering Eq. (A.20) is obtained. After eliminating the first-class constraints and linear multipliers, let u_{aux} denote the remaining quadratic auxiliary variables. For one angular sector, write

$$I^{(2)}_{\ell} = \frac{1}{2}\begin{pmatrix}\eta \\ u_{\mathrm{aux}}\end{pmatrix}^T \begin{pmatrix} H^{(\ell)}_{dd} & H^{(\ell)}_{da} \\ H^{(\ell)}_{ad} & H^{(\ell)}_{aa}\end{pmatrix}\begin{pmatrix}\eta \\ u_{\mathrm{aux}}\end{pmatrix} + I^{(2)}_{\ell,\partial}. \tag{A.21}$$

When $H^{(\ell)}_{aa}$ is invertible, stationarity in u_{aux} gives

$$u_{\mathrm{aux}} = -\big(H^{(\ell)}_{aa}\big)^{-1} H^{(\ell)}_{ad}\eta,$$

and hence

$$\mathcal{H}^{\mathrm{phys}}_{\boldsymbol{\nu},B,\ell} = H^{(\ell)}_{dd} - H^{(\ell)}_{da}\big(H^{(\ell)}_{aa}\big)^{-1} H^{(\ell)}_{ad}. \tag{A.22}$$

Thus the physical quadratic operator is formed only after the Hamiltonian and momentum constraints have been imposed. The boundary quadratic form remains part of its domain.

At the BPS endpoint, this physical domain reduces to the endpoint domain of Paper-I, and

$$\mathcal{H}_{\boldsymbol{\nu},B}(0) = \mathcal{Q}_{\boldsymbol{\nu}}^{\dagger}\mathcal{Q}_{\boldsymbol{\nu}}. \tag{A.23}$$

Equation (A.23) fixes the BPS endpoint operator. The finite-radius Hessian is obtained by deforming the complete constraint-reduced boundary-value problem. The endpoint square also fixes no probability law for individual matrix entries; the Paper-III ensemble is an additional microscopic input.

I next separate the finite bosonic block that carries the response from its Gaussian complement. Exact collective modes have already been extracted. Choose a set of retained bosonic coordinates that is fixed for all δ, and let P_B project onto this subspace. Set $Q_B = 1 - P_B$ and define

$$\mathcal{H}_{\boldsymbol{\nu},B,Q}(\delta) = Q_B\mathcal{H}_{\boldsymbol{\nu},B}(\delta)Q_B. \tag{A.24}$$

On a patch where $\mathcal{H}_{\boldsymbol{\nu},B,Q}$ is invertible, eliminating the Q_B variables gives

$$M_{\boldsymbol{\nu},B}(\delta) = P_B\mathcal{H}_{\boldsymbol{\nu},B}P_B - P_B\mathcal{H}_{\boldsymbol{\nu},B}Q_B\mathcal{H}_{\boldsymbol{\nu},B,Q}^{-1}Q_B\mathcal{H}_{\boldsymbol{\nu},B}P_B. \tag{A.25}$$

All blocks and source vectors are expressed in the same retained coordinates as δ varies. A change of basis within the retained subspace acts on $M_{\boldsymbol{\nu},B}$ by congruence and contributes the corresponding measure Jacobian.

The endpoint scaling of a soft block follows directly from this Schur complement. Let P_Z project onto an exact kernel of the endpoint operator that remains in the retained problem, and set $Q_Z = 1 - P_Z$. Self-adjointness gives

$$Q_Z\mathcal{H}_{B,0}P_Z = 0.$$

For

$$\mathcal{H}_B(\delta) = \mathcal{H}_{B,0} + \delta\mathcal{H}_{B,1} + O(\delta^2)$$

and a bounded inverse on the complementary subspace,

$$M_Z(\delta) = \delta\, P_Z\mathcal{H}_{B,1}P_Z + O(\delta^2). \tag{A.26}$$

The mixed blocks begin at $O(\delta)$, so their Schur contribution starts at $O(\delta^2)$. For differentiable input the remainder may be written as $o(\delta)$. A contribution proportional to $\delta^2\log(\delta/\delta_0)$ carries the same logarithm through the finite-dimensional elimination. At fixed regulator, the complementary endpoint spectrum has a finite gap. The continuum limit requires uniform control of the complementary resolvent.

The fermionic reduction proceeds in parallel. For a finite antisymmetric fermion matrix, choose a compatible even-dimensional decomposition $P_F + Q_F = 1$ and a fixed Berezin orientation. Eliminating the Q_F variables gives

$$M_{\boldsymbol{\nu},F} = P_F\mathcal{D}_{\boldsymbol{\nu},F}P_F - P_F\mathcal{D}_{\boldsymbol{\nu},F}Q_F\big(Q_F\mathcal{D}_{\boldsymbol{\nu},F}Q_F\big)^{-1}Q_F\mathcal{D}_{\boldsymbol{\nu},F}P_F. \tag{A.27}$$

In a real Grassmann basis, $M_{\boldsymbol{\nu},F}$ remains antisymmetric. Appendix F gives the corresponding determinant, inverse, and Pfaffian identities. On compatible reduced spaces,

$$\det{}'\mathcal{H}_{\boldsymbol{\nu},B} = \det\mathcal{H}_{\boldsymbol{\nu},B,Q}\,\det M_{\boldsymbol{\nu},B}, \tag{A.28}$$

$$\mathrm{Pf}'\mathcal{D}_{\boldsymbol{\nu},F} = \mathrm{Pf}\big(Q_F\mathcal{D}_{\boldsymbol{\nu},F}Q_F\big)\,\mathrm{Pf}M_{\boldsymbol{\nu},F}. \tag{A.29}$$

The primes refer only to exact modes already extracted together with their measures. Kernel removal in a continuum gluing formula must be performed compatibly across the factors.

Gaussian elimination also transforms the sources. Define

$$\mathbf{b}_{\boldsymbol{\nu},i,P} = P_B \mathbf{b}_{\boldsymbol{\nu},i}, \qquad \mathbf{b}_{\boldsymbol{\nu},i,Q} = Q_B \mathbf{b}_{\boldsymbol{\nu},i}. \tag{A.30}$$

The complementary response and the effective retained source are

$$G^{ij}_{\boldsymbol{\nu},Q} = \mathbf{b}^{\dagger}_{\boldsymbol{\nu},i,Q} \mathcal{H}^{-1}_{\boldsymbol{\nu},B,Q} \mathbf{b}_{\boldsymbol{\nu},j,Q}, \tag{A.31}$$

$$\mathbf{b}^{\mathrm{eff}}_{\boldsymbol{\nu},i} = \mathbf{b}_{\boldsymbol{\nu},i,P} - P_B \mathcal{H}_{\boldsymbol{\nu},B} Q_B \mathcal{H}^{-1}_{\boldsymbol{\nu},B,Q} \mathbf{b}_{\boldsymbol{\nu},i,Q}. \tag{A.32}$$

Completing the square produces both quantities in the same elimination step. The block inverse then gives the exact decomposition

$$\mathbf{b}^{\dagger}_{\boldsymbol{\nu},i} \mathcal{H}^{-1}_{\boldsymbol{\nu},B} \mathbf{b}_{\boldsymbol{\nu},j} = G^{ij}_{\boldsymbol{\nu},Q} + \left(\mathbf{b}^{\mathrm{eff}}_{\boldsymbol{\nu},i}\right)^{\dagger} M^{-1}_{\boldsymbol{\nu},B} \mathbf{b}^{\mathrm{eff}}_{\boldsymbol{\nu},j}. \tag{A.33}$$

The complementary determinant, the complementary source response, and the effective source vector are therefore parts of one Gaussian reduction and enter the coefficient together.

Collect all remaining source-independent factors into $\mathcal{Z}_{\boldsymbol{\nu},\mathrm{rem}}$. These include the ghost sector, self-dual sectors, exact-mode measure, prescribed saturation insertions, and any additional factors outside the displayed bosonic and fermionic blocks. At finite regulator define

$$\mathcal{A}_{\boldsymbol{\nu},Q} = \mathcal{Z}_{\boldsymbol{\nu},\mathrm{rem}} \frac{\mathrm{Pf}\big(Q_F \mathcal{D}_{\boldsymbol{\nu},F} Q_F\big)}{\sqrt{|\det \mathcal{H}_{\boldsymbol{\nu},B,Q}|}}. \tag{A.34}$$

On a real self-adjoint patch, the contour phase is included in $\mathcal{Z}_{\boldsymbol{\nu},\mathrm{rem}}$. For a complex saddle, the same expression is understood with the determinant branch fixed by the chosen contour.

The connected quadratic source response is

$$\mathcal{R}^{ij}_{\boldsymbol{\nu}} = \mathcal{V}^{ij}_{\boldsymbol{\nu}} + G^{ij}_{\boldsymbol{\nu},Q} + \left(\mathbf{b}^{\mathrm{eff}}_{\boldsymbol{\nu},i}\right)^{\dagger} M^{-1}_{\boldsymbol{\nu},B} \mathbf{b}^{\mathrm{eff}}_{\boldsymbol{\nu},j}. \tag{A.35}$$

The three terms have distinct origins: a direct quadratic source term, a response generated inside the eliminated complement, and propagation through the retained physical block.

After removing the classical exponential as in Eq. (A.15), the complete quadratic source functional becomes

$$\widehat{Z}^{(2)}_{\boldsymbol{\nu}}[J;\delta] = \mathcal{A}_{\boldsymbol{\nu},Q} \frac{\mathrm{Pf} M_{\boldsymbol{\nu},F}}{\sqrt{|\det M_{\boldsymbol{\nu},B}|}} \exp\left(\frac{1}{2} J_i \mathcal{R}^{ij}_{\boldsymbol{\nu}} J_j\right). \tag{A.36}$$

Two source derivatives give the corresponding unnormalized coefficient,

$$\widehat{C}^{ij}_{\boldsymbol{\nu}} = \mathcal{A}_{\boldsymbol{\nu},Q} \frac{\mathrm{Pf} M_{\boldsymbol{\nu},F}}{\sqrt{|\det M_{\boldsymbol{\nu},B}|}} \mathcal{R}^{ij}_{\boldsymbol{\nu}} + \widehat{C}^{ij}_{\boldsymbol{\nu},\mathrm{higher}}. \tag{A.37}$$

Thus $\mathcal{R}^{ij}_{\boldsymbol{\nu}}$ is the connected Gaussian response, while the prefactor supplies its source-independent quadratic weight. The term $\widehat{C}^{ij}_{\boldsymbol{\nu},\mathrm{higher}}$ contains interaction corrections and source-dependent contributions beyond the quadratic functional.

For a fixed saddle, the finite-radius coefficient is therefore specified by the data

$$\left(M_{\boldsymbol{\nu},B}, M_{\boldsymbol{\nu},F}, \mathbf{b}^{\mathrm{eff}}_{\boldsymbol{\nu},i}, G^{ij}_{\boldsymbol{\nu},Q}, \mathcal{A}_{\boldsymbol{\nu},Q}, \mathcal{V}^{ij}_{\boldsymbol{\nu}}, R_b\right). \tag{A.38}$$

The classical saddle fixes the exponential weight. Constraint reduction and radial matching fix the physical quadratic matrices and source response. The complete field measure fixes the normalization. The reduction R_b then converts the resulting unnormalized source coefficient into the scalar fixed-charge coefficient used in the main text.

B Finite-radius expansion and boundary Hessians

B.1 Local coefficients, matching, and finite elimination

Fix the saddle branch, integration contour, and boundary family defined in Appendix A. I express the fluctuations, source vectors, and boundary data in one common coordinate system for all δ. At fixed outer radius, the local quadratic data admit the expansions

$$\mathcal{H}^{\mathrm{loc}}_{\boldsymbol{\nu},B}(\delta) = \mathcal{H}^{(0)}_{\boldsymbol{\nu},B} + \delta\mathcal{H}^{(1)}_{\boldsymbol{\nu},B} + \delta^2\mathcal{H}^{(2)}_{\boldsymbol{\nu},B} + \cdots , \tag{B.1}$$

$$\mathcal{D}^{\mathrm{loc}}_{\boldsymbol{\nu},F}(\delta) = \mathcal{D}^{(0)}_{\boldsymbol{\nu},F} + \delta\mathcal{D}^{(1)}_{\boldsymbol{\nu},F} + \delta^2\mathcal{D}^{(2)}_{\boldsymbol{\nu},F} + \cdots , \tag{B.2}$$

$$\mathbf{b}^{\mathrm{loc}}_{\boldsymbol{\nu},i}(\delta) = \mathbf{b}^{(0)}_{\boldsymbol{\nu},i} + \delta\mathbf{b}^{(1)}_{\boldsymbol{\nu},i} + \delta^2\mathbf{b}^{(2)}_{\boldsymbol{\nu},i} + \cdots . \tag{B.3}$$

Individual coefficients may vanish in a specified background. These outer expansions cease to be uniform near the shrinking minimal three-sphere. The physical boundary matrices are therefore obtained by matching the outer expansion to the corresponding inner problem. The radial analysis of Appendix C.1 supplies both the ordinary power corrections and the resonant logarithms.

The finite-dimensional Gaussian eliminations preserve this asymptotic structure.

Finite elimination and logarithmic expansions. Let

$$\mathsf{M}(\delta) = \begin{pmatrix} \mathsf{A}(\delta) & \mathsf{B}(\delta) \\ \mathsf{C}(\delta) & \mathsf{D}(\delta) \end{pmatrix} \tag{B.4}$$

be a finite matrix whose blocks admit asymptotic expansions in integer powers of δ and $\log(\delta/\delta_0)$ with finite limits as $\delta \to 0^+$. Suppose

$$\mathsf{D}(\delta) = \mathsf{D}_0 + o(1), \qquad \det \mathsf{D}_0 \neq 0. \tag{B.5}$$

Then the Schur complement

$$\mathsf{A} - \mathsf{B}\mathsf{D}^{-1}\mathsf{C} \tag{B.6}$$

admits an asymptotic expansion in the same class. If all four blocks are analytic in δ, the Schur complement is analytic in δ.

To see this, write

$$\mathsf{D} = \mathsf{D}_0 + \mathsf{E}, \qquad \mathsf{E} = o(1). \tag{B.7}$$

For sufficiently small δ, $\|\mathsf{D}_0^{-1}\mathsf{E}\| < 1$, and hence

$$\mathsf{D}^{-1} = \sum_{n\geq 0} \bigl(-\mathsf{D}_0^{-1}\mathsf{E}\bigr)^n \mathsf{D}_0^{-1}. \tag{B.8}$$

Expanding this series to any fixed asymptotic order and substituting it into $\mathsf{A} - \mathsf{B}\mathsf{D}^{-1}\mathsf{C}$ preserves the powers of δ and the logarithms carried by the input blocks. The finite-limit hypothesis excludes an unsuppressed $\delta^0 \log^m \delta$ divergence in the inverted block. For analytic input, matrix inversion is analytic in a neighborhood of the invertible matrix D_0, and the Schur complement is analytic there.

This finite-dimensional argument applies directly at fixed regulator. Its continuum counterpart additionally requires a fixed operator domain and uniform control of the inverse on the eliminated subspace.

For an analytic reduced bosonic block, I write

$$M_{\boldsymbol{\nu},B}(\delta) = M_{0,\boldsymbol{\nu}} + \delta D_{1,\boldsymbol{\nu}} + \delta^2 D_{2,\boldsymbol{\nu}} + \cdots , \tag{B.9}$$

$$\mathbf{b}^{\mathrm{eff}}_{\boldsymbol{\nu},i}(\delta) = \mathbf{b}^{\mathrm{eff}}_{0,\boldsymbol{\nu},i} + \delta \mathbf{b}^{\mathrm{eff}}_{1,\boldsymbol{\nu},i} + \cdots , \tag{B.10}$$

$$\mathcal{V}^{ij}_{\boldsymbol{\nu}}(\delta) = \mathcal{V}^{ij}_{0,\boldsymbol{\nu}} + \delta \mathcal{V}^{ij}_{1,\boldsymbol{\nu}} + \cdots , \tag{B.11}$$

$$G^{ij}_{\boldsymbol{\nu},Q}(\delta) = G^{ij}_{0,\boldsymbol{\nu},Q} + \delta G^{ij}_{1,\boldsymbol{\nu},Q} + \cdots . \tag{B.12}$$

The matrix $D_{1,\boldsymbol{\nu}}$ is the first finite-radius deformation that enters the endpoint inverse response in the main text. The angular problem also generates nonanalytic terms. The first resonant contribution found below occurs in the $\ell = 3$ sector and has strength

$$\eta_{3,\log}(\delta) = \delta^2 \log(\delta/\delta_0), \qquad \delta_0 > 0. \tag{B.13}$$

Its first derivative vanishes at $\delta = 0^+$. Its contribution to an observable is fixed only after the corresponding boundary map and source vectors have been applied.

Separate the matrix structure from its scalar strength:

$$M(\delta) = M_0 + \eta(\delta) D + o(\eta), \qquad \eta(\delta) \longrightarrow 0. \tag{B.14}$$

Let M_0 be Hermitian positive definite and let

$$g = \lambda_{\min}(M_0) > 0.$$

Weyl's bound gives

$$\|M(\delta) - M_0\|_{\mathrm{op}} < g \quad \Longrightarrow \quad M(\delta) > 0. \tag{B.15}$$

For the affine deformation $M_0 + \eta D$ with $\eta \geq 0$, the first zero generated by a negative direction of D occurs at

$$\eta_c = \inf_{\substack{v \neq 0 \\ v^\dagger D v < 0}} \frac{v^\dagger M_0 v}{-v^\dagger D v}. \tag{B.16}$$

Each admissible Rayleigh quotient is the value of η at which the quadratic form first vanishes along that direction; their infimum gives the first crossing. Higher-order terms in $M(\delta)$ shift this affine estimate. For the resonant term it is convenient, on $0 < \delta < \delta_0$, to use the positive strength

$$\widetilde{\eta}_{3,\log}(\delta) = \delta^2 \log(\delta_0/\delta)$$

and absorb the overall minus sign into D.

The source-independent nonzero-mode factor varies with the same quadratic data. At finite regulator,

$$\begin{aligned} \partial_\delta \log \mathcal{T}^{\mathrm{nz}}_{\boldsymbol{\nu}} = {} & \frac{1}{2}\mathrm{Tr}\big[(\mathcal{D}_{F,\mathrm{nz}})^{-1}\partial_\delta \mathcal{D}_{F,\mathrm{nz}}\big] + \mathrm{Tr}\big[(\mathcal{M}_{\mathrm{gh,nz}})^{-1}\partial_\delta \mathcal{M}_{\mathrm{gh,nz}}\big] \\ & - \frac{1}{2}\mathrm{Tr}\big[(\mathcal{H}_{B,\mathrm{nz}})^{-1}\partial_\delta \mathcal{H}_{B,\mathrm{nz}}\big] + \partial_\delta \log \mathcal{T}^{\mathrm{extra}}_{\boldsymbol{\nu}}. \end{aligned} \tag{B.17}$$

The factor $\mathcal{T}^{\mathrm{nz}}_{\boldsymbol{\nu}}$ includes the associated measure factors and contour phases. In the continuum, its determinant traces are defined with the same renormalization prescription used for the corresponding functional determinants.

For the finite reduced matrices,

$$\partial_\delta \log \frac{\mathrm{Pf} M_F}{\sqrt{\det M_B}} = \frac{1}{2}\mathrm{Tr}\big(M_F^{-1}\partial_\delta M_F\big) - \frac{1}{2}\mathrm{Tr}\big(M_B^{-1}\partial_\delta M_B\big)\,, \tag{B.18}$$

$$\partial_\delta M_B^{-1} = -M_B^{-1}(\partial_\delta M_B) M_B^{-1}. \tag{B.19}$$

These identities hold on an invertible patch with the Pfaffian and determinant branches fixed by the chosen contour. A zero crossing marks the boundary of that patch and requires the corresponding zero direction to be extracted and treated separately.

Equations (B.1)–(B.19) propagate the local finite-radius expansion through Gaussian elimination, determinants, and inverse responses. The radial boundary-value problem determines the matrices and source vectors entering these identities.

B.2 One radial region and its value-to-momentum map

I now construct the one-sided value-to-momentum maps and glue the two radial regions to obtain the physical outer-boundary Hessian.

Consider one scalar harmonic sector. I use real harmonics $Y_{\ell m}$ on the unit S^3, normalized with respect to $\mathrm{d}\Omega_3/\mathcal{V}_3$, with

$$-\nabla^2 Y_{\ell m} = \ell(\ell+2) Y_{\ell m}. \tag{B.20}$$

Fix (ℓ, m), $\boldsymbol{\nu}$, and δ. After the angular decomposition, the coupled components in this sector form a radial vector $y(\tau)$. The same construction applies block by block to the remaining spin sectors with their corresponding harmonics and multiplicities.

After constraint reduction, the quadratic action on one radial region is

$$\begin{aligned} I^{(2)}_{\boldsymbol{\nu},B,\ell m}[y] = \frac{1}{2}\int \mathrm{d}\tau \, \Big[\dot{y}^\dagger A_\ell \dot{y} + \dot{y}^\dagger B_\ell y + y^\dagger B_\ell^\dagger \dot{y} + y^\dagger C_\ell y \Big] \\ + \frac{1}{2} y_\Sigma^\dagger B_{\Sigma,\ell} y_\Sigma. \end{aligned} \tag{B.21}$$

The matrices A_ℓ, B_ℓ, and C_ℓ depend on $(\tau, \boldsymbol{\nu}, \delta)$. They are local radial coefficients and are unrelated to the block matrices used in the Schur-complement algebra of the preceding subsection. On a real self-adjoint sector, $A_\ell = A_\ell^\dagger$, $C_\ell = C_\ell^\dagger$, and A_ℓ is invertible.

The canonical radial momentum is

$$p = A_\ell \dot{y} + B_\ell y. \tag{B.22}$$

The Euler–Lagrange equation gives

$$\dot{p} = B_\ell^\dagger \dot{y} + C_\ell y.$$

Eliminating $\dot{y}$ converts the second-order radial equation into the first-order Hamiltonian system

$$\frac{\mathrm{d}}{\mathrm{d}\tau}\begin{pmatrix} y \\ p \end{pmatrix} = \begin{pmatrix} -A_\ell^{-1} B_\ell & A_\ell^{-1} \\ C_\ell - B_\ell^\dagger A_\ell^{-1} B_\ell & B_\ell^\dagger A_\ell^{-1} \end{pmatrix} \begin{pmatrix} y \\ p \end{pmatrix}. \tag{B.23}$$

Introducing a spectral parameter z replaces C_ℓ by $C_\ell - z W_\ell$, where $W_\ell > 0$ is the radial eigenvalue weight. The Gaussian response studied in this paper is evaluated at $z = 0$.

For either radial region $\alpha = L, R$, let the columns of $Y_{\alpha,\ell}(\tau, z)$ solve the homogeneous equation and satisfy the prescribed physical outer-boundary condition. Define the corresponding momentum matrix by

$$\Pi_{\alpha,\ell} = A_\ell \dot{Y}_{\alpha,\ell} + B_\ell Y_{\alpha,\ell}. \tag{B.24}$$

On every interval where $Y_{\alpha,\ell}$ is invertible, the value-to-momentum map is

$$\mathcal{N}_{\boldsymbol{\nu},\alpha,\ell}(\tau, z; \delta) = \Pi_{\alpha,\ell}(\tau, z) Y_{\alpha,\ell}(\tau, z)^{-1}. \tag{B.25}$$

Differentiating Eq. (B.25) and using Eq. (B.23) gives the matrix Riccati equation

$$\dot{\mathcal{N}} = C_\ell - z W_\ell - \big(B_\ell^\dagger - \mathcal{N}\big) A_\ell^{-1} \big(B_\ell - \mathcal{N}\big). \tag{B.26}$$

For real z and a self-adjoint boundary domain, $\mathcal{N}$ is Hermitian. For complex z, Eq. (B.26) defines its analytic continuation with the displayed operator ordering. In that continuation, $B_\ell^\dagger - \mathcal{N}$ is generally distinct from $(B_\ell - \mathcal{N})^\dagger$. A zero of $\det Y_{\alpha,\ell}$ produces a pole of this Riccati chart. The underlying first-order system remains regular and continues through the pole in another boundary coordinate.

The two radial regions carry opposite outward orientations at the artificial matching surface Σ. I therefore convert the canonical momentum on each side to the outward momentum before gluing and denote the resulting maps by $\mathcal{N}^{\mathrm{out}}_{\boldsymbol{\nu},L,\ell}$ and $\mathcal{N}^{\mathrm{out}}_{\boldsymbol{\nu},R,\ell}$. For the common matching value $y_{\Sigma,\ell m}$, the two one-sided on-shell actions add. Including the explicit quadratic term localized at Σ gives the interface Hessian

$$\mathcal{K}^{\Sigma}_{\boldsymbol{\nu},B,\ell}(z;\delta) = \mathcal{N}^{\mathrm{out}}_{\boldsymbol{\nu},L,\ell}(z;\delta) + \mathcal{N}^{\mathrm{out}}_{\boldsymbol{\nu},R,\ell}(z;\delta) + \mathcal{B}_{\boldsymbol{\nu},\Sigma,\ell}(z;\delta). \tag{B.27}$$

Variation with respect to the common matching value is therefore the linearized gluing condition. When both one-sided Dirichlet problems are invertible, a nontrivial zero mode of the glued system exists precisely when

$$\det \mathcal{K}^{\Sigma}_{\boldsymbol{\nu},B,\ell}(0;\delta) = 0. \tag{B.28}$$

A kernel of either one-sided Dirichlet problem must first be extracted with its own measure; after that extraction, Eq. (B.28) applies to the remaining invertible blocks.

The same map follows directly from the one-sided on-shell action. Holding the physical outer data fixed,

$$\partial_{y_\Sigma} I^{\mathrm{on}}_L(y_\Sigma) = p^{\mathrm{out}}_{L,\Sigma}, \tag{B.29}$$

$$\partial^2_{y_\Sigma} I^{\mathrm{on}}_L(y_\Sigma) = \mathcal{N}^{\mathrm{out}}_{\boldsymbol{\nu},L,\ell}(0;\delta) \tag{B.30}$$

at quadratic order. The right region obeys the analogous relations.

A further simplification follows only when the complete left and right boundary-value problems are related by reflection. This requires the background fields, fluctuation operator, boundary conditions, and boundary terms to transform into one another. Then the two outward maps coincide and

$$\mathcal{K}^{\Sigma}_{\boldsymbol{\nu},B,\ell}(0;\delta) = 2\,\partial^2_{y_\Sigma} I^{\mathrm{on}}_{\mathrm{half}} + \mathcal{B}_{\boldsymbol{\nu},\Sigma,\ell}(0;\delta). \tag{B.31}$$

Reflection symmetry of the metric alone does not imply this relation. A generic charged scalar trajectory requires the two independent one-sided maps in Eq. (B.27).

The matrix $\mathcal{K}^{\Sigma}_{\boldsymbol{\nu},B,\ell}$ is the complete finite-dimensional quadratic form for the matching value in this harmonic sector. The next subsection integrates this matching value and combines its determinant and inverse response with the two Dirichlet interiors.

B.3 Gaussian gluing for one harmonic

I now perform the gluing at fixed radial discretization and angular cutoff. For each side $\alpha = L, R$, decompose the radial field as

$$y_\alpha = y^{\mathrm{cl}}_\alpha[y_\Sigma] + \xi_\alpha, \qquad \xi_\alpha|_\Sigma = 0,$$

where $y^{\mathrm{cl}}_\alpha[y_\Sigma]$ solves the homogeneous radial equation with matching value y_Σ and the prescribed physical outer-boundary condition. The fluctuations ξ_α therefore carry the Dirichlet Hessians $\mathcal{H}_{\boldsymbol{\nu},L,D,\ell}$ and $\mathcal{H}_{\boldsymbol{\nu},R,D,\ell}$. Here D denotes vanishing fluctuation at the artificial matching surface Σ, with the physical outer-boundary condition unchanged.

Integrating the two Dirichlet interiors produces three objects. The direct quadratic source term is $\mathcal{V}^{ij}_{\boldsymbol{\nu},\ell m}$. Propagation entirely inside the Dirichlet interiors gives $G^{ij}_{\boldsymbol{\nu},D,\ell m}$. The coupling of the sources to the remaining matching value gives the vector $\mathbf{s}_{\boldsymbol{\nu},\ell m;i}$. The dependence on y_Σ is then governed by the interface Hessian $\mathcal{K}^{\Sigma}_{\boldsymbol{\nu},B,\ell}$ derived in the preceding subsection.

Let n_ℓ denote the dimension of the matching vector in this harmonic block. The regulated bosonic source functional is

$$\begin{aligned} Z^{(2)}_{\boldsymbol{\nu},B,\ell m}[J;\delta] &= \frac{\mathfrak{n}_{\boldsymbol{\nu},\ell m}}{\sqrt{\det \mathcal{H}_{\boldsymbol{\nu},L,D,\ell}\,\det \mathcal{H}_{\boldsymbol{\nu},R,D,\ell}}} \exp\left[\frac{1}{2}J_i\left(\mathcal{V}^{ij}_{\boldsymbol{\nu},\ell m}+G^{ij}_{\boldsymbol{\nu},D,\ell m}\right)J_j\right] \\ &\quad\times\int \frac{\mathrm{d}^{n_\ell}y_\Sigma}{(2\pi)^{n_\ell/2}} \exp\left[-\frac{1}{2}y_\Sigma^T\mathcal{K}^{\Sigma}_{\boldsymbol{\nu},B,\ell}(0;\delta)y_\Sigma + J_i\mathbf{s}^T_{\boldsymbol{\nu},\ell m;i}y_\Sigma\right] \\ &= \frac{\mathfrak{n}_{\boldsymbol{\nu},\ell m}}{\sqrt{\det \mathcal{H}_{\boldsymbol{\nu},L,D,\ell}\,\det \mathcal{H}_{\boldsymbol{\nu},R,D,\ell}\,\det \mathcal{K}^{\Sigma}_{\boldsymbol{\nu},B,\ell}(0;\delta)}} \exp\left[\frac{1}{2}J_i\mathcal{R}^{ij}_{\boldsymbol{\nu},\ell m}J_j\right]. \end{aligned} \tag{B.32}$$

The normalization $\mathfrak{n}_{\boldsymbol{\nu},\ell m}$ contains the Jacobian of the decomposition and the regulated integration measure. It equals unity in normalized Cartesian block coordinates. Equation (B.32) is the bosonic harmonic block; the classical saddle weight, fermions, ghosts, exact modes, and the remaining source-independent factors enter in the full assembly below.

The connected quadratic response of this harmonic is

$$\mathcal{R}^{ij}_{\boldsymbol{\nu},\ell m} = \mathcal{V}^{ij}_{\boldsymbol{\nu},\ell m} + G^{ij}_{\boldsymbol{\nu},D,\ell m} + \mathbf{s}^T_{\boldsymbol{\nu},\ell m;i}\left[\mathcal{K}^{\Sigma}_{\boldsymbol{\nu},B,\ell}(0;\delta)\right]^{-1}\mathbf{s}_{\boldsymbol{\nu},\ell m;j}. \tag{B.33}$$

The three terms correspond respectively to the direct source coupling, propagation inside the two Dirichlet interiors, and propagation through the common matching value.

Equation (B.33) follows from the shift

$$y_\Sigma \longrightarrow y_\Sigma + \left(\mathcal{K}^{\Sigma}_{\boldsymbol{\nu},B,\ell}\right)^{-1}\sum_i J_i\mathbf{s}_{\boldsymbol{\nu},\ell m;i}. \tag{B.34}$$

Completing the square generates simultaneously the interface contribution to the source response and the factor $\left(\det \mathcal{K}^{\Sigma}_{\boldsymbol{\nu},B,\ell}\right)^{-1/2}$. Thus the determinant gluing and the matching-surface covariance arise from the same Gaussian integration. The next subsection assembles these harmonic blocks and converts the finite determinant identity into the regulated functional determinant of the complete quadratic problem.

B.4 Assembly, functional determinants, and the full source coefficient

I now assemble the harmonic blocks into the regulated quadratic functional. At scalar-harmonic cutoff $L_{\max}$, the matching space is the direct sum over (ℓ, m), and its Hessian is

$$\mathcal{K}^{\Sigma,[L_{\max}]}_{\boldsymbol{\nu},B}(\delta) = \bigoplus_{\ell=0}^{L_{\max}}\bigoplus_{m=1}^{(\ell+1)^2}\mathcal{K}^{\Sigma}_{\boldsymbol{\nu},B,\ell}(0;\delta). \tag{B.35}$$

Gauge directions and collective modes are removed on the compatible reduced space. The remaining spin sectors contribute analogous direct-sum blocks. At fixed regulator, determinants multiply across these blocks, inverses act blockwise, and the matching-surface source vector is the direct sum of the vectors $\mathbf{s}_{\boldsymbol{\nu},\ell m;i}$.

Suppressing the angular cutoff, the assembled connected response is

$$\mathcal{R}^{ij}_{\boldsymbol{\nu}} = \mathcal{V}^{ij}_{\boldsymbol{\nu}} + G^{ij}_{\boldsymbol{\nu},D} + \mathbf{s}^{\dagger}_{\boldsymbol{\nu},i}\left(\mathcal{K}^{\Sigma}_{\boldsymbol{\nu},B}\right)^{-1}\mathbf{s}_{\boldsymbol{\nu},j}, \qquad G^{ij}_{\boldsymbol{\nu},D} = \sum_{\ell,m} G^{ij}_{\boldsymbol{\nu},D,\ell m}. \tag{B.36}$$

Here $\mathcal{V}_{\boldsymbol{\nu}}^{ij}$ contains each direct quadratic source term once. A physical source may excite several harmonics, and multiplication of their Gaussian functionals adds their connected quadratic responses. The harmonic labels (ℓ, m) remain independent of the charge label $\boldsymbol{\nu}$.

The finite-dimensional determinant products acquire a definite regularized meaning in the continuum. For a positive elliptic operator T with nonzero discrete spectrum, let q_T denote its mass dimension and form the dimensionless operator $T/\mu_{\mathrm{ren}}^{q_T}$. I define

$$\zeta_T(s;\mu_{\mathrm{ren}}) = \mathrm{Tr}'\left(\frac{T}{\mu_{\mathrm{ren}}^{q_T}}\right)^{-s}, \qquad \log\det{}'_\zeta\left(\frac{T}{\mu_{\mathrm{ren}}^{q_T}}\right) = -\,\partial_s\zeta_T(s;\mu_{\mathrm{ren}})|_{s=0}\,. \tag{B.37}$$

The trace is defined first in its convergence domain and then continued to $s = 0$. A pole at $s = 0$ is treated by the chosen finite-part prescription. For a complex elliptic operator, the same construction uses a fixed spectral cut. A second-order bulk Hessian and the first-order Dirichlet-to-Neumann operator on Σ carry different mass dimensions and therefore require their own powers of μ_{ren}. The symbol ζ here denotes the regularization scheme.

At finite outer radius, the bosonic gluing theorem relates the full operator to the two Dirichlet interiors and the matching-surface operator. For an invertible elliptic boundary-value problem,

$$\det_\zeta \mathcal{H}_{\boldsymbol{\nu},B}(\delta) = \mathrm{e}^{\mathcal{L}_{\boldsymbol{\nu},\mathrm{loc}}(\delta)} \det_\zeta \mathcal{H}_{\boldsymbol{\nu},L,D}(\delta) \det_\zeta \mathcal{H}_{\boldsymbol{\nu},R,D}(\delta) \det_\zeta \mathcal{K}^{\Sigma}_{\boldsymbol{\nu},B}(\delta). \tag{B.38}$$

Each determinant carries the dimensionless normalization appropriate to its operator. The local factor $\mathcal{L}_{\boldsymbol{\nu},\mathrm{loc}}$ is fixed by the operator and its boundary conditions and survives the continuum gluing relation [10–12]. In finite Cartesian block algebra this local factor vanishes and the ordinary Schur-complement determinant identity is recovered.

For a noncompact outer limit, I define the determinants by the same relative-determinant or subtraction-and-counterterm prescription on all three factors. When kernels occur, I first introduce a common spectral shift, apply Eq. (B.38) to the invertible problem, and then extract the zero-mode powers together with their compatible kernel measures. This procedure preserves the finite kernel factors generated by gluing.

The fermionic sector requires its own first-order boundary split. At the same regulator, elimination of the complementary Grassmann coordinates produces

$$\mathrm{Pf}\mathcal{D}_{\boldsymbol{\nu},F,Q_D}\,\mathrm{Pf}M^{\Sigma}_{\boldsymbol{\nu},F},$$

with a fixed Berezin orientation. I collect ghosts, self-dual sectors, exact-mode measures, prescribed zero-mode saturation factors, counterterms, fermionic gluing normalizations, and all remaining source-independent factors into $\mathcal{Z}_{\boldsymbol{\nu},\mathrm{rem}}$. The source-independent contribution from the two Dirichlet interiors is then

$$\mathcal{A}_{\boldsymbol{\nu},D} = \mathcal{Z}_{\boldsymbol{\nu},\mathrm{rem}}\,\mathfrak{n}_{\boldsymbol{\nu}}\,\mathrm{e}^{-\mathcal{L}_{\boldsymbol{\nu},\mathrm{loc}}/2}\frac{\mathrm{Pf}\mathcal{D}_{\boldsymbol{\nu},F,Q_D}}{\sqrt{|\det_\zeta \mathcal{H}_{\boldsymbol{\nu},L,D}\,\det_\zeta \mathcal{H}_{\boldsymbol{\nu},R,D}|}}. \tag{B.39}$$

At finite regulator, the zeta determinants in Eq. (B.39) are replaced by the corresponding ordinary determinants. The factor $\mathfrak{n}_{\boldsymbol{\nu}}$ collects the regulated change-of-variable and measure Jacobians. In normalized Cartesian coordinates, $\mathfrak{n}_{\boldsymbol{\nu}} = 1$ and $\mathcal{L}_{\boldsymbol{\nu},\mathrm{loc}} = 0$. For a real self-adjoint problem, the absolute values display the Gaussian magnitude while the contour phase resides in $\mathcal{Z}_{\boldsymbol{\nu},\mathrm{rem}}$. For a complex saddle, the chosen determinant branches replace this notation.

After removing the classical exponential, the assembled quadratic source functional is

$$\widehat{Z}^{(2)}_{\boldsymbol{\nu}}[J;\delta] = \underbrace{\mathcal{A}_{\boldsymbol{\nu},D}\frac{\mathrm{Pf}M^{\Sigma}_{\boldsymbol{\nu},F}}{\sqrt{|\det\mathcal{K}^{\Sigma}_{\boldsymbol{\nu},B}|}}}_{\widehat{Z}^{(2)}_{\boldsymbol{\nu}}[0;\delta]} \exp\left[\frac{1}{2}J_i\mathcal{R}^{ij}_{\boldsymbol{\nu}}J_j\right]. \tag{B.40}$$

Its Gaussian contribution to the unnormalized two-source coefficient is therefore

$$\widehat{C}^{ij}_{\boldsymbol{\nu}} = \mathcal{A}_{\boldsymbol{\nu},D}\frac{\mathrm{Pf}\,M^{\Sigma}_{\boldsymbol{\nu},F}}{\sqrt{\left|\det \mathcal{K}^{\Sigma}_{\boldsymbol{\nu},B}\right|}}\left[\mathcal{V}^{ij}_{\boldsymbol{\nu}} + G^{ij}_{\boldsymbol{\nu},D} + \mathbf{s}^{\dagger}_{\boldsymbol{\nu},i}\big(\mathcal{K}^{\Sigma}_{\boldsymbol{\nu},B}\big)^{-1}\mathbf{s}_{\boldsymbol{\nu},j}\right] + \widehat{C}^{ij}_{\boldsymbol{\nu},\mathrm{higher}}. \tag{B.41}$$

The bracket is the connected Gaussian response $\mathcal{R}^{ij}_{\boldsymbol{\nu}}$. Its prefactor is the complete quadratic weight $\widehat{Z}^{(2)}_{\boldsymbol{\nu}}[0;\delta]$. The first term in Eq. (B.41) follows by differentiating Eq. (B.40); the final term collects interaction corrections and source-dependent insertions from the full functional.

This assembly preserves the distinction between determinant weight and inverse response. The same interface matrix $\mathcal{K}^{\Sigma}_{\boldsymbol{\nu},B}$ enters the former through its determinant and the latter through its inverse. The next reduction acts on the matching trace itself and produces the smaller physical boundary block used in the finite-radius and spectral analysis.

B.5 Further boundary elimination

The matching-surface field generally contains more components than the final observable requires. Split the trace coordinates as

$$y_{\Sigma} = (x, v), \tag{B.42}$$

where $x = P_R y_{\Sigma}$ denotes the retained trace variables and v denotes the complementary trace variables. The projector P_R acts on the finite matching space. It is distinct from the bulk projector P_B of Appendix A.3, which acts before radial elimination.

In fixed (x, v) coordinates, write

$$\mathcal{K}^{\Sigma}_{\boldsymbol{\nu},B} = \begin{pmatrix} \mathsf{A} & \mathsf{B} \\ \mathsf{C} & \mathsf{D} \end{pmatrix}, \qquad \mathbf{s}_i = \begin{pmatrix} \mathbf{s}_{i,x} \\ \mathbf{s}_{i,v} \end{pmatrix}. \tag{B.43}$$

For invertible D, stationarity in v gives

$$v = -\mathsf{D}^{-1}\mathsf{C}x + \mathsf{D}^{-1}\mathbf{s}_{i,v}J_i. \tag{B.44}$$

Substitution produces the reduced trace Hessian

$$M^{\Sigma}_{B} = \mathsf{A} - \mathsf{B}\mathsf{D}^{-1}\mathsf{C}. \tag{B.45}$$

The same elimination gives

$$\mathbf{s}^{\mathrm{eff}}_i = \mathbf{s}_{i,x} - \mathsf{B}\mathsf{D}^{-1}\mathbf{s}_{i,v}, \tag{B.46}$$

the contact response

$$\mathbf{s}^{\dagger}_{i,v}\mathsf{D}^{-1}\mathbf{s}_{j,v}, \tag{B.47}$$

and the Gaussian determinant factor $(\det \mathsf{D})^{-1/2}$. The reduced Hessian, effective source, contact response, and determinant therefore form one Schur-complement operation.

This reduction also fixes the first finite-radius deformation of the retained matrix. Keep the (x, v) coordinates fixed as δ varies and let subscripts $0, 1$ denote the endpoint value and first derivative. Differentiating Eq. (B.45) gives

$$\begin{aligned} M_1 = {} & \mathsf{A}_1 - \mathsf{B}_1\mathsf{D}_0^{-1}\mathsf{C}_0 - \mathsf{B}_0\mathsf{D}_0^{-1}\mathsf{C}_1 \\ & + \mathsf{B}_0\mathsf{D}_0^{-1}\mathsf{D}_1\mathsf{D}_0^{-1}\mathsf{C}_0. \end{aligned} \tag{B.48}$$

For a Hermitian quadratic form, define the endpoint stationary extension

$$\mathfrak{J}_0 x = \begin{pmatrix} x \\ -\mathsf{D}_0^{-1}\mathsf{C}_0 x \end{pmatrix}. \tag{B.49}$$

Then

$$M_1 = \mathfrak{J}_0^\dagger (\mathcal{K}^\Sigma)_1 \mathfrak{J}_0. \tag{B.50}$$

Equation (B.50) is the stationary-value derivative of the complete trace quadratic form. When the stationary extension is differentiated, the terms containing $\partial_\delta \mathfrak{J}_\delta$ cancel because the action is stationary in the eliminated v direction. The surviving term is therefore the explicit derivative of the complete quadratic form evaluated on the endpoint stationary extension. Expanding Eq. (B.50) gives Eq. (B.48).

If the retained subspace is an exact endpoint kernel, self-adjointness makes the endpoint mixed blocks vanish, $\mathsf{B}_0 = \mathsf{C}_0 = 0$. Equation (B.50) then reduces to the direct projection of $(\mathcal{K}^\Sigma)_1$ onto that kernel. This is the trace-space version of the endpoint projection used in Appendix A.3.

The successive reductions used above are associative.

Order independence of elimination. Let x denote the final retained coordinates, v additional trace coordinates, and u interior coordinates. Assume that every block inverted in the successive eliminations is invertible. With one fixed coordinate system, measure, and source functional, eliminating u and then v gives the same effective Hessian, source vector, contact response, and Gaussian normalization as eliminating (v, u) in one step.

To see this, in real coordinates, write

$$H = \begin{pmatrix} H_{xx} & H_{xv} & H_{xu} \\ H_{vx} & H_{vv} & H_{vu} \\ H_{ux} & H_{uv} & H_{uu} \end{pmatrix}, \qquad \mathbf{b}_i = (\mathbf{b}_{i,x}, \mathbf{b}_{i,v}, \mathbf{b}_{i,u}). \tag{B.51}$$

Set $y = (x, v)$. Eliminating u first gives

$$K = H_{yy} - H_{yu} H_{uu}^{-1} H_{uy}, \tag{B.52}$$

$$\mathbf{s}_i = \mathbf{b}_{i,y} - H_{yu} H_{uu}^{-1} \mathbf{b}_{i,u}, \tag{B.53}$$

$$G_D^{ij} = \mathbf{b}_{i,u}^T H_{uu}^{-1} \mathbf{b}_{j,u}. \tag{B.54}$$

Decompose K on (x, v) as in Eq. (B.43). Eliminating v then gives

$$M = \mathsf{A} - \mathsf{B}\mathsf{D}^{-1}\mathsf{C}, \tag{B.55}$$

$$\mathbf{b}_i^{\mathrm{eff}} = \mathbf{s}_{i,x} - \mathsf{B}\mathsf{D}^{-1}\mathbf{s}_{i,v}, \tag{B.56}$$

$$G_Q^{ij} = G_D^{ij} + \mathbf{s}_{i,v}^T \mathsf{D}^{-1} \mathbf{s}_{j,v}. \tag{B.57}$$

Now combine the eliminated coordinates as $w = (v, u)$. Their stationary equation is

$$w = H_{ww}^{-1}\big(J_i \mathbf{b}_{i,w} - H_{wx} x\big). \tag{B.58}$$

Direct elimination gives

$$M = H_{xx} - H_{xw} H_{ww}^{-1} H_{wx}, \tag{B.59}$$

$$\mathbf{b}_i^{\mathrm{eff}} = \mathbf{b}_{i,x} - H_{xw} H_{ww}^{-1} \mathbf{b}_{i,w}, \tag{B.60}$$

$$G_Q^{ij} = \mathbf{b}_{i,w}^T H_{ww}^{-1} \mathbf{b}_{j,w}. \tag{B.61}$$

Both procedures solve the same stationary equations with the same retained coordinate x. Uniqueness therefore gives identical stationary solutions and identical quadratic forms in x and J. The determinant identity

$$\det H = \det H_{uu} \, \det \mathsf{D} \, \det M = \det H_{ww} \, \det M \tag{B.62}$$

gives the same Gaussian normalization. Thus the effective matrix, source vector, and contact response agree in the same retained coordinates.

Under a real invertible reparameterization $x = T\widetilde{x}$,

$$\widetilde{M} = T^{\dagger} M T, \qquad \widetilde{\mathbf{b}}_i^{\mathrm{eff}} = T^{\dagger}\mathbf{b}_i^{\mathrm{eff}}, \qquad \mathrm{d}x = |\det T|\,\mathrm{d}\widetilde{x}. \tag{B.63}$$

The Gaussian functional is invariant under this simultaneous transformation. Equality of individual matrix entries therefore refers to one fixed coordinate system.

This order-independence statement connects the interface construction to the physical outer-boundary Hessian. Retain the asymptotic values (q_L, q_R) and eliminate both radial interiors together with every artificial matching variable. The resulting quadratic matrix is $\mathcal{K}^{\partial}_{\boldsymbol{\nu},B}$. One may perform these eliminations sequentially or in a single Schur complement; the reconstructed outer functional is identical.

This statement also fixes the role of the artificial cut. Moving Σ changes the one-sided Dirichlet factors, $\mathcal{K}^{\Sigma}_{\boldsymbol{\nu},B}$, and the induced matching-surface sources. Their assembled outer-boundary functional remains fixed. For example, a free scalar on a unit interval cut at r has

$$K^{\Sigma}(r) = \frac{1}{r} + \frac{1}{1-r}. \tag{B.64}$$

The interface Hessian varies explicitly with r, while elimination of the interface reproduces the same fixed endpoint functional for every $0 < r < 1$. The physical object is therefore $\mathcal{K}^{\partial}_{\boldsymbol{\nu},B}$ and its associated source response. The matrix $\mathcal{K}^{\Sigma}_{\boldsymbol{\nu},B}$ is the intermediate gluing operator that constructs it.

B.6 Charge sensitivities of the radial problem

The preceding construction determines the response in one fixed charge sector. To compare neighboring sectors while preserving the same boundary prescription, I differentiate the background and radial boundary-value problem with respect to the charge data.

Introduce independent symmetric bilinears t_{ij}, $i \le j$, through

$$U(t,\phi) = \sum_{i\le j} t_{ij}\,\mathcal{U}_{ij}(\phi), \qquad \mathcal{U}_{ij} = (2-\delta_{ij})\mathcal{G}^{ij}_{\chi}(\phi). \tag{B.65}$$

The physical charge sectors lie on the rank-one locus

$$t_{ij} = \nu_i \nu_j.$$

I first differentiate in the independent symmetric variables t_{ij} and then restrict the result to this physical locus. This procedure resolves changes in the relative charge components without conflating them with changes of boundary data.

Let t_A denote one such charge parameter. Every derivative ∂_A below includes both the explicit t_A-dependence of the radial coefficients and the induced t_A-dependence of the background solution at fixed prescribed outer data. For real spectral parameter z, define

$$R_\ell = A_\ell^{-1}, \qquad D_\ell = B_\ell - \mathcal{N}. \tag{B.66}$$

The Riccati equation (B.26) becomes

$$\dot{\mathcal{N}} = C_\ell - zW_\ell - D_\ell^{\dagger} R_\ell D_\ell. \tag{B.67}$$

Using

$$\partial_A R_\ell = -R_\ell(\partial_A A_\ell)R_\ell, \tag{B.68}$$

the first sensitivity

$$\mathcal{N}_A \equiv \partial_A \mathcal{N} \tag{B.69}$$

satisfies the linear inhomogeneous equation

$$\dot{\mathcal{N}}_A = D_\ell^\dagger R_\ell \mathcal{N}_A + \mathcal{N}_A R_\ell D_\ell + \mathcal{S}_A, \tag{B.70}$$

with

$$\begin{aligned}\mathcal{S}_A = \partial_A C_\ell - z\,\partial_A W_\ell - (\partial_A B_\ell)^\dagger R_\ell D_\ell - D_\ell^\dagger R_\ell (\partial_A B_\ell) \\ + D_\ell^\dagger R_\ell (\partial_A A_\ell) R_\ell D_\ell.\end{aligned} \tag{B.71}$$

Thus the charge derivative of the nonlinear Riccati problem reduces to a linear transport equation once the original radial solution is known. Its boundary condition follows by differentiating the same prescribed outer-boundary condition used to construct $\mathcal{N}$.

For complex z, I differentiate the ordered Riccati equation directly. The two factors flanking R_ℓ then retain their displayed ordering rather than being related by Hermitian conjugation. Successive charge derivatives obey linear inhomogeneous equations whose sources are determined recursively by the lower derivatives.

The two one-sided sensitivities assemble at the artificial interface in the same way as the original maps. At fixed Σ and in fixed trace coordinates,

$$\partial_A \mathcal{K}^\Sigma_{\boldsymbol{\nu},B,\ell} = \partial_A \mathcal{N}^{\mathrm{out}}_{\boldsymbol{\nu},L,\ell} + \partial_A \mathcal{N}^{\mathrm{out}}_{\boldsymbol{\nu},R,\ell} + \partial_A \mathcal{B}_{\boldsymbol{\nu},\Sigma,\ell}. \tag{B.72}$$

If the matching surface moves under the chosen parametrization, its endpoint motion contributes the corresponding boundary-evaluation terms before Eq. (B.72) is applied. Any subsequent trace-space elimination is differentiated with the stationary-extension identity (B.50). After the artificial trace has been removed, this procedure gives the charge sensitivity of the physical outer-boundary Hessian and of its effective source vectors.

The sensitivity equations therefore separate two operations used later in the charge analysis. Uniform charge rescaling in the product system is fixed directly by its homogeneity. Redistribution among charge components moves the target-space trajectory and is computed by Eqs. (B.70)–(B.72). Both comparisons use the same outer data and the same boundary functional.

B.7 The deformation and the observable

The BPS square fixes the endpoint operator, while the finite-radius boundary-value problem fixes its physical deformation. A continuation of the matrix factorization by itself carries no such information. This distinction can be seen directly at finite dimension.

Consider a reduced positive matrix written as

$$M(\delta) = \mathcal{Q}(\delta)^\dagger G_{\mathrm{diff}}(\delta) \mathcal{Q}(\delta) + \Delta(\delta), \qquad G_{\mathrm{diff}}(0) = 1, \qquad \Delta(0) = 0. \tag{B.73}$$

Let

$$M_0 = \mathcal{Q}_0^\dagger \mathcal{Q}_0 > 0. \tag{B.74}$$

For any Hermitian matrix D_1, define

$$R_Q = \frac{1}{2} \mathcal{Q}_0 M_0^{-1} D_1. \tag{B.75}$$

Then

$$(\mathcal{Q}_0 + \delta R_Q)^\dagger (\mathcal{Q}_0 + \delta R_Q) = M_0 + \delta D_1 + O(\delta^2). \tag{B.76}$$

Thus an arbitrary Hermitian first variation can be absorbed into a chosen deformation of the square root. The physical D_1 is instead determined by the gravitational data: the constraints, differential operator, target-space geometry, boundary domain, radial matching, trace elimination, and source map. Equation (B.76) therefore provides a representation of a known deformation, not a rule for deriving it.

Exact symmetries constrain this physical matrix after the boundary problem has been fixed. For a symmetry g of the fixed-charge saddle and its boundary data, choose an orthonormal basis on the retained finite space. Then

$$U(g)M_{\boldsymbol{\nu}}(\delta)U(g)^{-1} = M_{\boldsymbol{\nu}}(\delta). \tag{B.77}$$

Every coefficient in the finite-radius expansion commutes with $U(g)$. Rotational symmetry therefore separates distinct angular representations at quadratic order. The response within each representation remains fixed by its field content, boundary state, and source normalization.

Schur elimination also fixes the sign of a common class of induced deformations. Consider a positive eliminated channel,

$$\mathcal{H}_{\rm ext}(\delta) = \begin{pmatrix} M_0 & \gamma(\delta)V \\ \gamma(\delta)V^\dagger & H_{\rm ch} \end{pmatrix}, \qquad H_{\rm ch} > 0, \qquad \gamma(\delta) \in \mathbb{R}. \tag{B.78}$$

Eliminating that channel gives

$$M_{\rm eff} = M_0 - \gamma(\delta)^2 V H_{\rm ch}^{-1} V^\dagger. \tag{B.79}$$

The induced correction is negative semidefinite. For an indefinite or contour-rotated channel, the same Schur construction uses the continued quadratic form and contour; its sign is then fixed by that physical continuation.

The observable depends on more than the matrix deformation. Let

$$\mathbf{b}^{\rm eff}(\delta) = \mathbf{b}_0 + \delta\mathbf{b}_1 + O(\delta^2), \qquad M(\delta) = M_0 + \delta D_1 + O(\delta^2). \tag{B.80}$$

Differentiating the inverse contraction gives

$$\begin{aligned} \frac{\mathrm{d}}{\mathrm{d}\delta}\left[(\mathbf{b}^{\rm eff})^\dagger M^{-1}\mathbf{b}^{\rm eff}\right]\Big|_0 &= \mathbf{b}_1^\dagger M_0^{-1}\mathbf{b}_0 + \mathbf{b}_0^\dagger M_0^{-1}\mathbf{b}_1 \\ &\quad - \mathbf{b}_0^\dagger M_0^{-1} D_1 M_0^{-1}\mathbf{b}_0. \end{aligned} \tag{B.81}$$

The first two terms measure the motion of the physical source vector. The third measures the deformation of the quadratic matrix itself. For the complete connected response,

$$\mathcal{R}^{ij} = \mathcal{V}^{ij} + G_Q^{ij} + (\mathbf{b}_i^{\rm eff})^\dagger M^{-1}\mathbf{b}_j^{\rm eff}, \tag{B.82}$$

the first variation also contains $\partial_\delta \mathcal{V}^{ij}$ and $\partial_\delta G_Q^{ij}$. For the unnormalized coefficient, the derivative of the zero-source Gaussian weight multiplies this connected response as prescribed by Appendix A. The physical first variation therefore combines the matrix deformation, source motion, complementary propagation, direct source term, and fluctuation normalization.

The three small-δ structures occur at different orders. For the homogeneous physical outer-boundary Hessian,

$$K_{LR} = O(\delta^2), \tag{B.83}$$

while one eigenvalue of K is $O(\delta)$. Inversion converts these two facts into a cross-boundary covariance

$$G_{LR} = O(\delta). \tag{B.84}$$

The coupled $\ell = 3$ sector instead produces the resonant term

$$\delta^2 \log(\delta/\delta_0), \tag{B.85}$$

whose first δ-derivative vanishes at the BPS endpoint. The finite-cut scalar–gravity Hessian encountered in the angular matching problem begins at $O(\delta^3)$ in its own boundary variables. These orders belong to different quadratic objects at different stages of the reduction. The exact radial calculation below identifies each object before any comparison of powers is made.

C Exact radial solution and validity of the expansion

Exact radial matching propagates the near-throat solution to the two asymptotic boundaries and determines the physical boundary Hessian. I first derive the fixed-charge homogeneous quadratic problem in a form that remains regular at the minimal three-sphere.

C.1 Fixed-charge action at the minimal three-sphere

For fixed axion charge in $(d+1)$ Euclidean dimensions, take round S^d slices,

$$\mathrm{d}s^2 = N(\tau)^2 \mathrm{d}\tau^2 + a(\tau)^2 \mathrm{d}\Omega_d^2. \tag{C.1}$$

Let ϕ^A denote the dilaton/saxions with target metric G_{AB}. The axion kinetic matrix is $\mathcal{G}^{\chi}_{ij}$ and its inverse is $\mathcal{G}_{\chi}^{ij}$. After fixing the conserved axion momenta ν_i, the Legendre transform produces the charge potential

$$U_{\boldsymbol{\nu}}(\phi) = \nu_i \mathcal{G}_{\chi}^{ij}(\phi) \nu_j. \tag{C.2}$$

The homogeneous fixed-charge Euclidean action is

$$I_R = \frac{\mathcal{V}_d}{2\kappa_{d+1}^2} \int \mathrm{d}\tau \left[-\frac{d(d-1)a^{d-2}}{N}(a')^2 - d(d-1)Na^{d-2} + 2\Lambda N a^d \right.$$
$$\left. + \frac{a^d}{2N} G_{AB}(\phi)\phi^{A\prime}\phi^{B\prime} + \frac{N}{2a^d} U_{\boldsymbol{\nu}}(\phi) \right] + I_{\mathrm{outer}} + I_{\Sigma}. \tag{C.3}$$

Here $\mathcal{V}_d = \mathrm{Vol}(S^d)$. I use the Einstein–Hilbert convention $-\int \sqrt{g}\,(R - 2\Lambda)$. All explicit small-radius solutions below use $\Lambda = 0$.

Before the charge Legendre transform, the axion contribution is

$$-\frac{\mathcal{V}_d}{2\kappa_{d+1}^2} \frac{a^d}{2N} \mathcal{G}^{\chi}_{ij} \chi^{i\prime} \chi^{j\prime}. \tag{C.4}$$

After removing the common prefactor, its canonical momentum is

$$p_{\chi,i} = -\frac{a^d}{N} \mathcal{G}^{\chi}_{ij} \chi^{j\prime}.$$

I identify the fixed canonical momenta with ν_i. The Routhian $L - p_{\chi,i}\chi^{i\prime}$ then gives the positive term $NU_{\boldsymbol{\nu}}/(2a^d)$ in Eq. (C.3). This fixes the Euclidean sign used throughout the fixed-charge calculation.

Remove the common factor $\mathcal{V}_d/(2\kappa_{d+1}^2)$ and define

$$p_a = -2d(d-1)a^{d-2}\frac{a'}{N}, \qquad p_A = \frac{a^d}{N} G_{AB}\phi^{B\prime}. \tag{C.5}$$

Variation of the lapse gives the Hamiltonian constraint

$$\mathcal{H} = -\frac{p_a^2}{4d(d-1)a^{d-2}} + \frac{1}{2a^d}G^{AB}p_A p_B + d(d-1)a^{d-2} - 2\Lambda a^d - \frac{U_{\boldsymbol{\nu}}}{2a^d} = 0. \tag{C.6}$$

In four dimensions, take one scalar σ, set $\Lambda = 0$, and use proper-radial gauge $N = 1$. The scalar equation has the first integral

$$(a^3\sigma')^2 - U_{\boldsymbol{\nu}}(\sigma) = -E, \qquad (a')^2 = 1 - \frac{E}{12a^4}. \tag{C.7}$$

The second relation follows immediately by inserting the first into Eq. (C.6). For $E > 0$, the turning point satisfies $E = 12a_*^4$. These equations reproduce the radial system of Ref. [5] and fix the normalization used below.

I now reduce the homogeneous scalar–gravity system directly at the minimal sphere. I solve the Hamiltonian constraint for the momentum along the background scalar trajectory and retain the scale factor and transverse dilaton/saxions as canonical variables.

Choose coordinates (σ, s^u) in a tubular neighborhood of the background trajectory, with $s^u = 0$ on that trajectory. At the trajectory take

$$G_{\sigma\sigma} = 1, \qquad G_{\sigma u} = 0, \qquad p_u = 0, \qquad \sigma' \neq 0. \tag{C.8}$$

These relations fix the metric only on the trajectory. Derivatives of the target metric remain in the quadratic fluctuation problem for a general target space.

Multiplying Eq. (C.6) by $2a^d$ and isolating the scalar momentum defines

$$\mathcal{R} = \frac{a^2 p_a^2}{2d(d-1)} - 2d(d-1)a^{2d-2} + 4\Lambda a^{2d} + U_{\boldsymbol{\nu}}. \tag{C.9}$$

The constraint is quadratic in p_σ. Its two branches are

$$p_\sigma = \frac{-G^{\sigma u}p_u + \varsigma\sqrt{(G^{\sigma u}p_u)^2 + G^{\sigma\sigma}\left(\mathcal{R} - G^{uv}p_u p_v\right)}}{G^{\sigma\sigma}}, \qquad \varsigma = \pm 1. \tag{C.10}$$

Gauge fixing $\sigma(\tau) = \bar{\sigma}(\tau)$ turns the constrained action into

$$I_{\rm red} = \frac{\mathcal{V}_d}{2\kappa_{d+1}^2}\int \mathrm{d}\tau\ [p_m x^{m\prime} + \bar{\sigma}' p_\sigma] + I_{\rm outer} + I_\Sigma,$$

where $x^m = (a, s^u)$. For a general target metric, the second variation of this expression contains derivatives of $G^{\sigma\sigma}$, $G^{\sigma u}$, and G^{uv}.

The explicit calculation below uses a target metric that is locally a product along the scaling direction,

$$\mathrm{d}\ell^2 = \mathrm{d}\sigma^2 + G_{uv}(s)\mathrm{d}s^u\mathrm{d}s^v.$$

Equation (C.10) then reduces to

$$p_\sigma = \varsigma F, \qquad F = \sqrt{\Xi}, \tag{C.11}$$

with

$$\Xi = \frac{a^2 p_a^2}{2d(d-1)} - G^{uv}p_u p_v - 2d(d-1)a^{2d-2} + 4\Lambda a^{2d} + U_{\boldsymbol{\nu}}(\sigma, s). \tag{C.12}$$

The sign ς selects the branch of the constrained Hamiltonian. On an interval where σ is monotonic, define

$$\omega \equiv \varsigma\bar{\sigma}' > 0. \tag{C.13}$$

On the background, $\varsigma = \operatorname{sgn} p_\sigma = \operatorname{sgn} \bar{\sigma}'$. The reduced first-order action becomes

$$I_{\rm red} = \frac{\mathcal{V}_d}{2\kappa_{d+1}^2} \int \mathrm{d}\tau \; [p_m x^{m\prime} + \omega F(x, p; \bar{\sigma}, \boldsymbol{\nu})] + I_{\rm outer} + I_\Sigma. \tag{C.14}$$

This constraint reduction leaves the scale-factor fluctuation explicit and remains regular at the turning point $a' = 0$ as long as $p_\sigma \neq 0$.

Let Q^m and P_m denote fluctuations of x^m and p_m. Let F_{xx}, F_{xp}, and F_{pp} denote the corresponding Hessian blocks of F, evaluated on the background. When the transverse frame varies along the trajectory, its connection is included in $D_\tau Q$. The quadratic first-order action is

$$I^{(2)}_{\rm hom} = \frac{\mathcal{V}_d}{4\kappa_{d+1}^2} \int \mathrm{d}\tau \left[2P^T D_\tau Q + \omega Q^T F_{xx} Q + 2\omega Q^T F_{xp} P + \omega P^T F_{pp} P \right] + I^{(2)}_{\rm hom,bdy}. \tag{C.15}$$

This first-order form is the regular description of the constrained homogeneous fluctuation problem. On any patch where F_{pp} is invertible, stationarity in P gives

$$P = -F_{pp}^{-1} \left(\omega^{-1} D_\tau Q + F_{px} Q \right). \tag{C.16}$$

Substituting Eq. (C.16) yields

$$I^{(2)}_{\rm hom} = \frac{\mathcal{V}_d}{4\kappa_{d+1}^2} \int \mathrm{d}\tau \; \left[-\frac{1}{\omega} \left(D_\tau Q + \omega F_{px} Q \right)^T F_{pp}^{-1} \left(D_\tau Q + \omega F_{px} Q \right) + \omega Q^T F_{xx} Q \right] + I^{(2)}_{\rm hom,bdy}. \tag{C.17}$$

In a parallel transverse frame, comparison with the radial action in Eq. (B.21) gives

$$A = -\frac{1}{\omega} F_{pp}^{-1}, \qquad B = -F_{pp}^{-1} F_{px}, \qquad C = \omega \left(F_{xx} - F_{xp} F_{pp}^{-1} F_{px} \right). \tag{C.18}$$

The matrices in Eq. (C.18) acquire the common factor $\mathcal{V}_d/(2\kappa_{d+1}^2)$ when inserted into Eq. (B.21). For a non-product target metric, the corresponding coefficients follow from the Hessian of $\bar{\sigma}' p_\sigma$ in Eq. (C.10).

On the background,

$$F = |p_\sigma| = a^d \omega, \qquad p_a = -2d(d-1) a^{d-2} a'. \tag{C.19}$$

The momentum Hessian separates into the scale-factor and transverse blocks,

$$F_{p_a p_a} = \frac{a^2 \omega^2 - 2d(d-1)(a')^2}{2d(d-1) a^d \omega^3}, \tag{C.20}$$

$$F_{p_u p_v} = -\frac{G^{uv}}{a^d \omega}, \qquad F_{p_a p_u} = 0. \tag{C.21}$$

At the minimal three-sphere, $a' = 0$. For the branch with $p_\sigma \neq 0$, one has $\omega \neq 0$, so both blocks of F_{pp} are invertible. Equation (C.18) then gives, before the common gravitational normalization is restored,

$$A_{aa}\big|_* = -2d(d-1) a_*^{d-2}, \qquad A_{uv}\big|_* = a_*^d G_{uv}, \qquad A_{au}\big|_* = 0. \tag{C.22}$$

The scale-factor kinetic term carries the gravitational conformal sign, whereas the transverse dilaton/saxion block is positive for $G_{uv} > 0$. I integrate the scale direction on the gravitational

contour. Zero crossings of the physical reduced quadratic form control changes of the Gaussian contour phase.

Away from the minimal sphere, the second-order representation Eq. (C.17) becomes singular when

$$a^2\omega^2 - 2d(d-1)(a')^2 = 0. \tag{C.23}$$

This is a singularity of the elimination of P_a. The first-order system (C.15) remains the canonical continuation through such a point. Equivalently, one may solve the Hamiltonian constraint using another monotonic field as the clock. Both descriptions reconstruct the same outer boundary map.

The four-dimensional one-scalar truncation makes the scalar–gravity block explicit. For $d = 3$,

$$F(a, p_a; \sigma) = \sqrt{\frac{a^2 p_a^2}{12} - 12a^4 + 4\Lambda a^6 + U_{\boldsymbol{\nu}}(\sigma)}. \tag{C.24}$$

With $\omega = |\sigma'|$, $F = a^3\omega$, and $f \equiv Q^a$, Eq. (C.17) becomes

$$I^{(2)}_{\rm hom} = \frac{\mathcal{V}_3}{4\kappa_4^2}\int \mathrm{d}\tau\, \left[-\frac{1}{\omega F_{p_a p_a}}\left(f' + \omega F_{p_a a} f\right)^2 + \omega F_{aa} f^2\right] + I^{(2)}_{\rm hom,bdy}. \tag{C.25}$$

All partial derivatives of F are taken at fixed σ and fixed remaining canonical variables. Define

$$\mathcal{R}_4 = \frac{a^2 p_a^2}{12} - 12a^4 + 4\Lambda a^6 + U_{\boldsymbol{\nu}}(\sigma), \qquad F = \sqrt{\mathcal{R}_4}. \tag{C.26}$$

Direct differentiation gives

$$F_{p_a p_a} = \frac{a^2}{12F} - \frac{a^4 p_a^2}{144F^3}, \tag{C.27}$$

$$F_{p_a a} = \frac{a p_a}{6F} - \frac{a^2 p_a (\mathcal{R}_4)_a}{24F^3}, \tag{C.28}$$

$$F_{aa} = \frac{(\mathcal{R}_4)_{aa}}{2F} - \frac{(\mathcal{R}_4)_a^2}{4F^3}, \tag{C.29}$$

$$(\mathcal{R}_4)_a = \frac{a p_a^2}{6} - 48a^3 + 24\Lambda a^5, \qquad (\mathcal{R}_4)_{aa} = \frac{p_a^2}{6} - 144a^2 + 120\Lambda a^4. \tag{C.30}$$

At the minimal sphere $p_a = 0$, hence $F_{p_a a} = 0$. Using Eq. (C.22), the local quadratic density becomes

$$\mathcal{L}^{(2)}_{\rm hom}\Big|_* = \frac{\mathcal{V}_3}{4\kappa_4^2}\left[-12a_*(f')^2 + \omega_* F_{aa}\big|_*\, f^2\right]. \tag{C.31}$$

Equation (C.31) gives the local form at the minimal sphere. The radial propagation is governed by Eq. (C.25). After the Hamiltonian constraint and scalar-clock gauge are imposed, the one-axion–dilaton truncation leaves one homogeneous scalar–gravity degree of freedom. Additional dilaton/saxions, form fields, harmonics, and internal modes enlarge this reduced quadratic system.

For several axions, all explicit charge dependence begins with

$$U_{\boldsymbol{\nu}}(\phi) = \nu_i \mathcal{G}^{ij}_\chi(\phi)\nu_j, \tag{C.32}$$

and therefore

$$\nabla_u\nabla_v U_{\boldsymbol{\nu}} = \nu_i \nabla_u\nabla_v \mathcal{G}^{ij}_\chi(\phi)\nu_j. \tag{C.33}$$

Introduce the independent symmetric bilinears t_{ij} of Appendix B. At a fixed phase-space point,

$$\frac{\partial F}{\partial t_{ij}} = \frac{(2-\delta_{ij})\mathcal{G}^{ij}_\chi(\phi)}{2F}, \qquad i \le j. \tag{C.34}$$

The factor 2 for $i < j$ restores the two off-diagonal entries of the original double sum. The physical charge sensitivities follow by differentiating the background together with Eqs. (C.18) and (C.34) at fixed outer data.

At $p_u = 0$, the transverse Hessian of the square-root Hamiltonian is

$$\omega F_{;uv} = \frac{1}{2a^d}\nabla_u\nabla_v U_{\boldsymbol{\nu}} - \frac{1}{4a^{3d}\omega^2}(\nabla_u U_{\boldsymbol{\nu}})(\nabla_v U_{\boldsymbol{\nu}}). \tag{C.35}$$

On the stationary transverse trajectory used below, $\nabla_u U_{\boldsymbol{\nu}} = 0$, so the second term vanishes. For a general target metric, Eq. (C.10) supplies the additional derivatives of the inverse target metric.

At fixed (a, ω, ϕ), the two numerators in Eq. (C.35) carry quadratic and quartic charge dependence, respectively. The background itself moves with $\boldsymbol{\nu}$, and the subsequent Schur reductions introduce further inverse matrices. The final physical boundary matrix therefore acquires its charge dependence only after the background sensitivity and all eliminated fields have been included. The next subsection performs the small-radius inner–outer expansion that turns these local coefficients into the finite-radius boundary response.

C.2 Small-radius background expansion

The near-BPS problem contains two radial scales. At fixed outer radius the background approaches the BPS solution, while the region $a = O(a_*)$ retains a nontrivial limiting geometry. I separate these regions by inner–outer matching.

In four dimensions define

$$\delta \equiv a_*^2 = \sqrt{\frac{E}{12}}, \qquad E = 12\delta^2. \tag{C.36}$$

The metric equation therefore departs from its BPS form at $O(\delta^2)$ at fixed nonzero outer radius.

I use the local multi-axion truncation

$$\mathrm{d}\ell^2_{\text{dilaton/saxion}} = \mathrm{d}\sigma^2 + G_{uv}(s)\mathrm{d}s^u\mathrm{d}s^v, \qquad \mathcal{G}^{ij}_\chi(\sigma, s) = \mathrm{e}^{2\beta\sigma}H^{ij}(s), \tag{C.37}$$

for which

$$U_{\boldsymbol{\nu}}(\sigma, s) = \mathrm{e}^{2\beta\sigma}V_{\boldsymbol{\nu}}(s), \qquad V_{\boldsymbol{\nu}}(s) = \nu_i H^{ij}(s)\nu_j. \tag{C.38}$$

Choose a transverse stationary trajectory $s^u = \bar{s}^u_{\boldsymbol{\nu}}$ satisfying

$$\nabla_u V_{\boldsymbol{\nu}}(\bar{s}_{\boldsymbol{\nu}}) = 0. \tag{C.39}$$

At the minimal three-sphere define

$$u_* = \frac{\mathrm{e}^{2\beta\sigma_*}V_{\boldsymbol{\nu}}(\bar{s}_{\boldsymbol{\nu}})}{E} \geq 1. \tag{C.40}$$

Equation (C.7) gives $p_\sigma^2 = E(u_* - 1)$ at the minimal sphere. Thus $u_* > 1$ is precisely the branch on which σ remains a valid clock there. At $u_* = 1$, the scalar momentum vanishes and the first-order constrained system of the preceding subsection supplies the regular description.

To resolve the inner region, set

$$a = a_*\rho(t), \qquad \tau = a_* t, \qquad \psi(t) = \sigma(t) - \sigma_*, \tag{C.41}$$

and define the normalized charge potential

$$\widehat{U}_{\boldsymbol{\nu}}(\psi, s) = \mathrm{e}^{2\beta\psi}\frac{V_{\boldsymbol{\nu}}(s)}{V_{\boldsymbol{\nu}}(\bar{s}_{\boldsymbol{\nu}})}. \tag{C.42}$$

Since $U_{\boldsymbol{\nu}} = 12\delta^2 u_* \widehat{U}_{\boldsymbol{\nu}}$, the two first integrals become

$$\dot{\rho}^{\,2} = 1 - \rho^{-4}, \qquad \rho^6 \dot{\psi}^{\,2} = 12\left(u_* \widehat{U}_{\boldsymbol{\nu}} - 1\right), \tag{C.43}$$

where a dot now denotes $\mathrm{d}/\mathrm{d}t$. At $\rho = 1$,

$$\dot{\psi}_*^{\,2} = 12(u_* - 1). \tag{C.44}$$

The inner equations contain no explicit power of a_*. All small-radius scaling enters through the overall action normalization and through matching to the outer solution.

A signed coordinate makes the complete two-sided geometry elementary:

$$\mathrm{d}y = \frac{2\delta}{a^3}\mathrm{d}\tau, \qquad a^2 = \delta \sec y, \qquad -\frac{\pi}{2} < y < \frac{\pi}{2}, \qquad k = \sqrt{3}\,\beta, \qquad \theta_\beta = \frac{\pi k}{2}. \tag{C.45}$$

The right exterior has $y > 0$ and the left exterior has $y < 0$. The metric becomes

$$\mathrm{d}s^2 = \delta\left[\frac{\mathrm{d}y^2}{4\cos^3 y} + \frac{\mathrm{d}\Omega_3^2}{\cos y}\right]. \tag{C.46}$$

For $\delta > 0$ and $|y| < \pi/2$, every metric eigenvalue is positive and real, so

$$\sum_{\mu=1}^{4} |\mathrm{Arg}\,\lambda_\mu| = 0 < \pi. \tag{C.47}$$

The real finite-radius branch therefore lies strictly inside the four-dimensional Kontsevich–Segal–Witten allowable domain. The logarithm encountered later arises from fluctuation matching.

On the right half,

$$y = \arccos(\rho^{-2}), \tag{C.48}$$

and the sign reverses on the left half. The exact stationary matter profile is

$$H \equiv \mathrm{e}^{-\beta\sigma} = \frac{\mathfrak{c}_{\boldsymbol{\nu}}}{\delta}\sin w, \qquad w = \alpha_* - ky, \qquad \theta_\beta < \alpha_* < \pi - \theta_\beta, \qquad \mathfrak{c}_{\boldsymbol{\nu}} = \sqrt{\frac{V_{\boldsymbol{\nu}}(\bar{s}_{\boldsymbol{\nu}})}{12}}. \tag{C.49}$$

Direct differentiation gives

$$a^3\sigma' = \sqrt{12}\,\delta\cot w, \qquad u_* = \csc^2\alpha_*, \qquad a^3\mathcal{G}^{\chi}_{ij}\chi^{j\prime} = -\nu_i. \tag{C.50}$$

The two radial halves meet smoothly at $y = 0$. Their outward canonical momenta carry opposite orientations at the matching surface.

I now impose the saddle family used throughout the paper. Fix the right asymptotic value

$$h \equiv \mathrm{e}^{-\beta\sigma_R} > 0. \tag{C.51}$$

At the right end $y \to \pi/2$, Eq. (C.49) gives

$$\epsilon = \arcsin\frac{\delta h}{\mathfrak{c}_{\boldsymbol{\nu}}}, \qquad \alpha_* = \theta_\beta + \epsilon, \qquad \vartheta = \pi k, \qquad w_R = \epsilon, \qquad w_L = \vartheta + \epsilon. \tag{C.52}$$

I take the small-radius branch $0 < \epsilon < \pi - \vartheta$. The left asymptotic value is then

$$H_L = \frac{\mathfrak{c}_{\boldsymbol{\nu}}}{\delta}\sin(\vartheta + \epsilon) = \frac{\mathfrak{c}_{\boldsymbol{\nu}}\sin\vartheta}{\delta} + h\cos\vartheta + O(\delta). \tag{C.53}$$

Thus fixing the right data and varying δ moves the left asymptotic dilaton/saxion value, exactly as prescribed in Appendix A.

Conversely, fixing both finite asymptotic values determines the minimal radius. Using $H_R = \mathfrak{c}_{\boldsymbol{\nu}} \sin\epsilon/\delta$ and the sum and difference of H_L and H_R gives

$$\delta = \frac{2\mathfrak{c}_{\boldsymbol{\nu}}}{\sqrt{\left[(H_L + H_R)/\cos\theta_\beta\right]^2 + \left[(H_L - H_R)/\sin\theta_\beta\right]^2}}. \tag{C.54}$$

The two-ended boundary-value problem therefore fixes δ once both asymptotic scalar values and the charge sector are specified.

For

$$0 < \beta < \beta_c = \frac{1}{\sqrt{3}}, \tag{C.55}$$

one has $0 < \theta_\beta < \pi/2$. Along the fixed-right-data family,

$$\alpha_* - \theta_\beta = O(\delta), \qquad u_*(\delta) \longrightarrow u_*^{(0)} \equiv \csc^2\theta_\beta > 1. \tag{C.56}$$

Hence p_σ remains nonzero at the minimal sphere throughout the near-BPS branch used below.

The outer expansion follows directly from the same exact solution. On the right exterior, define

$$u = \arcsin\frac{\delta}{a^2}. \tag{C.57}$$

Since $y = \pi/2 - u$, Eq. (C.49) becomes

$$\mathrm{e}^{-\beta\sigma(a)} = \frac{\sqrt{V_{\boldsymbol{\nu}}(\bar{s}_{\boldsymbol{\nu}})}}{\sqrt{12}\,\delta} \sin\Big(\alpha_* - \theta_\beta + \sqrt{3}\,\beta u\Big). \tag{C.58}$$

Both

$$\alpha_* - \theta_\beta = \arcsin\frac{\delta h}{\mathfrak{c}_{\boldsymbol{\nu}}} \tag{C.59}$$

and $u = \arcsin(\delta/a^2)$ are odd functions of δ. Their sine divided by δ therefore has an expansion in even powers of δ. At fixed $a > 0$,

$$\mathrm{e}^{-\beta\sigma(a)} = \mathrm{e}^{-\beta\sigma_\infty} + \frac{\beta\sqrt{V_{\boldsymbol{\nu}}(\bar{s}_{\boldsymbol{\nu}})}}{2a^2} + O(\delta^2), \qquad \mathrm{e}^{-\beta\sigma_\infty} = h. \tag{C.60}$$

The first two terms are the BPS profile. Hence

$$\sigma(a;\delta) = \sigma_{\mathrm{BPS}}(a) + O(\delta^2) \tag{C.61}$$

at every fixed nonzero outer radius. The $O(\delta)$ effect found below therefore originates in the inner region and in the motion of the left asymptotic endpoint, rather than from an $O(\delta)$ deformation of the fixed-radius outer background.

The same distinction appears in the classical action. Set

$$\mathcal{A} \equiv \frac{\mathcal{V}_3}{2\kappa_4^2}. \tag{C.62}$$

After using the field equations, the two-sided bulk density is

$$\frac{\mathrm{d}I_R}{\mathcal{A}} = 6\delta\left(\csc^2 w - \sec^2 y\right)\mathrm{d}y. \tag{C.63}$$

The matching-surface contributions from the two halves cancel. The flat outer reference terms cancel the integrated $-\sec^2 y$ contribution. The renormalized action is therefore

$$\begin{aligned}\frac{S_{\rm full}^{\rm ren}}{\mathcal{A}} &= \frac{6\delta}{k}\left[\cot\epsilon - \cot(\vartheta+\epsilon)\right] \\ &= \frac{6\mathfrak{c}_{\boldsymbol{\nu}}}{kh} - \frac{6}{k}\cot\vartheta\,\delta + \frac{6h}{k\mathfrak{c}_{\boldsymbol{\nu}}}\left(\csc^2\vartheta - \frac{1}{2}\right)\delta^2 + O(\delta^3).\end{aligned} \tag{C.64}$$

The first term is the finite endpoint action of this truncation. The linear term realizes the right derivative introduced in Appendix A.

The boundary first variation reproduces its coefficient directly. The outward left scalar momentum, with the common normalization $\mathcal{A}$ removed, is

$$p_{\sigma,L}^{\rm out} = -\sqrt{12}\,\delta\cot(\vartheta+\epsilon), \tag{C.65}$$

while Eq. (C.53) gives

$$\frac{\mathrm{d}\sigma_L}{\mathrm{d}\delta} = \frac{1}{\beta\delta} + O(1). \tag{C.66}$$

The right asymptotic value is fixed, and the two matching-surface variations cancel. Consequently

$$\frac{1}{\mathcal{A}}\frac{\mathrm{d}S_{\rm full}^{\rm ren}}{\mathrm{d}\delta} = p_{\sigma,L}^{\rm out}\frac{\mathrm{d}\sigma_L}{\mathrm{d}\delta} \longrightarrow -\frac{6}{k}\cot\vartheta. \tag{C.67}$$

This agrees with the linear term in Eq. (C.64). The $O(\delta)$ action shift is therefore boundary work along the fixed-right-data saddle family, while the local outer background begins at $O(\delta^2)$.

I next extract the scaling of the physical transverse fluctuations. Let q^u be covariant fluctuations about $s^u = \bar{s}^u_{\boldsymbol{\nu}}$. Because the background has $s^{u\prime} = 0$ and $\nabla_u U_{\boldsymbol{\nu}} = 0$, the transverse sector decouples at quadratic order from the lapse, scale factor, and longitudinal fluctuation of σ. In the inner variables its quadratic action is

$$\begin{aligned}I_\perp^{(2)} = \frac{\mathcal{V}_3\delta}{4\kappa_4^2}\int \mathrm{d}t\,\left[\rho^3 G_{uv} D_t q^u D_t q^v + q^u \widehat{\mathbb{V}}_{uv}(t;\widehat{\boldsymbol{\nu}})q^v\right] \\ + \frac{\mathcal{V}_3\delta}{4\kappa_4^2} q^u_\Sigma \widehat{\mathcal{B}}_{uv,\Sigma} q^v_\Sigma + O(\delta^2),\end{aligned} \tag{C.68}$$

where

$$\widehat{\mathbb{V}}_{uv} = 6u_*\rho^{-3}\mathrm{e}^{2\beta\psi}\mathfrak{M}_{uv}(\widehat{\boldsymbol{\nu}}), \tag{C.69}$$

and

$$\mathfrak{M}_{uv}(\widehat{\boldsymbol{\nu}}) = \frac{\nu_i\nabla_u\nabla_v H^{ij}(\bar{s}_{\boldsymbol{\nu}})\nu_j}{\nu_i H^{ij}(\bar{s}_{\boldsymbol{\nu}})\nu_j}. \tag{C.70}$$

Here $\widehat{\boldsymbol{\nu}} = \boldsymbol{\nu}/|\boldsymbol{\nu}|$ records the charge ratios on a fixed active support. Uniform rescaling cancels from $\mathfrak{M}_{uv}$. The overall inner action is proportional to

$$\delta = a_*^2. \tag{C.71}$$

This is the origin of the linear finite-radius scale that survives after matching to the asymptotic boundary.

The same counting applies to every fixed scalar harmonic. Let

$$-\nabla^2_{S^3} Y_{\ell m} = \ell(\ell+2)Y_{\ell m}, \tag{C.72}$$

and suppose the radial potential has a finite inner limit after the rescaling

$$\widehat{\mathcal{V}}_\ell(t) \equiv a_*^2\mathcal{V}_\ell(a_* t). \tag{C.73}$$

Then

$$I^{(2)}_{\ell,\Sigma} = \frac{\mathcal{V}_3\delta}{4\kappa_4^2}\int \mathrm{d}t\,\Big[\rho^3(D_tq_\ell)^T G D_tq_\ell + \rho\,\ell(\ell+2)q_\ell^T G q_\ell + \rho^3 q_\ell^T\widehat{\mathcal{V}}_\ell q_\ell\Big] + O(\delta^2). \tag{C.74}$$

Thus every fixed-ℓ inner quadratic block carries the same overall factor δ. The subsequent outer propagation determines whether this local scale appears as an $O(\delta)$ diagonal Hessian, a higher-order mixed Hessian, or an inverse response enhanced by an endpoint soft mode. Harmonics with $\ell = O(a_*^{-1})$ define a separate double-scaling regime. The calculation below keeps ℓ fixed and proceeds to the exact product-model boundary map.

C.3 Product axion–dilaton/saxion model and boundary covariance

I now solve the homogeneous transverse problem exactly. The product target makes the normalized transverse Hessian universal, while the exact finite-radius solution propagates this local structure to the two physical asymptotic boundaries. This calculation determines the boundary Hessian K, its soft eigenvalue, and the cross-boundary covariance used in the main text.

The model follows from the fixed-charge Legendre transform of the $[SL(2,\mathbb{R})/SO(1,1)]^p$ seed sectors of symmetric-space axion wormholes [6]. Their effective coupling obeys

$$b_{\rm eff}^{-2} = \sum_i b_i^{-2}. \tag{C.75}$$

With $b_i = 2\beta_i$, this gives $b_{\rm eff} = 2\beta$, where β is defined below. The Euclidean axion kinetic terms carry the negative sign before the charge Legendre transform. Fixing the axion momenta converts them into the positive charge potential of the Routhian.

Restrict to the active support of $\boldsymbol{\nu}$ and label its p components by $i = 1,\dots,p$. Take canonically normalized dilaton/saxions ϕ_i with

$$\mathrm{d}\ell^2_{\rm dilaton/saxion} = \sum_{i=1}^p \mathrm{d}\phi_i^2, \qquad \mathcal{G}^\chi_{ij} = \delta_{ij}\mathrm{e}^{-2\beta_i\phi_i}, \qquad \beta_i > 0. \tag{C.76}$$

The inverse axion metric and fixed-charge potential are

$$\mathcal{G}_\chi^{ij} = \delta^{ij}\mathrm{e}^{2\beta_i\phi_i}, \qquad U_{\boldsymbol{\nu}} = \sum_i \nu_i^2\mathrm{e}^{2\beta_i\phi_i}. \tag{C.77}$$

Define

$$\frac{1}{\beta^2} = \sum_i \frac{1}{\beta_i^2}, \qquad n_i = \frac{\beta}{\beta_i}, \qquad \sum_i n_i^2 = 1. \tag{C.78}$$

Choose an orthonormal basis E_{iu}, $u = 1,\dots,p-1$, for the subspace perpendicular to n_i:

$$\sum_i E_{iu}E_{iv} = \delta_{uv}, \qquad \sum_i n_i E_{iu} = 0. \tag{C.79}$$

The orthogonal rotation

$$\phi_i = n_i\sigma + E_{iu}s^u \tag{C.80}$$

separates the scaling direction from the relative dilaton/saxion directions. Equation (C.77) becomes

$$U_{\boldsymbol{\nu}} = \mathrm{e}^{2\beta\sigma}V_{\boldsymbol{\nu}}(s), \qquad V_{\boldsymbol{\nu}}(s) = \sum_i X_i(s), \qquad X_i(s) = \nu_i^2\exp(2\beta_i E_{iu}s^u)\,. \tag{C.81}$$

Universal transverse Hessian. At an interior stationary point of Eq. (C.81), the normalized transverse Hessian defined in Eq. (C.70) is

$$\mathfrak{M}_{uv} = 4\beta^2 \delta_{uv}. \tag{C.82}$$

Thus every transverse direction in the active product sector has the same positive charge-induced quadratic coefficient.

To see this, observe that stationarity gives

$$0 = \frac{1}{2}\partial_u V_{\boldsymbol{\nu}} = \sum_i \beta_i E_{iu} X_i. \tag{C.83}$$

The $(p-1)\times p$ matrix with entries $\beta_i E_{iu}$ has rank $p-1$. Its kernel is therefore one dimensional. The positive vector with components β_i^{-2} belongs to this kernel because

$$\sum_i \beta_i E_{iu} \frac{1}{\beta_i^2} = \sum_i \frac{E_{iu}}{\beta_i} = \frac{1}{\beta} \sum_i n_i E_{iu} = 0. \tag{C.84}$$

Since every X_i is positive on the active support, Eq. (C.83) fixes

$$X_i = \frac{c}{\beta_i^2}, \qquad c > 0. \tag{C.85}$$

It follows that

$$\partial_u \partial_v V_{\boldsymbol{\nu}} = 4 \sum_i \beta_i^2 E_{iu} E_{iv} X_i = 4c\, \delta_{uv}, \tag{C.86}$$

$$V_{\boldsymbol{\nu}} = c \sum_i \frac{1}{\beta_i^2} = \frac{c}{\beta^2}. \tag{C.87}$$

Their ratio gives Eq. (C.82).

Henceforth $V_{\boldsymbol{\nu}}$ denotes $V_{\boldsymbol{\nu}}(\bar{s}_{\boldsymbol{\nu}})$. The BPS profile obtained from Eq. (C.60) is

$$\mathrm{e}^{-\beta\sigma_{\mathrm{BPS}}(a)} = \mathrm{e}^{-\beta\sigma_\infty} + \frac{\beta\sqrt{V_{\boldsymbol{\nu}}}}{2a^2}. \tag{C.88}$$

Introduce the classical inverse-area scale

$$\varpi_{\boldsymbol{\nu}} = \frac{2\mathrm{e}^{-\beta\sigma_\infty}}{\beta\sqrt{V_{\boldsymbol{\nu}}}}. \tag{C.89}$$

Then

$$U_{\boldsymbol{\nu}}^{\mathrm{BPS}}(a) = \frac{4a^4}{\beta^2} \left(1 + \varpi_{\boldsymbol{\nu}} a^2\right)^{-2}. \tag{C.90}$$

For an orthonormal homogeneous transverse mode, the quadratic field equation on the outward BPS branch $a' = 1$ is

$$a^2 q'' + 3aq' - \frac{2\mathfrak{m}_\perp}{\beta^2} \left(1 + \varpi_{\boldsymbol{\nu}} a^2\right)^{-2} q = 0, \qquad \mathfrak{m}_\perp = 4\beta^2. \tag{C.91}$$

Thus

$$a^2 q'' + 3aq' - 8 \left(1 + \varpi_{\boldsymbol{\nu}} a^2\right)^{-2} q = 0. \tag{C.92}$$

A fundamental pair is

$$q_+(a) = \frac{a^2}{1 + \varpi_{\boldsymbol{\nu}} a^2}, \qquad q_-(a) = a^{-4} \left(1 + \varpi_{\boldsymbol{\nu}} a^2\right)^2. \tag{C.93}$$

Near the BPS endpoint these branches behave as a^2 and a^{-4}. The homogeneous charged outer equation therefore contains no Frobenius logarithm.

I now solve the finite-radius transverse problem exactly. Using Eq. (C.82) on the matter profile of Eq. (C.49), the quadratic action becomes

$$I_q^{(2)} = \mathcal{A}\delta \int_{-\pi/2}^{\pi/2} \left[q_y^2 + 2k^2 \csc^2 w\, q^2\right] \mathrm{d}y, \qquad \frac{\mathrm{d}^2 q}{\mathrm{d}w^2} = 2\csc^2 w\, q. \tag{C.94}$$

The coefficient $\mathcal{A}$ is the positive normalization fixed in the preceding subsection. A convenient fundamental pair is

$$u_1(w) = \cot w, \qquad u_2(w) = 1 - w\cot w, \qquad u_1 u_2' - u_1' u_2 = 1. \tag{C.95}$$

Near the right BPS end,

$$u_1(w) = w^{-1} + O(w), \qquad u_2(w) = \frac{w^2}{3} + O(w^4). \tag{C.96}$$

In the limiting right inner profile, set $\epsilon = 0$ before taking the overlap limit. Then

$$w = k \arcsin \frac{\delta}{a^2} = \frac{k\delta}{a^2} + O\left(\frac{\delta^3}{a^6}\right). \tag{C.97}$$

For $q = C_1 u_1 + C_2 u_2$, comparison with the two BPS branches gives

$$\frac{B_{\mathrm{out}}}{A_{\mathrm{out}}} = \frac{k^3}{3}\frac{C_2}{C_1}\delta^3 + O(\delta^4). \tag{C.98}$$

This cubic ratio is a local overlap statement. The physical two-boundary Hessian also depends on the global Dirichlet data and on the displacement $\epsilon(\delta)$ of the background.

Let q_L and q_R be the two asymptotic boundary values. The on-shell Dirichlet action defines

$$I_{q,\mathrm{on}}^{(2)} = \frac{\mathcal{A}}{2}(q_L, q_R) K \begin{pmatrix} q_L \\ q_R \end{pmatrix}, \qquad \Delta = u_{1R}u_{2L} - u_{2R}u_{1L}, \tag{C.99}$$

where

$$w_R = \epsilon, \qquad w_L = \vartheta + \epsilon. \tag{C.100}$$

The physical outer-boundary Hessian is

$$\mathcal{K}_{\boldsymbol{\nu},B}^{\partial} = \mathcal{A}K. \tag{C.101}$$

It is distinct from the matching-surface Hessian $\mathcal{K}_{\boldsymbol{\nu},B}^{\Sigma}$ of Appendix B.

Primes below denote derivatives with respect to w. With the common factor $\mathcal{A}$ removed, the outward canonical momenta are $2k\delta q_w(w_L)$ and $-2k\delta q_w(w_R)$. The exact Dirichlet-to-Neumann matrix is therefore

$$\begin{aligned} K_{LL} &= \frac{2k\delta}{\Delta}\left[-u_{2R}u_{1L}' + u_{1R}u_{2L}'\right], \\ K_{RR} &= -\frac{2k\delta}{\Delta}\left[u_{1R}'u_{2L} - u_{1L}u_{2R}'\right], \\ K_{LR} &= K_{RL} = -\frac{2k\delta}{\Delta}. \end{aligned} \tag{C.102}$$

For every permitted $\delta > 0$, $0 < w_R < w_L < \pi$ and the integrand in Eq. (C.94) is strictly positive. Hence K is positive definite. Equivalently, a zero eigenvector of K would give

a nonzero solution with vanishing outward momenta at both ends; integration of the field equation against that solution forces it to vanish.

The exact matrix now gives the near-BPS boundary scaling. Define

$$v_0 = 1 - \vartheta \cot \vartheta, \qquad v_1 = -\cot \vartheta + \vartheta \csc^2 \vartheta. \tag{C.103}$$

For the subcritical branch, $0 < \vartheta < \pi$, and $v_0, v_1 > 0$. Expanding Eq. (C.102) at fixed right asymptotic data gives

$$\begin{aligned} K_{LL} &= a_1 \delta + O(\delta^2), & a_1 &= 2k \frac{v_1}{v_0} > 0, \\ K_{RR} &= r_0 + \frac{kh}{\mathfrak{c}_{\boldsymbol{\nu}}} \delta^2 + O(\delta^3), & r_0 &= \frac{2k\mathfrak{c}_{\boldsymbol{\nu}}}{h} > 0, \\ K_{LR} &= b_2 \delta^2 + O(\delta^3), & b_2 &= -\frac{2kh}{\mathfrak{c}_{\boldsymbol{\nu}} v_0} < 0. \end{aligned} \tag{C.104}$$

Consequently

$$\det K = a_1 r_0 \, \delta + O(\delta^2). \tag{C.105}$$

The finite-radius variation of the on-shell quadratic action begins as

$$I^{(2)}_{q,\mathrm{on}}(\delta) - I^{(2)}_{q,\mathrm{on}}(0) = \frac{\mathcal{A} a_1}{2} \delta q_L^2 + O(\delta^2 |q|^2). \tag{C.106}$$

The two eigenvalues of the physical Hessian are

$$\mathcal{A} a_1 \delta + O(\delta^2), \qquad \mathcal{A} r_0 + O(\delta^2). \tag{C.107}$$

Thus one boundary combination becomes soft linearly in δ, while the orthogonal combination retains a finite restoring term.

The covariance follows by integrating the two boundary values with the fixed Lebesgue measure and linear sources. Since

$$G = \mathcal{A}^{-1} K^{-1}, \tag{C.108}$$

the exact cross-boundary response is

$$\begin{aligned} G_{LR}(\delta) &= \frac{1}{\mathcal{A}} (K^{-1})_{LR} \\ &= \frac{\delta h^2}{2\mathcal{A} k \mathfrak{c}_{\boldsymbol{\nu}}^2} \frac{\sin^2(\vartheta + \epsilon)}{\vartheta - \sin \vartheta \cos(\vartheta + 2\epsilon)} \\ &= g_{1,\boldsymbol{\nu}} \delta + O(\delta^2), \end{aligned} \tag{C.109}$$

$$g_{1,\boldsymbol{\nu}} = \frac{h^2 \sin^2 \vartheta}{2\mathcal{A} k \mathfrak{c}_{\boldsymbol{\nu}}^2 \left[\vartheta - \sin \vartheta \cos \vartheta\right]} > 0. \tag{C.110}$$

The same inverse may be written as

$$(K^{-1})_{LR} = -\frac{1}{2k\delta \left(u'_{1R} u'_{2L} - u'_{1L} u'_{2R}\right)}. \tag{C.111}$$

The denominator in Eq. (C.110) is positive because

$$\vartheta - \sin \vartheta \cos \vartheta = 2 \int_0^{\vartheta} \sin^2 t \, \mathrm{d}t > 0. \tag{C.112}$$

The scaling is now transparent: $K_{LR} = O(\delta^2)$, whereas $\det K = O(\delta)$. The inverse therefore converts the quadratic off-diagonal Hessian entry into the linear covariance $G_{LR} = O(\delta)$.

The exact inverse also fixes the first subleading term. Define

$$v_2 = 2v_0 \csc^2\vartheta, \qquad G_{LR,\boldsymbol{\nu}} = g_{1,\boldsymbol{\nu}}\delta + g_{2,\boldsymbol{\nu}}\delta^2 + O(\delta^3), \qquad \frac{g_{2,\boldsymbol{\nu}}}{g_{1,\boldsymbol{\nu}}} = -\frac{h}{\mathfrak{c}_{\boldsymbol{\nu}}}\frac{v_2}{v_1}. \tag{C.113}$$

Indeed, the logarithmic derivative of the ϵ-dependent factor in Eq. (C.109) at $\epsilon = 0$ is

$$2\cot\vartheta - \frac{2\sin^2\vartheta}{\vartheta - \sin\vartheta\cos\vartheta} = -\frac{v_2}{v_1}. \tag{C.114}$$

Since

$$\epsilon'(0) = \frac{h}{\mathfrak{c}_{\boldsymbol{\nu}}}, \tag{C.115}$$

Eq. (C.113) follows. For $0 < \vartheta < \pi$, v_0, v_1, v_2 are positive, so

$$g_{2,\boldsymbol{\nu}} < 0. \tag{C.116}$$

The normalized cross-boundary response therefore bends downward at its first sub-leading order.

The unnormalized source coefficient requires the complete fixed-saddle weight. Let

$$Z_{\boldsymbol{\nu}}[0;\delta] \longrightarrow Z_{\boldsymbol{\nu},0} \tag{C.117}$$

as $\delta \to 0^+$ after exact modes, prescribed insertions, fermions, ghosts, boundary normalization, and the remaining fluctuation factors have been included. Then Eq. (C.109) and the centered-source identity of Appendix A give

$$C^{LR}_{\boldsymbol{\nu}}(0) = 0, \qquad \partial_\delta C^{LR}_{\boldsymbol{\nu}}\big|_{0^+} = Z_{\boldsymbol{\nu},0}\, g_{1,\boldsymbol{\nu}}. \tag{C.118}$$

The isolated two-boundary bosonic Gaussian does not possess this finite endpoint weight: its soft eigenvalue contributes a factor $\delta^{-1/2}$. The finite quantity $Z_{\boldsymbol{\nu},0}$ is therefore a property of the complete fixed-charge measure. If the prescribed insertions leave an exact fermion zero mode unsaturated, the corresponding BPS sector weight vanishes and so does the slope in Eq. (C.118).

All $p-1$ orthonormal transverse directions obey the same radial equation and carry the same coefficient with the common boundary normalization used here. In the original ϕ_i coordinates their projector is

$$EE^T = \boldsymbol{I} - nn^T. \tag{C.119}$$

Finally, the result depends on the boundary state exactly as described in the main text. Adding

$$\frac{\mathcal{A}}{2}\left(\mu_L q_L^2 + \mu_R q_R^2\right), \qquad \mu_L, \mu_R \geq 0, \tag{C.120}$$

replaces

$$K \longrightarrow K + \mathrm{diag}(\mu_L, \mu_R). \tag{C.121}$$

The cross covariance becomes

$$G^{(\mu)}_{LR} = \begin{cases} -\dfrac{b_2\delta}{\mathcal{A}a_1(r_0+\mu_R)} + O(\delta^2), & \mu_L = 0, \\ -\dfrac{b_2\delta^2}{\mathcal{A}\mu_L(r_0+\mu_R)} + O(\delta^3), & \mu_L > 0. \end{cases} \tag{C.122}$$

A positive quadratic term in the soft left-boundary direction lifts its $O(\delta)$ eigenvalue to $O(1)$ and changes the cross response from $O(\delta)$ to $O(\delta^2)$. I use $\mu_L = \mu_R = 0$ in the remainder of the calculation. For this boundary state the bare two-variable Gaussian carries the factor $\delta^{-1/2}$, while the physical finite-BPS matching concerns the complete fixed-charge weight. The finite-radius transverse quadratic form itself remains strictly positive for every $\delta > 0$ on the branch considered here.

C.4 Cubic and quartic corrections

The linearly soft boundary eigenvalue amplifies interaction corrections. I therefore compute the cubic and quartic vertices of the effective soft boundary action and use them below to determine the range of validity of the Gaussian approximation.

At the stationary product point define

$$\omega_i = \frac{\beta^2}{\beta_i^2}, \qquad t_i = 2\beta_i E_{iu} q^u. \tag{C.123}$$

Equations (C.78), (C.81), and (C.85) give

$$\frac{X_i}{V} = \omega_i, \qquad \sum_i \omega_i = 1, \qquad \omega_i = \frac{\beta^2}{\beta_i^2}. \tag{C.124}$$

The exact transverse charge potential on the fixed background is therefore

$$\frac{V(\bar{s}+q)}{V(\bar{s})} = \sum_i \omega_i \mathrm{e}^{t_i}, \qquad \sum_i \omega_i t_i = 0, \qquad \sum_i \omega_i t_i^2 = 4\beta^2 |q|^2. \tag{C.125}$$

The transverse kinetic metric is flat in these coordinates. After subtracting the background action,

$$\frac{\Delta I_\perp}{\mathcal{A}\delta} = \int \mathrm{d}y \left[|q_y|^2 + 3\csc^2 w \left(\sum_i \omega_i \mathrm{e}^{t_i} - 1 \right) \right]. \tag{C.126}$$

The quadratic term reproduces Eq. (C.94). Expanding the exponential gives the direct cubic and quartic terms

$$\frac{I_\perp^{(3)} + I_{\perp,\mathrm{dir}}^{(4)}}{\mathcal{A}\delta} = \int \mathrm{d}y \, \csc^2 w \left[4\beta^2 \sum_i \beta_i (E_i \cdot q)^3 + 2\beta^2 \sum_i \beta_i^2 (E_i \cdot q)^4 \right]. \tag{C.127}$$

Here $E_i \cdot q \equiv E_{iu} q^u$. Relaxation of the remaining physical fields first contributes at quartic order.

Choose a unit transverse direction e and denote the left soft boundary amplitude by z. At the BPS endpoint the stationary value of the regular right-boundary combination is zero. The leading soft profile is therefore

$$q(w) = ze\, f(w), \qquad f(w) = \frac{1 - w\cot w}{v_0}, \qquad 0 \le w \le \vartheta, \qquad 0 \le f(w) \le 1. \tag{C.128}$$

The last inequality follows from monotonicity of $1 - w\cot w$ on $0 < w < \pi$. Define

$$J_n = \int_0^\vartheta \csc^2 w \, f(w)^n \mathrm{d}w, \qquad T_n(e) = \sum_i \beta_i^{n-2} (E_i \cdot e)^n. \tag{C.129}$$

Since $f(w) = O(w^2)$ at the right endpoint, the integrand defining J_n is $O(w^{2n-2})$. In particular, J_3 and J_4 are finite.

Evaluating Eq. (C.127) on the stationary linear profile gives

$$\frac{I_{\mathrm{soft}}}{\mathcal{A}\delta} = \frac{a_1 z^2}{2} + \frac{\lambda_3 z^3}{6} + \frac{\lambda_{4,\mathrm{dir}} z^4}{24} + \cdots, \qquad \lambda_3 = 8kT_3J_3, \qquad \lambda_{4,\mathrm{dir}} = 16kT_4J_4. \tag{C.130}$$

The $O(z^2)$ correction to the stationary profile contributes first at $O(z^4)$, so the linear profile determines λ_3 exactly. The quartic coefficient also receives exchange contributions from the regular complementary fields.

Collect those regular coordinates in u and write their quadratic coupling to the soft mode as

$$\frac{1}{2}u^T\mathcal{H}_c u + \frac{z^2}{2}\mathcal{J}^T u. \tag{C.131}$$

Stationarity gives

$$u = -\frac{z^2}{2}\mathcal{H}_c^{-1}\mathcal{J},$$

and hence

$$\lambda_4 = \lambda_{4,\mathrm{dir}} - 3\mathcal{J}^T\mathcal{H}_c^{-1}\mathcal{J}, \qquad |\lambda_4| \le |\lambda_{4,\mathrm{dir}}| + 3\|\mathcal{H}_c^{-1}\|\|\mathcal{J}\|^2. \tag{C.132}$$

Equation (C.132) is the Schur-complement correction to the quartic vertex. For a positive complementary quadratic form it lowers the direct quartic coefficient. For a contour-rotated gravitational coordinate, the coordinate and its source are continued together.

For a one-dimensional contour-rotated gravitational mode,

$$-\frac{1}{2}Hu^2 + \frac{1}{2}\mathcal{J}z^2u \tag{C.133}$$

gives

$$\Delta I_{\mathrm{eff}} = +\frac{\mathcal{J}^2 z^4}{8H} \tag{C.134}$$

after stationary elimination. I use this common contour continuation for the gravitational exchange channels below.

I now evaluate the complementary relaxation explicitly in the homogeneous product model at $d = 3$ and $\Lambda = 0$. A transverse boundary displacement changes the individual scalar first-integral constants. The Hamiltonian constraint then shifts the minimal radius. I fix the charges, the induced outer metrics, and the longitudinal dilaton/saxion boundary data. The left transverse displacement is ze. The effective soft action is obtained after the regular right-boundary combination and the interior fields have relaxed. At the order required for the limiting cubic and quartic vertices, its stationary right transverse value may be set to zero. The two radial halves are joined smoothly, so their oriented matching-surface terms cancel.

Let $\widehat{\delta}$ denote the displaced squared minimal radius and introduce harmonic radial time ξ, increasing from the right end to the left end, through

$$|\mathrm{d}\xi| = \frac{\mathrm{d}\tau}{a^3}.$$

With $X = \log a$, the scalar and gravitational first integrals separate:

$$\dot{\phi}_i^{\,2} - \nu_i^2 \mathrm{e}^{2\beta_i\phi_i} = -r_i^2, \qquad \dot{X}^2 = \mathrm{e}^{4X} - \widehat{\delta}^2, \qquad \sum_i r_i^2 = 12\widehat{\delta}^2. \tag{C.135}$$

Here a dot denotes $\mathrm{d}/\mathrm{d}\xi$. The branch connected continuously to the reference saddle has the exact solution

$$\begin{aligned} a^2 &= \widehat{\delta}\csc(2\widehat{\delta}\xi), & 0 < \xi < \frac{\pi}{2\widehat{\delta}}, \\ \mathrm{e}^{-\beta_i\phi_i} &= \frac{|\nu_i|}{r_i}\sin(\beta_i r_i \xi + \epsilon_i), & r_i = \frac{2k\widehat{\delta}}{\beta_i}\sqrt{b_i}, \qquad \sum_i \omega_i b_i = 1. \end{aligned} \tag{C.136}$$

The final relation is equivalent to the Hamiltonian constraint because $k^2 = 3\beta^2$ and $\omega_i = \beta^2/\beta_i^2$. The metric reflects about the middle of the harmonic interval, while the phases ϵ_i impose the scalar boundary data.

Set

$$x_i = \beta_i(E_i \cdot e), \qquad t = \log \frac{\widehat{\delta}}{\delta}, \qquad \eta = \frac{\delta h}{\mathfrak{c}_{\boldsymbol{\nu}}}.$$

The orthogonality relations imply

$$\sum_i \omega_i x_i = 0, \qquad \sum_i \omega_i x_i^2 = \beta^2.$$

The exact right phases and the left Dirichlet conditions are

$$\epsilon_i = \arcsin\Big(\eta \mathrm{e}^t \sqrt{b_i}\Big), \qquad \frac{\sin(\vartheta\sqrt{b_i} + \epsilon_i)}{\mathrm{e}^t\sqrt{b_i}} = \sin(\vartheta + \epsilon)\mathrm{e}^{-x_i z}, \qquad \epsilon = \arcsin\eta. \tag{C.137}$$

These equations impose the physical boundary data before the small-radius limit is taken. The variation of the throat radius begins at $O(z^2)$. Since the complete inner action carries the prefactor $\mathcal{A}\delta$, eliminating this radius response first changes the effective action at $O(\mathcal{A}\delta z^4)$.

The exact renormalized action at fixed outer data is

$$\frac{S^{\mathrm{ren}}}{\mathcal{A}} = \sum_i \frac{r_i}{\beta_i}\Big[\cot\epsilon_i - \cot(\vartheta\sqrt{b_i} + \epsilon_i)\Big]. \tag{C.138}$$

Flat reference subtraction removes the outer gravitational divergence. The Hamiltonian constraint cancels the remaining constant bulk terms. At $b_i = 1$ and $t = 0$, Eq. (C.138) reduces to the background result Eq. (C.64).

The $\delta \to 0$ boundary map takes a particularly simple form. Define

$$\begin{aligned} &\mathcal{F}(b) = \log\frac{\sin(\vartheta\sqrt{b})}{\sqrt{b}\,\sin\vartheta}, \quad \mathcal{F}(b_i) = t - x_i z, \qquad \sum_i \omega_i b_i = 1, \\ &F_1 = \mathcal{F}'(1) = -\frac{v_0}{2}, \qquad F_2 = \mathcal{F}''(1) = \frac{2 - \vartheta\cot\vartheta - \vartheta^2\csc^2\vartheta}{4}. \end{aligned} \tag{C.139}$$

Since $0 < \vartheta < \pi$, one has $v_0 > 0$ and therefore $F_1 < 0$. The Jacobian of the boundary equations is invertible. The implicit function theorem then gives a unique analytic solution for $b_i(t, z)$ near the reference saddle.

Expanding $\mathcal{F}(b_i) = t - x_i z$ together with $\sum_i \omega_i b_i = 1$ gives

$$\begin{aligned} &t = t_2 z^2 + O(z^3), && t_2 = \frac{\beta^2 F_2}{2F_1^2}, \\ &b_i = 1 - \frac{x_i}{F_1} z + \frac{F_2(\beta^2 - x_i^2)}{2F_1^3} z^2 + O(z^3). \end{aligned} \tag{C.140}$$

Thus the minimal radius responds only at second order in a transverse boundary displacement. This response contributes to the quartic vertex and leaves the quadratic Hessian unchanged.

I next compute the scalar exchange at fixed harmonic interval. The regular scalar complement is governed by

$$L = -\partial_w^2 + 2\csc^2 w$$

on $0 < w < \vartheta$, with the regular w^2 branch at the right endpoint and Dirichlet data at the left endpoint. Set

$$P(w) = 1 - w\cot w, \qquad v(w) = v_0\cot w - \cot\vartheta\, P(w).$$

The Dirichlet Green function is

$$\begin{aligned} G_D(w, s) &= \frac{P(w_<)v(w_>)}{v_0}, \qquad w_< = \min(w, s), \qquad w_> = \max(w, s), \\ \|G_D\|_{L^2\to L^2} &\le \frac{1}{2 + \pi^2/\vartheta^2}. \end{aligned} \tag{C.141}$$

The Wronskian

$$Pv' - P'v = -v_0$$

fixes the derivative jump. Since $L \geq -\partial_w^2 + 2$ on the Dirichlet interval, the Poincaré inequality gives the displayed resolvent bound.

Define

$$j_f(w) = \csc^2 w\, f(w)^2.$$

The second-order source solution is

$$\begin{aligned} \mathfrak{r}(w) &= -2\int_0^\vartheta G_D(w,s) j_f(s)\mathrm{d}s \\ &= \frac{-1 + w^2\csc^2 w - P(w) + 4F_2 P(w)/v_0}{2v_0^2}, \\ \mathcal{I}_f &= \int_0^\vartheta \int_0^\vartheta j_f(w) G_D(w,s) j_f(s)\mathrm{d}w\,\mathrm{d}s \\ &= -\frac{1}{2}\int_0^\vartheta j_f(w)\mathfrak{r}(w)\mathrm{d}w > 0. \end{aligned} \tag{C.142}$$

Direct differentiation gives

$$L\mathfrak{r} = -2j_f, \qquad \mathfrak{r}(0) = \mathfrak{r}(\vartheta) = 0.$$

The apparent singular terms in the explicit expression cancel at $w = 0$. In the product variables, each regular scalar channel has this same fixed-interval Green function. Its second-order displacement is

$$\delta^{(2)}\phi_i = \beta_i (E_i \cdot e)^2 \mathfrak{r}(w) z^2.$$

Substitution into the Schur-complement formula Eq. (C.132) gives

$$\Delta\lambda_{4,\mathrm{scalar}} = -96kT_4\mathcal{I}_f, \qquad \mathcal{J}_{\mathrm{scalar}}^T \mathcal{H}_{\mathrm{scalar}}^{-1} \mathcal{J}_{\mathrm{scalar}} = 32kT_4\mathcal{I}_f.$$

The remaining relaxation is the change of the harmonic interval, equivalently the throat radius. For fixed t solve the scalar boundary equations first, so that $b_i = b_i(t,z)$ is determined by $\mathcal{F}(b_i) = t - x_i z$. Define

$$g(b) = \sqrt{b}\,\cot(\vartheta\sqrt{b}).$$

Up to an additive constant, the leading constrained action is

$$\mathcal{S}(t,z) = -\frac{6}{k}\mathrm{e}^t \sum_i \omega_i g(b_i) + 3\pi\mathrm{e}^t\left(1 - \sum_i \omega_i b_i\right). \tag{C.143}$$

Differentiating along the implicitly determined functions $b_i(t,z)$ gives

$$\partial_t \mathcal{S} = 3\pi\mathrm{e}^t\left(1 - \sum_i \omega_i b_i\right).$$

Thus stationarity in t is exactly the Hamiltonian constraint.

At the reference saddle,

$$H_t \equiv \partial_t^2 \mathcal{S}\big|_0 = -\frac{3\pi}{F_1} = \frac{6\pi}{v_0} > 0, \qquad J_t \equiv \partial_t \partial_z^2 \mathcal{S}\big|_0 = \frac{3\pi\beta^2 F_2}{F_1^3}. \tag{C.144}$$

The scalar variables have already relaxed in these derivatives. Eliminating t therefore gives the quartic correction

$$-\frac{3J_t^2}{H_t} = -\frac{288\pi\beta^4 F_2^2}{v_0^5},$$

and reproduces the radius shift t_2 in Eq. (C.140).

Combining the direct term, scalar exchange, and radius exchange gives the complete quartic coefficient of the homogeneous soft direction:

$$\lambda_4 = 16kT_4J_4 - 96kT_4\mathcal{I}_f - \frac{288\pi\beta^4F_2^2}{v_0^5}, \qquad \mathcal{J}^T\mathcal{H}_c^{-1}\mathcal{J} = 32kT_4\mathcal{I}_f + \frac{96\pi\beta^4F_2^2}{v_0^5}. \tag{C.145}$$

The first exchange term comes from the regular scalar complement. The second comes from the Hamiltonian constraint through the radius response. Both enter at $O(\mathcal{A}\delta z^4)$. Equation (C.145) is the quartic vertex used in the validity analysis below.

The corresponding fields through second order are

$$\begin{aligned}\phi_i(w;z) - \bar{\phi}_i(w) &= z(E_i\cdot e)f(w) \\ &\quad + z^2\left[\beta_i(E_i\cdot e)^2\mathfrak{r}(w) + \frac{t_2}{\beta_i}\big(1-f(w)\big)\right] + O(z^3), \\ \widehat{\delta} &= \delta\left[1 + t_2z^2 + O(z^3)\right].\end{aligned} \tag{C.146}$$

The first term is the soft transverse profile. The $\mathfrak{r}$ term is the regular scalar relaxation. The term proportional to $1-f$ is the longitudinal response induced by the change of radial scale. At the left boundary, $f(\vartheta) = 1$ and $\mathfrak{r}(\vartheta) = 0$, so the prescribed displacement is purely transverse and has no longitudinal component. Equation (C.137) fixes the physical right boundary data before the inner limit is taken; Eq. (C.146) is its expansion at fixed rescaled coordinate. The metric remains reflection symmetric while the scalar profile carries the asymmetric boundary data.

C.5 Range of the quadratic approximation

The interaction vertices of the preceding subsection determine the lower end of the Gaussian regime. I first check them directly against the constrained tree action and then derive uniform bounds for all transverse soft directions.

After solving the boundary equations for b_i and imposing $\sum_i \omega_i b_i = 1$, the renormalized action relative to the undeformed solution is

$$\frac{\Delta S^{\mathrm{ren}}}{\mathcal{A}\delta} = -\frac{6}{k}\left[\mathrm{e}^t\sum_i \omega_i g(b_i) - \cot\vartheta\right] + O(\delta). \tag{C.147}$$

Here $t = t(z)$ and $b_i = b_i(z)$ are the constrained solutions of Eq. (C.139). The second, third, and fourth derivatives of Eq. (C.147) at $z = 0$ reproduce a_1, λ_3, and the complete quartic coefficient in Eq. (C.145). A direct power-series solution of the boundary equations gives the same coefficients for the equal two-factor model and for the unequal couplings $(0.6, 0.7, 0.9)$.[3] Independent inversion of the exact finite-radius boundary matrix reproduces Eq. (C.109).

As a calibration case, take two equal factors,

$$\beta_i = \sqrt{2}\,\beta, \qquad E = \frac{1}{\sqrt{2}}(1,-1)^T. \tag{C.148}$$

[3] I checked the resulting algebraic residuals below 10^{-45} at 65-digit precision.

Interchange of the two factors sends $z \to -z$ and therefore sets $\lambda_3 = 0$. At $k = 1/2$,

$$\begin{aligned} a_1 &= \frac{\pi}{2}, \qquad \lambda_3 = 0, \\ \lambda_4 &= \frac{\pi(\pi^2 - 10)}{48} = -0.00853437199\ldots, \\ \lambda_{4,\mathrm{dir}} &= 0.10409776147\ldots, \\ \Delta\lambda_{4,\mathrm{scalar}} &= -0.02684160432\ldots, \\ \Delta\lambda_{4,\mathrm{length}} &= -0.08579052914\ldots, \\ t_2 &= -\frac{\pi^2 - 8}{96}. \end{aligned} \tag{C.149}$$

The scalar and interval-length exchange terms outweigh the positive direct quartic term and make the net quartic coefficient negative. The quadratic coefficient remains positive. The local soft potential therefore becomes less confining at quartic order in this example.

Set

$$\Lambda_* = \mathcal{A}\delta. \tag{C.150}$$

For one soft coordinate with fixed Lebesgue measure, use the effective tree action

$$\Lambda_* \left(\frac{a_1 z^2}{2} + \frac{\lambda_3 z^3}{6} + \frac{\lambda_4 z^4}{24} \right). \tag{C.151}$$

Expanding around the Gaussian measure gives

$$\begin{aligned} \frac{Z_{\mathrm{soft}}}{Z_{\mathrm{G}}} &= 1 + \frac{1}{\Lambda_*} \left[-\frac{\lambda_4}{8a_1^2} + \frac{5\lambda_3^2}{24a_1^3} \right] + O(\Lambda_*^{-2}), \\ \langle z^2 \rangle_c &= \frac{1}{\Lambda_* a_1} \left[1 + \frac{1}{\Lambda_*} \left(-\frac{\lambda_4}{2a_1^2} + \frac{\lambda_3^2}{a_1^3} \right) + O(\Lambda_*^{-2}) \right]. \end{aligned} \tag{C.152}$$

The cubic vertex shifts the mean already at first subleading order,

$$\langle z \rangle = -\frac{\lambda_3}{2\Lambda_* a_1^2} + O(\Lambda_*^{-2}), \tag{C.153}$$

and Eq. (C.152) uses the connected variance after subtracting this shift. The quartic and cubic corrections remain perturbative when

$$\frac{|\lambda_4|}{\Lambda_* a_1^2} \ll 1, \qquad \frac{\lambda_3^2}{\Lambda_* a_1^3} \ll 1. \tag{C.154}$$

I now keep all $d_\perp = p - 1$ soft transverse directions. The cubic radial coefficient is

$$c_3 = 8kJ_3. \tag{C.155}$$

The quartic coefficient receives the direct contribution and the regular scalar exchange,

$$c_4 = 16kJ_4 - 96k\mathcal{I}_f, \tag{C.156}$$

while the radius response imposed by the Hamiltonian constraint gives

$$c_g = -\frac{288\pi\beta^4 F_2^2}{v_0^5}. \tag{C.157}$$

These coefficients define the cubic and quartic vertex tensors,

$$V_{abc} = c_3 \sum_i \beta_i E_{ia} E_{ib} E_{ic}, \tag{C.158}$$

and

$$W_{abcd} = c_4 \sum_i \beta_i^2 E_{ia} E_{ib} E_{ic} E_{id} + \frac{c_g}{3} \left(\delta_{ab}\delta_{cd} + \delta_{ac}\delta_{bd} + \delta_{ad}\delta_{bc}\right). \tag{C.159}$$

The first term in W_{abcd} contains the direct quartic vertex and the regular scalar exchange. The second term is the isotropic radius response.

The resulting soft boundary action is

$$\frac{I_{\rm soft}}{\mathcal{A}\delta} = \frac{a_1}{2} z_a z_a + \frac{1}{6} V_{abc} z_a z_b z_c + \frac{1}{24} W_{abcd} z_a z_b z_c z_d + \cdots . \tag{C.160}$$

For a unit transverse vector e_a,

$$\lambda_3(e) = V_{abc} e_a e_b e_c, \qquad \lambda_4(e) = W_{abcd} e_a e_b e_c e_d, \tag{C.161}$$

which reproduces the directional cubic and quartic coefficients derived in the preceding subsection.

Set

$$S_\beta = \sum_i \beta_i^2, \qquad N_3 = S_\beta - (3p-2)\beta^2, \qquad R_3 = S_\beta - p^2\beta^2, \qquad R_4 = S_\beta - (2p-1)\beta^2. \tag{C.162}$$

Since

$$\left(\sum_i \beta_i^2\right)\left(\sum_i \beta_i^{-2}\right) \geq p^2, \tag{C.163}$$

one has $S_\beta \geq p^2\beta^2$. Thus N_3, R_3, and R_4 are nonnegative for $p \geq 2$. Using

$$EE^T = \boldsymbol{I} - nn^T \tag{C.164}$$

gives the exact contractions

$$V_{abc}V_{abc} = c_3^2 N_3, \qquad V_{abb}V_{acc} = c_3^2 R_3, \qquad W_{aabb} = c_4 R_4 + \frac{c_g}{3} d_\perp (d_\perp + 2). \tag{C.165}$$

Repeated transverse indices are summed.

Gaussian Wick contraction then gives the first correction to the multidimensional soft partition function,

$$\frac{Z_{\rm soft}}{Z_{\rm G}} = 1 + \frac{1}{\Lambda_*}\left[-\frac{c_4 R_4 + c_g d_\perp(d_\perp+2)/3}{8a_1^2} + \frac{c_3^2 N_3}{12 a_1^3} + \frac{c_3^2 R_3}{8a_1^3}\right] + O(\Lambda_*^{-2}). \tag{C.166}$$

The corresponding connected covariance is

$$\langle z_a z_b \rangle_c = \frac{1}{\Lambda_* a_1}\left[\delta_{ab} + \frac{1}{\Lambda_*}\left(-\frac{W_{abcc}}{2a_1^2} + \frac{V_{acd}V_{bcd} + V_{abc}V_{cdd}}{2a_1^3}\right) + O(\Lambda_*^{-2})\right]. \tag{C.167}$$

For $d_\perp = 1$, Eqs. (C.166) and (C.167) reduce to Eq. (C.152). The connected contraction in Eq. (C.167) includes the subtraction of the cubic mean shift.

Triangle and Cauchy–Schwarz inequalities give sufficient uniform bounds on these corrections. The partition-function correction is bounded by $\mathcal{C}_Z/\Lambda_*$ and the operator norm of the relative covariance correction by $\mathcal{C}_V/\Lambda_*$, with

$$\begin{aligned}\mathcal{C}_Z &= \frac{|c_4|R_4 + |c_g|d_\perp(d_\perp+2)/3}{8a_1^2} + \frac{c_3^2 N_3}{12a_1^3} + \frac{c_3^2 R_3}{8a_1^3},\\ \mathcal{C}_V &= \frac{|c_4|R_4 + |c_g|(d_\perp+2)/3}{2a_1^2} + \frac{c_3^2\left(N_3 + \sqrt{N_3 R_3}\right)}{2a_1^3}.\end{aligned} \tag{C.168}$$

A separate bound controls the field range over which the exponential potential may be truncated. Define

$$b = \max_i \beta_i \|E_i\|, \qquad t_{\max} = 2b|q|. \tag{C.169}$$

Then $|t_i| \le t_{\max}$, and Taylor's integral remainder gives

$$\left|\sum_i \omega_i \left(\mathrm{e}^{t_i} - 1 - t_i - \frac{1}{2}t_i^2\right)\right| \le \frac{t_{\max}\mathrm{e}^{t_{\max}}}{6}\sum_i \omega_i t_i^2. \tag{C.170}$$

For the isotropic Gaussian soft block,

$$\langle |z|^2\rangle_{\mathrm{G}} = \frac{d_\perp}{\mathcal{A}a_1\delta}. \tag{C.171}$$

Thus

$$t_{\max,\mathrm{rms}}^2 \lesssim \frac{4d_\perp b^2}{\mathcal{A}a_1\delta}. \tag{C.172}$$

The local field expansion is controlled by $\mathcal{A}a_1\delta \gg d_\perp b^2$, with fixed numerical factors absorbed in the asymptotic symbol $\gg$.

The exchange coefficients remain bounded throughout every closed coupling interval contained in $0 < k < 1$. Indeed, monotonicity of $P(w)/w^2$ gives

$$f(w) \le \left(\frac{w}{\vartheta}\right)^2, \tag{C.173}$$

and monotonicity of $\sin w/w$ on $0 < w < \vartheta < \pi$ then gives

$$J_n \le \frac{\vartheta}{(2n-1)\sin^2\vartheta}, \qquad n = 3, 4, \qquad \mathcal{I}_f \le \frac{\vartheta}{5\sin^4\vartheta\,(2+\pi^2/\vartheta^2)}. \tag{C.174}$$

The exact finite-radius boundary map gives continuous corrections to these endpoint vertices.

The upper end of the expansion is fixed by the outer geometric scale. For an outer length L,

$$\frac{\delta}{L^2} \ll 1. \tag{C.175}$$

Combining this condition with the field-range and Gaussian bounds, I define

$$\mathcal{C}_{\mathrm{ctl}} = \max\left\{\frac{d_\perp b^2}{a_1}, \mathcal{C}_Z, \mathcal{C}_V\right\}, \qquad \frac{\mathcal{C}_{\mathrm{ctl}}}{\mathcal{A}} \ll \delta \ll L^2. \tag{C.176}$$

Fixed order-one constants are absorbed into the definition of the asymptotic window in Eq. (C.176). With this convention, the equal two-factor example at $k = 1/2$ has

$$\mathcal{C}_{\mathrm{ctl}} = \frac{1}{6\pi}. \tag{C.177}$$

Its connected variance receives the relative correction

$$\frac{10-\pi^2}{24\pi\Lambda_*}=\frac{0.00172942534\ldots}{\Lambda_*}, \tag{C.178}$$

in agreement with the negative net quartic coefficient in Eq. (C.149).

The two inequalities in Eq. (C.176) admit, for example,

$$\delta=L\sqrt{\frac{\mathcal{C}_{\rm ctl}}{\mathcal{A}}} \tag{C.179}$$

whenever $\mathcal{A}L^2\gg\mathcal{C}_{\rm ctl}$. For equal product couplings at fixed effective β, $\mathcal{C}_{\rm ctl}$ grows at most as p^2. A simultaneous large-p limit therefore requires

$$\mathcal{A}\delta\gg p^2. \tag{C.180}$$

The product truncation includes the homogeneous dilaton/saxion, axion, and radius responses through this order. The controlled near-BPS limit is

$$\frac{\delta}{L^2}\longrightarrow 0,\qquad \frac{\mathcal{A}\delta}{\mathcal{C}_{\rm ctl}}\longrightarrow\infty. \tag{C.181}$$

At fixed $\mathcal{A}$, the Gaussian regime terminates before the literal endpoint $\delta=0$ is reached. A complete endpoint treatment must then use the higher vertices and the full fixed-charge measure. The finite complete BPS weight entering Eq. (C.118) remains a separate matching datum.

C.6 Coupled angular modes and radial resonance

For $\ell>0$, the axion fluctuations remain dynamical. The homogeneous fixed-charge Routhian eliminates only the conserved radial axion momenta. Angular dependence permits radial charge density to flow into the angular current, so the axion and dilaton/saxion fluctuations must be solved as a coupled system.

Let

$$-\nabla^2_{S^3}Y_{\ell m}=\lambda_\ell Y_{\ell m},\qquad \lambda_\ell=\ell(\ell+2). \tag{C.182}$$

For one transverse dilaton/saxion direction write

$$\delta\phi_i=E_{iu}q^uY_{\ell m},\qquad \delta\chi_i=\xi_iY_{\ell m}. \tag{C.183}$$

Before the fixed-charge Legendre transform, expansion of the Euclidean axion kinetic term gives the mixed quadratic contribution

$$I^{(2)}_{q\chi}\supset -2\mathcal{A}\sum_i\beta_iE_{iu}\nu_i\int \mathrm{d}\tau\, q^u\partial_\tau\xi_i. \tag{C.184}$$

For $\ell=0$, the perturbed radial charges remain conserved and the axion derivatives may be eliminated at fixed charge. For $\ell>0$, current conservation instead gives

$$\partial_\tau(\delta\nu_i)=-\lambda_\ell a\,\mathcal{G}^\chi_{ii}\xi_i, \tag{C.185}$$

where

$$\nu_i=-a^3\mathcal{G}^\chi_{ii}\partial_\tau\chi_i$$

in proper-radial gauge. Thus $\delta\nu_i$ is no longer radially constant, and ξ_i remains part of the fluctuation system.

I first determine the BPS radial operator. On the outward BPS branch I use a as the radial coordinate, so $a' = 1$ and primes below denote $\mathrm{d}/\mathrm{d}a$. Combining the stationary product relation derived in Appendix C.3 with the BPS background gives, on every active factor,

$$\nu_i^2 \mathrm{e}^{2\beta_i \bar{\phi}_i} = \frac{4a^4}{\beta_i^2}. \tag{C.186}$$

For the transverse axion block define

$$c_i = \frac{\beta_i \nu_i}{2a^2}\xi_i, \qquad c_i = E_{iu}c^u. \tag{C.187}$$

For one transverse pair (q, c), suppressing the common normalization and harmonic degeneracy, the BPS quadratic Lagrangian is

$$L_\ell^{(2)} = \frac{1}{2}a^3 q'^2 - \frac{1}{2}a^3 c'^2 + \frac{a\lambda_\ell}{2}(q^2 - c^2) - 4aq^2 + 4a^2 q' c. \tag{C.188}$$

The negative axion kinetic term is the Euclidean contour convention before the fixed-charge transform. The Euler equations are

$$\begin{aligned} a^2 q'' + 3aq' + (8 - \lambda_\ell)q + 4ac' + 8c = 0, \\ a^2 c'' + 3ac' - \lambda_\ell c + 4aq' = 0. \end{aligned} \tag{C.189}$$

For a local power

$$(q, c) = a^s (Q, C), \tag{C.190}$$

set

$$x = s(s + 2). \tag{C.191}$$

The indicial matrix is

$$\mathbb{M}_\ell(s) = \begin{pmatrix} x + 8 - \lambda_\ell & 4(s + 2) \\ 4s & x - \lambda_\ell \end{pmatrix}. \tag{C.192}$$

Its determinant factorizes exactly:

$$\det \mathbb{M}_\ell(s) = [s - (\ell - 2)](s + \ell)[s - (\ell + 2)](s + \ell + 4). \tag{C.193}$$

The coupled transverse axion–dilaton/saxion block therefore has the four BPS indices

$$s = \ell - 2, \qquad -\ell, \qquad \ell + 2, \qquad -\ell - 4, \tag{C.194}$$

counted with multiplicity. These are local radial indices. The physical boundary spectrum follows only after the boundary domain and the two-end matching are imposed.

The $\ell = 1$ sector already contains a repeated BPS index. Its roots are

$$3, \quad -1, \quad -1, \quad -5. \tag{C.195}$$

At $s = -1$, $\mathbb{M}_1(-1)$ has rank one. With

$$v = \begin{pmatrix} 1 \\ -1 \end{pmatrix}, \qquad v_1 = \begin{pmatrix} 1 \\ 0 \end{pmatrix}, \tag{C.196}$$

one finds

$$\mathbb{M}_1(-1)v = 0, \qquad \mathbb{M}_1(-1)v_1 + \mathbb{M}_1'(-1)v = 0. \tag{C.197}$$

A complete local BPS basis is

$$a^3\begin{pmatrix}1\\-1\end{pmatrix},\qquad a^{-1}\begin{pmatrix}1\\-1\end{pmatrix},\qquad a^{-1}\left[\begin{pmatrix}1\\-1\end{pmatrix}\log\frac{a}{a_{\rm ref}}+\begin{pmatrix}1\\0\end{pmatrix}\right],\qquad a^{-5}\begin{pmatrix}3\\5\end{pmatrix}. \tag{C.198}$$

The fixed radius $a_{\rm ref}>0$ sets the logarithm's origin. The Wronskian of these four solutions, with rows (q,c,q',c'), is

$$-128a^{-6}. \tag{C.199}$$

Changing $a_{\rm ref}$ shifts the logarithmic solution by a multiple of the ordinary $a^{-1}v$ solution. This logarithm is already part of the BPS Frobenius basis. Whether a finite-radius deformation excites it is a separate matching question.

I now expand the finite-radius equations in the BPS overlap region. Set

$$a=a_*\rho,\qquad k^2=3\beta^2,\qquad f_\rho=\sqrt{1-\rho^{-4}}. \tag{C.200}$$

For the limiting right inner background $\alpha_*\to\theta_\beta$, the large-ρ expansion is

$$\begin{aligned} f_\rho &= 1-\frac{1}{2}\rho^{-4}+O(\rho^{-8}),\\ \frac{\beta\sqrt{U}}{2a_*^2} &= \rho^2\left[1-\frac{1-k^2}{6}\rho^{-4}+O(\rho^{-8})\right],\\ \beta\dot\psi &= \frac{2}{\rho}\left[1-\frac{1+2k^2}{6}\rho^{-4}+O(\rho^{-8})\right]. \end{aligned} \tag{C.201}$$

Here the dot denotes the inner coordinate t. The finite phase $\epsilon(\delta)$ is restored when the local overlap solution is matched to the physical outer data.

For the local resonance calculation define

$$D_\rho=\rho\partial_\rho,\qquad w=k\arcsin(\rho^{-2}). \tag{C.202}$$

The exact transverse pair equations on the limiting product background are

$$\begin{aligned} 0=&\left[(1-\rho^{-4})D_\rho^2+2D_\rho-\lambda_\ell+8k^2\rho^{-4}\csc^2 w\right]q\\ &+\left[4kf_\rho\rho^{-2}\csc w\,D_\rho+8k^2\rho^{-4}\csc w\cot w\right]c,\\ 0=&\left[(1-\rho^{-4})D_\rho^2+2D_\rho-\lambda_\ell+4k^2\rho^{-4}\right]c\\ &+4kf_\rho\rho^{-2}\csc w\,D_\rho q. \end{aligned} \tag{C.203}$$

In this overlap it is convenient to use the covariant axion variable

$$c_i=\mathrm{sgn}(\nu_i)\mathrm{e}^{-\beta_i\bar\phi_i}\xi_i. \tag{C.204}$$

Equation (C.186) shows that this definition agrees with Eq. (C.187) at the BPS endpoint.

Expanding f_ρ, $\csc w$, and $\cot w$ at large ρ gives

$$\mathbb{M}_\ell(D_\rho)+\rho^{-4}\mathbb{N}_\beta(D_\rho)+O(\rho^{-8}). \tag{C.205}$$

Acting on $\rho^s(Q,C)$, the first correction is

$$\mathbb{N}_\beta(s)=\begin{pmatrix}-s^2-\frac{8}{3}(1-k^2) & -\frac{2}{3}(4-k^2)s-\frac{4}{3}(2+k^2)\\ -\frac{2}{3}(4-k^2)s & -s^2+4k^2\end{pmatrix}. \tag{C.206}$$

The deformation lowers the radial power by four. A logarithm is forced only when the shifted power coincides with another BPS root and the corresponding forcing has nonzero projection onto the left null space of the indicial matrix.

For $\ell = 1$, the $s = 3$ branch reaches the repeated root $s = -1$ at first order. Equation (C.206) gives

$$\mathbb{N}_\beta(3)v = (2k^2 - 1)v. \tag{C.207}$$

The ordinary correction

$$v_{\text{corr}} = \begin{pmatrix} (1 - 2k^2)/4 \\ 0 \end{pmatrix} \tag{C.208}$$

satisfies

$$\mathbb{M}_1(-1)v_{\text{corr}} + \mathbb{N}_\beta(3)v = 0. \tag{C.209}$$

Thus the first finite-radius recurrence closes with an ordinary ρ^{-1} term. The repeated BPS root still supplies its logarithmic companion, but no new resonant logarithm is forced at this order. Its coefficient is determined by the global boundary matching.

For $\ell = 2$, the candidate resonance from $s = 4$ to $s = 0$ also cancels: the forcing has zero projection onto the left null vector at $s = 0$. The first nonvanishing finite-radius resonance occurs at $\ell = 3$. The BPS roots are

$$s = 5, \qquad 1, \qquad -3, \qquad -7. \tag{C.210}$$

The $5 \to 1$ and $-3 \to -7$ compatibility projections vanish. The $1 \to -3$ pair has right null vectors

$$v_+ = \begin{pmatrix} 3 \\ 1 \end{pmatrix}, \qquad v_- = \begin{pmatrix} -1 \\ 1 \end{pmatrix}, \tag{C.211}$$

while a left null vector of $\mathbb{M}_3(-3)$ is

$$w_-^T = (-3, 1). \tag{C.212}$$

Direct evaluation gives

$$\begin{aligned} w_-^T \mathbb{N}_\beta(1) v_+ &= 40 - 16k^2 = 40 - 48\beta^2, \\ w_-^T \mathbb{M}_3'(-3) v_- &= -32. \end{aligned} \tag{C.213}$$

On the branch $0 < k < 1$, the first quantity is strictly positive. The compatibility condition therefore requires a logarithm.

At order ρ^{-3} write

$$\rho^{-3} \left[\kappa_3 \log \rho \, v_- + u \right]. \tag{C.214}$$

The recurrence becomes

$$\mathbb{M}_3(-3)u + \kappa_3 \mathbb{M}_3'(-3)v_- + \mathbb{N}_\beta(1)v_+ = 0. \tag{C.215}$$

Multiplication by w_-^T removes the ordinary vector u and fixes

$$\kappa_3 = -\frac{w_-^T \mathbb{N}_\beta(1) v_+}{w_-^T \mathbb{M}_3'(-3) v_-} = \frac{5 - 2k^2}{4} = \frac{5 - 6\beta^2}{4}. \tag{C.216}$$

One convenient choice of ordinary completion gives

$$\Psi_+(\rho) = \rho v_+ + \kappa_3 \rho^{-3} \log \rho \, v_- + \rho^{-3} \left[\begin{pmatrix} (10k^2 - 19)/12 \\ 0 \end{pmatrix} + b \, v_- \right] + \cdots, \qquad \kappa_3 = \frac{5 - 6\beta^2}{4}. \tag{C.217}$$

Substitution into both coupled equations verifies the logarithmic and ordinary terms. The coefficient b multiplies the homogeneous $\rho^{-3}v_-$ solution and is fixed by matching. A regular change of fluctuation variables can shift this ordinary term, whereas the resonance residue κ_3 is invariant.

The inner logarithm now determines the nonanalytic order seen at fixed outer radius. Since

$$\rho = \frac{a}{a_*}, \qquad a_*^2 = \delta, \tag{C.218}$$

normalize the leading branch as $a\,v_+ = a_*\rho v_+$. Equation (C.217) then contains

$$a_*\Psi_+(a/a_*) \supset \frac{\kappa_3\delta^2}{a^3}\log\frac{a}{\sqrt{\delta}}\,v_-. \tag{C.219}$$

Thus the first nonvanishing finite-radius angular resonance enters the outer solution at

$$O\big(\delta^2\log\delta\big)\,. \tag{C.220}$$

Its first derivative with respect to δ vanishes as $\delta \to 0^+$. It therefore does not modify the linear endpoint slope obtained from the homogeneous transverse mode.

The logarithm also carries the standard matching-scale freedom of a resonant Frobenius expansion. The BPS overlap operator is covariant under radial dilatations, while the first finite-radius correction lowers the radial weight by four. For two independent solutions labelled by their boundary data, write the resonant part as

$$\rho^{-3}\left[\kappa_3\log\frac{\rho}{\mu_\rho} + b_j(\mu_\rho)\right]v_-, \qquad j = 1, 2. \tag{C.221}$$

Independence of the physical solution from the arbitrary overlap scale μ_ρ gives

$$\frac{\mathrm{d}b_j}{\mathrm{d}\log\mu_\rho} = \kappa_3. \tag{C.222}$$

Hence $b_1 - b_2$ is matching-scale invariant. The common running is the classical radial resonance; the physical boundary map converts the invariant matched data and the residue κ_3 into the finite-radius response. The exact transformation in the next subsection supplies that boundary map and reproduces the angular resonance directly.

C.7 Exact angular matching and the gravity mode

The coupled product system admits an exact field transformation that separates the bulk angular equations. I use this transformation to construct the physical two-boundary map at finite radius while retaining the generic matter phase.

With

$$Q = (q, c)^T,$$

the finite-radius quadratic density divided by $\mathcal{A}\delta$ is

$$\begin{aligned} L_Q = {} & q_y^2 - (c_y + k\cot w\,c)^2 + \frac{\lambda_\ell}{4\cos^2 y}(q^2 - c^2) - 2k^2\csc^2 w\,q^2 \\ & - 4k\csc w\,q(c_y + k\cot w\,c). \end{aligned} \tag{C.223}$$

Introduce

$$Q = S(w)\begin{pmatrix} z_k \\ z_0 \end{pmatrix}, \qquad S(w) = \begin{pmatrix} \csc w & -\cot w \\ -\cot w & \csc w \end{pmatrix}, \qquad \det S = 1. \tag{C.224}$$

Direct substitution gives the exact identity

$$L_Q = z_{k,y}^2 - z_{0,y}^2 + \frac{\lambda_\ell}{4\cos^2 y}(z_k^2 - z_0^2) - k^2 z_k^2 + \partial_y(Q^T T Q),$$
$$T(w) = \begin{pmatrix} 0 & -k\csc w \\ -k\csc w & -k\cot w \end{pmatrix}. \tag{C.225}$$

The two bulk fields therefore satisfy the same Pöschl–Teller equation with two fixed values of the parameter,

$$\left[-\partial_y^2 + \frac{\lambda_\ell}{4\cos^2 y}\right] z_\eta = \eta^2 z_\eta, \qquad \eta = k, 0. \tag{C.226}$$

The transformation removes the asymmetric matter phase from the bulk operator. That phase survives entirely in the boundary matrices $S(w)$ and $T(w)$.

This separation is useful because reflection symmetry is obscured in the original variables. For a scalar equation $q'' = Vq$, decomposition into even and odd parts gives

$$q_e'' = V_e q_e + V_o q_o, \qquad q_o'' = V_e q_o + V_o q_e. \tag{C.227}$$

For

$$V(y) = 2k^2 \csc^2(\alpha_* - ky),$$

the odd part V_o is nonzero at generic α_*. The original parity sectors therefore mix. Equation (C.226), by contrast, has even coefficients. I solve it in an even–odd basis and reconstruct the asymmetric physical variables only at the boundaries.

Set

$$g = \frac{\ell + 2}{2}.$$

A normalized even and odd pair for each η is

$$e_\eta(y) = (\cos y)^g {}_2F_1\left(\frac{g+\eta}{2}, \frac{g-\eta}{2}; \frac{1}{2}; \sin^2 y\right),$$
$$o_\eta(y) = \sin y\,(\cos y)^g {}_2F_1\left(\frac{g+\eta+1}{2}, \frac{g-\eta+1}{2}; \frac{3}{2}; \sin^2 y\right). \tag{C.228}$$

They obey

$$e_\eta(0) = 1, \qquad e_\eta'(0) = 0, \qquad o_\eta(0) = 0, \qquad o_\eta'(0) = 1,$$

and their Wronskian is unity.

Place equal physical cuts at $a = R$. Since

$$a^2 = \delta \sec y,$$

the cuts lie at

$$Y = \arccos \frac{\delta}{R^2}.$$

For each transformed channel define

$$d_\eta = \delta\left(\frac{e_\eta'}{e_\eta} + \frac{o_\eta'}{o_\eta}\right)_{y=Y}, \quad x_\eta = -\frac{\delta}{e_\eta(Y) o_\eta(Y)}, \quad D_\partial = \mathrm{diag}(d_k, -d_0), \quad X_\partial = \mathrm{diag}(x_k, -x_0). \tag{C.229}$$

The relative minus signs in the $\eta = 0$ channel follow from the opposite kinetic sign in Eq. (C.225).

At the left and right cuts,

$$w_L = \alpha_* + kY, \qquad w_R = \alpha_* - kY,$$

and I write

$$S_{L,R} = S(w_{L,R}), \qquad T_{L,R} = T(w_{L,R}).$$

The physical outer Dirichlet Hessian, with the common normalization $\mathcal{A}$ removed, has blocks

$$\begin{aligned} K^Q_{LL} &= S_L^{-T} D_\partial S_L^{-1} - 2\delta T_L, \\ K^Q_{RR} &= S_R^{-T} D_\partial S_R^{-1} + 2\delta T_R, \\ K^Q_{LR} &= S_L^{-T} X_\partial S_R^{-1}, \qquad K^Q_{RL} = (K^Q_{LR})^T. \end{aligned} \tag{C.230}$$

Thus

$$\mathcal{K}^\partial_{\boldsymbol{\nu},B} = \mathcal{A} K^Q$$

in this angular block. The terms proportional to $T_{L,R}$ come from the total derivative in Eq. (C.225). They are part of the physical Dirichlet Hessian. The matrices S_L, S_R, T_L, and T_R carry the asymmetry of the charged matter profile, while the bulk propagation is controlled by the even equation (C.226).

The outer matrix K^Q is distinct from the artificial interface Hessian $\mathcal{K}^\Sigma$. Changing the physical boundary ensemble requires the corresponding Legendre transform. Likewise, matching to asymptotic multipole sources requires the source normalization and local subtraction specified by the observable.

The exact transformed equation also gives a closed recurrence for the overlap expansion. In the inner radial coordinate ρ, Eq. (C.226) becomes

$$\left[P_\ell(D_\rho) + \rho^{-4}\left(4\eta^2 - D_\rho^2\right)\right] z_\eta = 0, \qquad P_\ell(s) = s(s+2) - \ell(\ell+2), \qquad D_\rho = \rho\partial_\rho. \tag{C.231}$$

For the branch beginning with ρ^ℓ, write

$$z_\eta = \rho^\ell \sum_{n\geq 0} a_n \rho^{-4n}, \qquad a_0 = 1.$$

Matching equal powers gives

$$a_n = \frac{(\ell - 4n + 4)^2 - 4\eta^2}{P_\ell(\ell - 4n)} a_{n-1}. \tag{C.232}$$

The second indicial root of this scalar equation is $-\ell - 2$. The descending sequence $\ell - 4n$ reaches this root only for odd ℓ. For

$$n_* = \frac{\ell + 1}{2},$$

the resonant denominator in Eq. (C.232) vanishes. The coefficient of $\rho^{-\ell-2}\log\rho$ is

$$\gamma_\ell(\eta) = \frac{\displaystyle\prod_{j=1}^{n_*}\left[4\eta^2 - (2j-1)^2\right]}{4n_*\, 16^{\,n_*-1}[(n_*-1)!]^2}. \tag{C.233}$$

For even ℓ, the power sequence never reaches the second root and this resonance is absent. For odd ℓ, a zero of any factor in the numerator cancels the corresponding logarithm.

For $\ell = 1$,

$$\gamma_1(\eta) = \eta^2 - \frac{1}{4}.$$

After the inverse transformation (C.224), the associated $\rho^{-3}\log\rho$ term maps to the repeated a^{-1} BPS branch identified in the preceding subsection. It is therefore the transformed representation of the $\ell = 1$ BPS logarithmic companion, rather than a new first-order finite-radius resonance of the physical (q, c) system. This agrees with the direct recurrence, where the first finite-radius correction in the $\ell = 1$ block closes with an ordinary power.

For $\ell = 3$, the transformed recurrence reaches the second root at $n_* = 2$. After transforming back to (q, c), the resulting logarithm reproduces the $\rho^{-3}\log\rho$ structure of Eq. (C.217). At fixed outer radius it therefore enters the physical solution at

$$\delta^2 \log\frac{\delta}{\delta_0},$$

up to the matched reference scale δ_0. Its first derivative with respect to δ vanishes at the BPS endpoint. The exact transformation thus confirms the resonance found from the coupled indicial recurrence and supplies its complete two-boundary map.

I next separate genuine fluctuation modes from collective directions. Spatial rotations leave every radial background field invariant and generate no radial fluctuation. Their stabilizer volume belongs to the gauge treatment. When a common translation is an admissible collective coordinate, its scalar variation is proportional to

$$\delta\phi_i \propto n_i\sigma'\,\epsilon\cdot\hat{x}.$$

Its transverse projection vanishes because

$$E^T n = 0,$$

and the corresponding transverse axion projection vanishes as well. The transverse angular block studied above therefore contains no translation collective mode.

At a finite Dirichlet cut, $Y < \pi/2$. The lowest Dirichlet eigenvalue of $-\partial_y^2$ on $[-Y, Y]$ is

$$\left(\frac{\pi}{2Y}\right)^2 > 1.$$

Since

$$0 \le \eta^2 \le k^2 < 1$$

on the branch studied here and $\lambda_\ell/(4\cos^2 y) > 0$ for $\ell \ge 1$, the operators

$$-\partial_y^2 + \frac{\lambda_\ell}{4\cos^2 y} - \eta^2$$

are strictly positive on the finite-cut Dirichlet domain. Each transformed scalar channel therefore has trivial zero-frequency kernel. The original (q, c) action still carries opposite kinetic signs before the axion contour rotation. The positivity statement concerns the transformed Dirichlet Sturm–Liouville operators, rather than the unreduced Euclidean gravity–matter action.

I now turn to the homogeneous scalar–gravity channel. The one-scalar reduction in Eq. (C.25) gives a regular constraint-reduced description. In the BPS interior scaling region with $\Lambda = 0$,

$$F = \frac{2a^2}{\beta}, \qquad p_a = -12a, \qquad \omega = \frac{2}{\beta a}. \tag{C.234}$$

Equations (C.27)–(C.29) then give

$$F_{p_a p_a} = \frac{\beta}{24}(1 - 3\beta^2), \qquad F_{p_a a} = -\beta - \frac{3}{2}\beta^3, \qquad F_{aa} = -30\beta - 18\beta^3. \tag{C.235}$$

Substitution into Eq. (C.25) gives, apart from the common factor $\mathcal{V}_3/(4\kappa_4^2)$,

$$-\frac{12}{1-3\beta^2}\,a\left(f'-\frac{2+3\beta^2}{a}f\right)^2-\frac{60+36\beta^2}{a}f^2. \tag{C.236}$$

Its Euler equation simplifies exactly to

$$a^2f''+af'-9f=0. \tag{C.237}$$

Hence

$$f_+\propto a^3, \qquad f_-\propto a^{-3}.$$

With fixed normalization of these local branches, their relative size at the minimal radius is

$$a_*^6=\delta^3. \tag{C.238}$$

This local power ratio identifies the natural mixing order of the scalar–gravity channel. The physical outer Hessian still requires propagation through the finite-radius boundary-value problem.

That propagation can be obtained directly by varying the exact background at fixed dilaton/saxion. On every interval with $\sigma'\neq 0$, two independent radius variations and their canonical momenta are

$$\begin{aligned} f_\alpha &= \frac{a}{2k}\tan y, & f_\delta &= \frac{a}{2\delta}\left(1-\frac{\tan y\tan w}{k}\right),\\ p_\alpha &= -12\sin y\, f_\alpha-\frac{12a\cos y}{k}, & p_\delta &= -12\sin y\, f_\delta+\frac{12a\cos y\tan w}{k\delta}. \end{aligned} \tag{C.239}$$

Their symplectic Wronskian is constant,

$$f_\delta p_\alpha-f_\alpha p_\delta=-\frac{6}{k}.$$

The matrix of outward canonical momenta multiplied by the inverse matrix of boundary values gives the exact Dirichlet-to-Neumann coefficient whenever the boundary-value map is nonsingular.

At equal cuts $a=R$, set

$$T_Y=\tan Y, \qquad w_L=\alpha_*+kY, \qquad w_R=\alpha_*-kY.$$

The off-diagonal scalar–gravity Hessian entry, with $\mathcal{A}$ removed, is

$$K_{LR}^{\mathrm{grav}}=\frac{24\delta}{R^2T_Y\,[2+(T_Y/k)(\tan w_L-\tan w_R)]}=\frac{24k\cot(\pi k)}{R^6}\delta^3+O(\delta^4). \tag{C.240}$$

The displayed expansion applies when the boundary-value map is nondegenerate and $\cos(\pi k)\neq 0$. It shows that the generic scalar–gravity off-diagonal Hessian begins at $O(\delta^3)$. Special coupling values can cancel this coefficient and move the first nonzero term to higher order. The corresponding covariance also depends on the diagonal entries and on the gravitational contour.

At a turning point of the scalar used as the clock, I return to the first-order constrained system of Eq. (C.15), choose another regular canonical coordinate, and continue the same physical boundary map.

The preceding calculations now determine the finite-radius deformation that enters the spectral analysis. At fixed physical outer coordinates, let

$$\mathcal{K}^{\partial}_{\boldsymbol{\nu},B}(\delta)$$

denote the two-sided outer-boundary Hessian. Define

$$\mathcal{D}^{\partial}_{\boldsymbol{\nu}} = \frac{\mathrm{d}}{\mathrm{d}\delta}\mathcal{K}^{\partial}_{\boldsymbol{\nu},B}(\delta)\bigg|_{0^+}. \tag{C.241}$$

This derivative follows the fixed-charge saddle family of Appendix A, with the physical outer coordinates and probe convention held fixed.

If the calculation uses an artificial radial cut, first eliminate the two Dirichlet interiors and form the joint Hessian on the physical outer values and the trace at Σ:

$$\mathcal{K}^{\partial}_{\boldsymbol{\nu},B} = \mathbb{H}_{\partial\partial} - \mathbb{H}_{\partial\Sigma}\mathbb{H}^{-1}_{\Sigma\Sigma}\mathbb{H}_{\Sigma\partial}, \qquad \mathbb{H}_{\Sigma\Sigma} = \mathcal{K}^{\Sigma}_{\boldsymbol{\nu},B}. \tag{C.242}$$

Every block in Eq. (C.242) uses the same boundary domain, coordinates, regulator, and local subtraction. The individual interface quantities depend on the position of Σ. Their Schur complement does not. This is the outer Hessian whose derivative enters the physical finite-radius response.

For a differentiable outer block,

$$\mathcal{K}^{\partial}_{\boldsymbol{\nu},B}(\delta) = \mathcal{K}^{\partial}_{\boldsymbol{\nu},B}(0) + \delta\mathcal{D}^{\partial}_{\boldsymbol{\nu}} + o(\delta). \tag{C.243}$$

If the observable retains a further outer subspace, let $\mathfrak{J}_0$ denote its endpoint stationary extension. The first deformation of the final reduced matrix is

$$D^{\mathrm{phys}}_{1,\boldsymbol{\nu}} = \mathfrak{J}_0^{\dagger}\mathcal{D}^{\partial}_{\boldsymbol{\nu}}\mathfrak{J}_0. \tag{C.244}$$

This is the stationary-extension identity of Eq. (B.50). On an exact endpoint kernel with a bounded complementary inverse, it reduces to direct projection.

The calculations above also separate the different powers of δ that occur in the paper:

Quantity	Leading finite-radius change
Fixed-radius outer background	$O(\delta^2)$
Inner transverse quadratic action	$O(\delta)$
Homogeneous transverse off-diagonal Hessian	$O(\delta^2)$
Homogeneous transverse cross covariance	$O(\delta)$
Scalar–gravity off-diagonal Hessian at generic stated cuts	$O(\delta^3)$
First nonvanishing angular resonance	$O(\delta^2 \log(\delta/\delta_0))$

The powers belong to different stages of the boundary reduction. The local inner action, the physical Hessian, and its inverse therefore need not begin at the same order.

In particular, the homogeneous transverse result gives

$$K'_{LL}(0) = a_1, \qquad K_{LR} = O(\delta^2), \qquad G_{LR} = g_{1,\boldsymbol{\nu}}\delta + O(\delta^2). \tag{C.245}$$

In the product system, the exact homogeneous transverse quadratic form remains positive at every allowed finite radius. Its local normalized potential Hessian is $\mathfrak{M} = 4\beta^2 I$. The endpoint derivative of the physical quadratic form on the soft subspace is positive semidefinite. The subtractive finite-rank deformations introduced later are separate spectral models and are not inferred from this product calculation.

For an invertible regulated endpoint block $M_{0,\nu}$ and one fixed scalar source contraction, the relative Gaussian bosonic two-source coefficient is

$$\frac{\Pi_{B,\boldsymbol{\nu}}(\delta)}{\Pi_{B,\boldsymbol{\nu}}(0)} = \mathcal{R}_{\boldsymbol{\nu},\mathrm{comp}}(\delta)\left[\frac{\det M_{\boldsymbol{\nu},B}(\delta)}{\det M_{0,\boldsymbol{\nu}}}\right]^{-1/2} \times \frac{\mathcal{V}_{\boldsymbol{\nu}}(\delta)+G_{\boldsymbol{\nu},Q}(\delta)+\mathbf{b}^{\mathrm{eff}}_{\boldsymbol{\nu}}(\delta)^{\dagger}M_{\boldsymbol{\nu},B}(\delta)^{-1}\mathbf{b}^{\mathrm{eff}}_{\boldsymbol{\nu}}(\delta)}{\mathcal{V}_{\boldsymbol{\nu}}(0)+G_{\boldsymbol{\nu},Q}(0)+\mathbf{b}^{\mathrm{eff}}_{\boldsymbol{\nu}}(0)^{\dagger}M^{-1}_{0,\boldsymbol{\nu}}\mathbf{b}^{\mathrm{eff}}_{\boldsymbol{\nu}}(0)}. \tag{C.246}$$

The complementary factor is normalized by

$$\mathcal{R}_{\boldsymbol{\nu},\mathrm{comp}}(0) = 1$$

and contains the remaining regulated bosonic contributions. Equation (C.246) applies to an invertible endpoint block with a nonzero endpoint source contraction. The singular homogeneous pair is instead treated exactly by Eq. (C.109).

Dividing an unnormalized two-source coefficient by its zero-source functional removes the determinant and other source-independent weights and leaves the connected Gaussian response. For the unnormalized coefficient those weights remain. In the homogeneous soft channel, $G_{LR}(0) = 0$, so the derivative of the zero-source weight multiplies zero at first order. Consequently the linear coefficient in Eq. (C.118) is $Z_{\boldsymbol{\nu},0}g_{1,\boldsymbol{\nu}}$ independently of the first derivative of a finite differentiable weight.

The exact radial analysis therefore supplies three distinct inputs for the later spectral problem. The homogeneous transverse block gives the linear cross covariance. The coupled angular block gives the first resonant $\delta^2\log\delta$ correction. The scalar–gravity block begins at cubic order in its off-diagonal Hessian at generic cuts. The compactification and the complete fixed-charge measure determine how these mode-dependent responses enter the full sector coefficient.

D Charge structure and endpoint spectrum

D.1 Charge dependence

The finite-radius response is computed charge sector by charge sector. I now separate three levels of charge dependence: the local dependence of the fluctuation operator on the charge bilinears, the dependence of the reduced scalar coefficient on the charge lattice, and the matrix-valued information carried by the reduced Hessian. These levels coincide only under additional factorization assumptions.

For axion charges $\boldsymbol{\nu} \in \mathbb{Z}^r$ and dilaton/saxions ϕ^A, the fixed-charge potential is

$$U_{\boldsymbol{\nu}}(\phi) = \nu_i \mathcal{G}^{ij}_{\chi}(\phi)\nu_j. \tag{D.1}$$

Its covariant second variation contains

$$\Delta^{(2)}U_{\boldsymbol{\nu}} = \frac{1}{2}\xi^A\xi^B\nu_i\nabla_A\nabla_B\mathcal{G}^{ij}_{\chi}(\phi)\nu_j. \tag{D.2}$$

This term supplies only the local charge-dependent potential. The physical quadratic form also contains the kinetic terms, target curvature, gravitational constraint, form-field mixing, and boundary form.

Let e_a denote a coordinate vector in the final reduced boundary space, and let

$$\Psi_a = \mathfrak{J}e_a$$

be its stationary bulk extension after all complementary bosonic variables have been eliminated. The exact reduced bosonic matrix is then

$$\begin{aligned}[M_{\boldsymbol{\nu},B}]_{ab} &= \mathfrak{h}_{\boldsymbol{\nu},B}[\Psi_a,\Psi_b] \\ &= \int \mathrm{d}\tau\, \left[\dot{\Psi}_a^\dagger A\dot{\Psi}_b + \dot{\Psi}_a^\dagger B\Psi_b + \Psi_a^\dagger B^\dagger\dot{\Psi}_b + \Psi_a^\dagger C\Psi_b\right] + \mathfrak{h}_{\boldsymbol{\nu},\partial}[\Psi_a,\Psi_b]. \end{aligned} \tag{D.3}$$

Here $\mathfrak{h}_{\boldsymbol{\nu},B}[\cdot,\cdot]$ is the complete normalized bosonic quadratic form on the physical domain. The stationary extension $\mathfrak{J}$ already contains the response of the eliminated fields. Adding a separate relaxation term to Eq. (D.3) would therefore double count their Schur-complement contribution.

The charge dependence is most cleanly differentiated before imposing the rank-one relation between charge bilinears. Introduce independent symmetric variables $t_{ij} = t_{ji}$ as in Appendix B. Around a fixed reference point t^0,

$$M_B(t;\delta) = M_B(t^0;\delta) + \sum_{i\le j}(t_{ij}-t^0_{ij})X_{ij}(\delta) + O(\|t-t^0\|^2), \qquad X_{ij} = \partial_{t_{ij}} M_B\big|_{t^0}. \tag{D.4}$$

Every derivative in Eq. (D.4) includes both the explicit charge dependence of the fluctuation operator and the induced displacement of the background at fixed physical outer data. It also includes transport of the chosen reduced basis. Only after differentiation do I restrict to the physical locus

$$t_{ij} = \nu_i\nu_j.$$

Thus Eq. (D.4) is a local matrix expansion in the independent bilinears, rather than a statement that the physical charge dependence is affine. Matrix inversion, Schur reduction, and motion of the saddle generally generate nonpolynomial dependence on $\boldsymbol{\nu}$. The same charge variation acts on the fermionic block, effective source vectors, complementary response, exact-mode factors, and normalization.

The homogeneous product model gives one part of this dependence in closed form. With the C^1 endpoint matching used in Eq. (C.118), Eq. (C.110) gives

$$g_{1,\boldsymbol{\nu}} = \frac{6h^2}{\mathcal{A}kV_{\boldsymbol{\nu}}v_1}, \qquad B_{\boldsymbol{\nu}} = Z_{\boldsymbol{\nu},0}g_{1,\boldsymbol{\nu}}, \qquad C^{LR}_{\boldsymbol{\nu}} = \delta B_{\boldsymbol{\nu}} + O(\delta^2). \tag{D.5}$$

The factor $g_{1,\boldsymbol{\nu}}$ is the geometric response multiplier. The factor $Z_{\boldsymbol{\nu},0}$ is the complete BPS sector weight. Their product gives the leading unnormalized finite-radius coefficient.

For the stationary product trajectory, define

$$\omega_i = \frac{\beta^2}{\beta_i^2}, \qquad \sum_i \omega_i = 1.$$

At the stationary point, Eq. (C.85) gives $X_i = c/\beta_i^2$. Taking logarithms and using $n^T Es = 0$ yields

$$V_{\boldsymbol{\nu}} = \prod_i \left(\frac{\nu_i^2}{\omega_i}\right)^{\omega_i}, \qquad V_{t\boldsymbol{\nu}} = t^2 V_{\boldsymbol{\nu}}, \qquad g_{1,t\boldsymbol{\nu}} = t^{-2} g_{1,\boldsymbol{\nu}}. \tag{D.6}$$

These identities hold at fixed active support, fixed couplings, and fixed right scaling datum h. The geometric multiplier is real and positive. It changes the magnitude of a complex BPS coefficient while leaving its phase unchanged. Sectors with the same $V_{\boldsymbol{\nu}}$ therefore have the same homogeneous geometric multiplier under the same boundary prescription.

The closed form in Eq. (D.6) applies to the stationary product submanifold. At a fixed right asymptotic dilaton/saxion vector, a charge sector lies on this submanifold precisely when

$$\beta_i^2\nu_i^2 \mathrm{e}^{2\beta_i\phi_{i,R}} = \beta_j^2\nu_j^2\mathrm{e}^{2\beta_j\phi_{j,R}} \qquad \text{for all active } i,j. \tag{D.7}$$

Sign-related sectors satisfy the same condition because the background depends on ν_i^2. They therefore share the same stationary trajectory and the same geometric response. Changing relative charge magnitudes generally violates Eq. (D.7) at fixed ϕ_R and moves the stationary trajectory. Those charge variations are obtained from the sensitivity equations of Appendix B, rather than by applying Eq. (D.6) at a fixed background.

The scalar coefficient that enters the charge-sector construction must be formed only after the complete fixed-charge fluctuation problem has been reduced. At quadratic order,

$$\Pi_{\boldsymbol{\nu}} = R_b\left[\mathcal{A}_{\boldsymbol{\nu},Q}\frac{\mathrm{Pf}M_{\boldsymbol{\nu},F}}{\sqrt{|\det M_{\boldsymbol{\nu},B}|}}\left(G_{\boldsymbol{\nu},Q} + (\mathbf{b}_{\boldsymbol{\nu}}^{\mathrm{eff}})^\dagger M_{\boldsymbol{\nu},B}^{-1}\mathbf{b}_{\boldsymbol{\nu}}^{\mathrm{eff}} + \mathcal{V}_{\boldsymbol{\nu},\mathrm{eff}}\right)\right] + \Pi_{\boldsymbol{\nu},\mathrm{higher}}. \tag{D.8}$$

Here $\Pi_{\boldsymbol{\nu},\mathrm{higher}}$ denotes the already reduced non-Gaussian and source-dependent corrections. The absolute-value notation in Eq. (D.8) refers to the real self-adjoint patch; a complex saddle uses the determinant branch fixed by its contour.

The same reduced matrix appears in both the bosonic determinant and the source response. An eigenvalue $\lambda \to 0^+$ contributes $\lambda^{-1/2}$ to the bosonic determinant factor and λ^{-1} to a source contraction with nonzero overlap. Exact-mode measures, saturation insertions, fermions, ghosts, contour phases, and the remaining fluctuation factors must therefore be included before a charge-sector coefficient is assigned.

For one isolated saddle, remove the classical exponential and define

$$\Pi_{\boldsymbol{\nu}}[b;\delta] = \mathrm{e}^{S_{\boldsymbol{\nu}}^{\mathrm{cl}}(\delta)}W_{\boldsymbol{\nu}}[b;\delta]. \tag{D.9}$$

This is the reduced coefficient after the operation R_b. For several saddles I construct $\Pi_{\boldsymbol{\nu},\mathfrak{s}}$ separately on each branch and sum the branch contributions only after their individual measures, phases, and zero-mode prescriptions have been fixed.

The scalar charge dependence can now be tested directly on the charge lattice. Let $\boldsymbol{e}_a$ denote the unit vector in charge direction a. For two distinct directions define the elementary mixed plaquette ratio

$$\mathfrak{K}_{ab}^{\mathrm{pre}}(\boldsymbol{\nu}) = \frac{\Pi_{\boldsymbol{\nu}+\boldsymbol{e}_a+\boldsymbol{e}_b}\Pi_{\boldsymbol{\nu}}}{\Pi_{\boldsymbol{\nu}+\boldsymbol{e}_a}\Pi_{\boldsymbol{\nu}+\boldsymbol{e}_b}}. \tag{D.10}$$

I use Eq. (D.10) only where all four coefficients are nonzero and are defined with the same boundary and reduction data. Unlike a logarithm, this multiplicative ratio is insensitive to the choice of a local logarithm branch.

Charge-factorization criterion. Suppose the reduced prefactor factorizes as

$$\Pi_{\boldsymbol{\nu}} = \prod_c f_c(\nu_c) \tag{D.11}$$

throughout the four sectors entering Eq. (D.10). Then

$$\mathfrak{K}_{ab}^{\mathrm{pre}}(\boldsymbol{\nu}) = 1, \qquad a \neq b. \tag{D.12}$$

Therefore $\mathfrak{K}_{ab}^{\mathrm{pre}} \neq 1$ proves nonfactorized dependence on the two charge directions.

To see this, note that every factor with $c \neq a, b$ cancels between numerator and denominator. The a- and b-dependent factors cancel separately.

The converse is local rather than global: $\mathfrak{K}_{ab}^{\mathrm{pre}} = 1$ at one charge plaquette does not prove factorization of the full charge family.

The geometric multiplier in Eq. (D.6) itself factorizes,

$$g_{1,\boldsymbol{\nu}} \propto \prod_i |\nu_i|^{-2\omega_i},$$

as long as all four sectors remain on the same active support and use the same stationary boundary prescription. It therefore cancels from Eq. (D.10). Under those conditions, the mixed plaquette ratio of

$$B_{\boldsymbol{\nu}} = Z_{\boldsymbol{\nu},0} g_{1,\boldsymbol{\nu}}$$

equals the corresponding ratio formed from $Z_{\boldsymbol{\nu},0}$. For generic independent charge increments at fixed physical outer data, however, the saddle moves and the four geometric multipliers must be recomputed from the charge-sensitivity problem. This distinction separates a special product-model factorization from the general charge dependence of the physical coefficient.

The reduced scalar ratio detects charge factorization, but it does not by itself resolve the matrix geometry that produced the coefficient. To expose that information, consider a positive Hermitian matrix $M(t_a, t_b)$ that is affine in two charge parameters near a reference point:

$$M = M_0 + t_a M_a + t_b M_b.$$

Whiten the two tangent matrices with M_0 and define

$$A = M_0^{-1/2} M_a M_0^{-1/2}, \qquad B = M_0^{-1/2} M_b M_0^{-1/2}, \qquad \mathcal{F} = -\frac{1}{2} \log\det M. \tag{D.13}$$

The fourth-order term of $-\frac{1}{2}\mathrm{Tr}\log(\boldsymbol{I} + t_a A + t_b B)$ contains the six words with two A's and two B's. Cyclicity reduces them to four copies of $\mathrm{Tr}(A^2B^2)$ and two copies of $\mathrm{Tr}(ABAB)$. Hence

$$\partial_a^2 \partial_b^2 \mathcal{F} = 2\mathrm{Tr}(A^2B^2) + \mathrm{Tr}(ABAB) = 3\mathrm{Tr}(A^2B^2) - \frac{1}{2}\|[A,B]\|_F^2. \tag{D.14}$$

The second equality uses

$$\|[A,B]\|_F^2 = 2\mathrm{Tr}(A^2B^2 - ABAB)$$

for Hermitian A and B. Thus the mixed fourth derivative contains both an ordinary positive contraction and a noncommutative correction. The derivative alone does not determine the commutator norm. Once $\mathrm{Tr}(A^2B^2)$ is obtained independently, Eq. (D.14) isolates $\|[A,B]\|_F^2$.

The affine assumption is essential to this simple formula. For a general one-parameter family $M(t)$, evaluate all derivatives at the reference point and define

$$X_j = M^{-1/2} M^{(j)} M^{-1/2}.$$

Four differentiations give

$$\mathcal{F}^{(4)} = -\frac{1}{2}\mathrm{Tr}\left[X_4 - 4X_1X_3 - 3X_2^2 + 12X_1^2X_2 - 6X_1^4\right]. \tag{D.15}$$

Cyclicity of the trace has already combined the distinct orderings in Eq. (D.15). Multivariable polarization produces the corresponding mixed derivatives. In the gravitational problem, the charge-sensitivity equations supply the derivatives of both the operator and the moving background. I therefore differentiate with respect to independent t_{ij} first and impose $t_{ij} = \nu_i\nu_j$ only after the matrix derivatives have been formed.

The scalar coefficient admits a parallel hierarchy directly on the charge lattice. Define

$$\Delta_a f(\boldsymbol{\nu}) = f(\boldsymbol{\nu} + \boldsymbol{e}_a) - f(\boldsymbol{\nu}).$$

On a nonvanishing charge domain choose one continuous branch of $\log \Pi_{\boldsymbol{\nu}}$ and form

$$\Delta_{a_1} \cdots \Delta_{a_k} \log \Pi_{\boldsymbol{\nu}}. \tag{D.16}$$

For distinct charge directions, these differences are discrete mixed cumulants of the reduced coefficient. If $\Pi_{\boldsymbol{\nu}} = \prod_a f_a(\nu_a)$, every mixed difference involving two or more distinct directions vanishes. If $\log \Pi_{\boldsymbol{\nu}}$ is a polynomial of total degree d, every finite difference of total order greater than d vanishes.

Neither statement follows from low matrix rank or from simultaneous diagonalizability of the charge-response matrices. A scalar example already shows the distinction:

$$\log(1 + t_a + t_b)$$

has mixed derivatives of arbitrarily high order even though there is no matrix noncommutativity at all. Thus nonzero mixed charge differences diagnose multi-charge dependence of the reduced scalar coefficient, whereas $\|[A, B]\|_F$ diagnoses noncommuting tangent directions of the matrix-valued response. These are independent structures.

This separation fixes the order of the subsequent analysis. The charge lattice carries scalar mixed ratios and higher finite differences only after the fixed-sector coefficient has been reduced. The endpoint spectrum carries eigenvalue and eigenvector information of the physical reduced matrix. Their joint use therefore requires the charge dependence of the matrix, its source vectors, and its sector weight to remain correlated rather than replacing them by independent marginal data.

D.2 BPS matrix ensemble and finite-radius correction

I now combine the finite-radius deformation with the BPS endpoint ensemble. I first identify the reduced BPS matrix and its hard-edge inverse moments in one fixed charge sector. I then insert the finite-radius deformation determined by the gravitational boundary problem.

The BPS factorization makes the physical endpoint Hessian positive. It does not determine a probability measure on positive matrices. For the microscopic endpoint model I use the central chiral Gaussian ensemble of Ref. [3]. The charge label $\boldsymbol{\nu}$, the rectangularity κ, and the Dyson index β_{D} remain distinct data.

Represent the endpoint square root by

$$\mathcal{Q} \in \mathbb{F}_{\beta_{\mathrm{D}}}^{(N+\kappa)\times N}, \qquad \mathrm{d}\mu(\mathcal{Q}) \propto \exp\left[-\frac{\beta_{\mathrm{D}}}{4}\mathrm{Tr}(\mathcal{Q}^\dagger \mathcal{Q})\right] \mathrm{d}\mathcal{Q}. \tag{D.17}$$

Here $\mathbb{F}_{\beta_{\mathrm{D}}} = \mathbb{R}, \mathbb{C}, \mathbb{H}$ for $\beta_{\mathrm{D}} = 1, 2, 4$, and $\kappa \geq 0$ is the rectangular defect. The Dyson index β_{D} is unrelated to the scalar coupling β.

Choose the retained m columns independently of the realization of $\mathcal{Q}$ and write

$$\mathcal{Q} = (X\ Y), \qquad X \in \mathbb{F}_{\beta_{\mathrm{D}}}^{(N+\kappa)\times m}, \qquad Y \in \mathbb{F}_{\beta_{\mathrm{D}}}^{(N+\kappa)\times n}, \qquad n = N - m. \tag{D.18}$$

Then

$$\mathcal{H}_0 = \mathcal{Q}^\dagger \mathcal{Q} = \begin{pmatrix} X^\dagger X & X^\dagger Y \\ Y^\dagger X & Y^\dagger Y \end{pmatrix}. \tag{D.19}$$

The Gaussian matrix Y has full column rank almost surely. Eliminating its columns gives the Schur complement

$$M_0 = X^\dagger X - X^\dagger Y (Y^\dagger Y)^{-1} Y^\dagger X = X^\dagger P_Y^\perp X, \tag{D.20}$$

with

$$P_Y^\perp = \boldsymbol{I} - Y(Y^\dagger Y)^{-1} Y^\dagger, \qquad \mathrm{rank} P_Y^\perp = m + \kappa. \tag{D.21}$$

Endpoint law after column elimination. Under the central measure (D.17), M_0 has the same law as $Z^\dagger Z$, where

$$Z \in \mathbb{F}_{\beta_{\mathrm{D}}}^{(m+\kappa)\times m}$$

is central Gaussian with the same variance convention. Its eigenvalue density is

$$\mathrm{d}\mu_{\mathrm{eig}}(\lambda) = \frac{1}{Z_{m,\kappa}^{(\beta_{\mathrm{D}})}} \prod_{a<b} |\lambda_a - \lambda_b|^{\beta_{\mathrm{D}}} \prod_{a=1}^{m} \lambda_a^{\frac{\beta_{\mathrm{D}}}{2}(\kappa+1)-1} \mathrm{e}^{-\frac{\beta_{\mathrm{D}}}{4}\lambda_a} \mathrm{d}\lambda_a. \tag{D.22}$$

The rectangularity κ is unchanged by the elimination. Moreover, M_0 is independent of $Y^\dagger Y$.

To see this, condition on Y and rotate the row space so that

$$P_Y^\perp = \mathrm{diag}(\boldsymbol{I}_{m+\kappa}, 0). \tag{D.23}$$

The distribution of X is invariant under this rotation and is independent of Y. Hence the conditional law of $X^\dagger P_Y^\perp X$ is independent of Y and equals the law of $Z^\dagger Z$. The singular-value Jacobian gives Eq. (D.22). See Ref. [23].

For $\beta_{\mathrm{D}} = 4$, trace and determinant count each quaternion eigenvalue once. If the physical operator is represented by a real or complex matrix with duplicated quaternion eigenvalues, its Gaussian determinant power must be matched to that representation. It cannot be inferred from Eq. (D.22) alone.

I next determine which inverse observables are integrable at the hard edge. Set

$$a_\kappa = \frac{\beta_{\mathrm{D}}}{2}(\kappa+1), \qquad b_{\mathrm{D}} = \frac{\beta_{\mathrm{D}}}{4}.$$

Multiplying the density by $(\det M_0)^u$ shifts the one-eigenvalue power by u. The Laguerre normalization therefore gives

$$\mathbb{E}[(\det M_0)^u] = b_{\mathrm{D}}^{-mu} \prod_{j=0}^{m-1} \frac{\Gamma(a_\kappa + u + j\beta_{\mathrm{D}}/2)}{\Gamma(a_\kappa + j\beta_{\mathrm{D}}/2)}, \qquad a_\kappa + u > 0. \tag{D.24}$$

For real u, this condition is exact.

Under the determinant-weighted measure, integration by parts gives

$$\mathbb{E}_u \mathrm{Tr} M_0^{-1} = \frac{m b_{\mathrm{D}}}{a_\kappa + u - 1}.$$

The pairwise Vandermonde derivatives cancel after summation over the eigenvalues. Rotational invariance then gives

$$\mathbb{E}[(\det M_0)^u M_0^{-1}] = \mathbb{E}[(\det M_0)^u] \frac{b_{\mathrm{D}}}{a_\kappa + u - 1} \boldsymbol{I}_m, \qquad a_\kappa + u > 1. \tag{D.25}$$

Several thresholds follow immediately:

$$\mathbb{E} M_0^{-1} < \infty \quad \Longleftrightarrow \quad a_\kappa > 1,$$

$$\mathbb{E}(\det M_0)^{-1/2} < \infty \quad \Longleftrightarrow \quad a_\kappa > \frac{1}{2},$$

and

$$\mathbb{E}\big[(\det M_0)^{-1/2} \mathbf{b}^\dagger M_0^{-1} \mathbf{b}\big] < \infty \quad \Longleftrightarrow \quad a_\kappa > \frac{3}{2}$$

for a fixed nonzero source vector $\mathbf{b}$ independent of the eigenvectors. A physical source correlated with M_0, a fermionic factor, or a vanishing source overlap changes the joint integrand and must be treated before these criteria are applied.

The same threshold is visible directly at the hard edge. Holding the other eigenvalues away from zero,

$$\mathrm{d}\mu_{\mathrm{eig}} \propto \lambda_{\mathrm{min}}^{a_\kappa - 1} \mathrm{d}\lambda_{\mathrm{min}}.$$

An unweighted inverse moment of order q therefore requires

$$a_\kappa > q.$$

These conditions concern the random positive eigenvalues of the BPS endpoint matrix. They are distinct from the deterministic soft eigenvalue $\lambda_{\mathrm{soft}} \propto \delta$ found in Eq. (C.104).

I now turn on the finite-radius deformation. For a finite regulated block that is analytic at the endpoint, write

$$M(\delta) = M_0 + \delta D_1 + \delta^2 D_2 + \cdots . \tag{D.26}$$

For fixed invertible M_0,

$$\begin{aligned} \log \frac{\det M(\delta)}{\det M_0} &= \delta \mathrm{Tr}(M_0^{-1} D_1) \\ &\quad + \delta^2 \left[\mathrm{Tr}(M_0^{-1} D_2) - \frac{1}{2} \mathrm{Tr}\big(M_0^{-1} D_1 M_0^{-1} D_1\big) \right] + O(\delta^3), \end{aligned} \tag{D.27}$$

and

$$\begin{aligned} M(\delta)^{-1} &= M_0^{-1} - \delta M_0^{-1} D_1 M_0^{-1} \\ &\quad + \delta^2 \left[M_0^{-1} D_1 M_0^{-1} D_1 M_0^{-1} - M_0^{-1} D_2 M_0^{-1} \right] + O(\delta^3). \end{aligned} \tag{D.28}$$

Termwise ensemble averaging of these formulas requires every displayed inverse moment to exist and the remainder to admit a common integrable bound. The hard-edge conditions above determine when this step is legitimate.

The matched deformation need not always be analytic in δ. For a mode with

$$M(\delta) = M_0 + \eta(\delta) D + \cdots ,$$

the radial calculation determines $\eta(\delta)$. The homogeneous mode gives ordinary powers. The $\ell = 3$ angular resonance gives

$$\eta(\delta) = \delta^2 \log \frac{\delta_0}{\delta}.$$

Its matrix coefficient is fixed by the physical boundary map Eq. (C.230). Thus the radial problem determines the strength and orientation of the deformation before the endpoint ensemble is averaged.

A deterministic finite-rank correction takes the form

$$M(\delta) = M_0 + U C(\delta) U^\dagger, \qquad U^\dagger U = \boldsymbol{I}_s. \tag{D.29}$$

Here U specifies the affected s-dimensional subspace. Define

$$S = U^\dagger M_0^{-1} U.$$

The matrix determinant lemma gives

$$\frac{\det M(\delta)}{\det M_0} = \det(\boldsymbol{I}_s + C(\delta) S)\,, \tag{D.30}$$

while the Woodbury identity gives

$$M(\delta)^{-1} = M_0^{-1} - M_0^{-1}U[\boldsymbol{I}_s + C(\delta)S]^{-1}C(\delta)U^\dagger M_0^{-1}. \tag{D.31}$$

Neither identity requires $C(\delta)$ to be invertible. The correction is controlled by three separate data: its rank, its strength, and the orientation of U relative to the endpoint eigenvectors.

The finite-rank family is a spectral diagnostic. It is not an identification of the positive transverse deformation derived in Appendix C. In particular, consider the subtractive model

$$C(\delta) = -\eta(\delta)G, \qquad G > 0, \qquad \eta(0) = 0.$$

A zero eigenvalue appears when

$$\det(\boldsymbol{I}_s - \eta GS) = 0. \tag{D.32}$$

To turn this exact condition into a probability law, I now specify the orientation of the perturbation. Assume that U is fixed independently of M_0 and define

$$\mathcal{Y} = \left(U^\dagger M_0^{-1} U\right)^{-1}. \tag{D.33}$$

Fixed-rank endpoint reduction. Let M_0 have the endpoint law (D.22), and let U be an $m \times s$ isometry fixed independently of M_0. Then $\mathcal{Y}$ has density

$$\mathrm{d}\mu(\mathcal{Y}) \propto (\det \mathcal{Y})^{\frac{\beta_{\mathrm{D}}}{2}(\kappa+1)-1} \exp\left[-\frac{\beta_{\mathrm{D}}}{4}\mathrm{Tr}\mathcal{Y}\right] \mathrm{d}\mathcal{Y}. \tag{D.34}$$

Equivalently, $\mathcal{Y}$ is an $s\times s$ Wishart matrix generated by $s+\kappa$ Gaussian rows. The rectangularity remains κ.

To see this, use orthogonal, unitary, or symplectic invariance to rotate U to the first s coordinate vectors and partition

$$M_0 = \begin{pmatrix} A & B \\ B^\dagger & D \end{pmatrix}. \tag{D.35}$$

The upper-left block of M_0^{-1} is

$$(A - BD^{-1}B^\dagger)^{-1}. \tag{D.36}$$

Hence Eq. (D.33) gives

$$\mathcal{Y} = A - BD^{-1}B^\dagger. \tag{D.37}$$

The partitioned Wishart theorem identifies this Schur complement with an $s \times s$ Wishart matrix having $s + \kappa$ rows. Equation (D.34) follows. See Ref. [23].

At fixed s and κ, the law in Eq. (D.34) contains no large-m scale. This fact controls the crossing threshold of a generic fixed finite-rank direction.

Write the subtractive model explicitly as

$$M(\delta) = M_0 - \eta(\delta)UGU^\dagger, \qquad G > 0, \qquad \eta(0) = 0. \tag{D.38}$$

Since $S = \mathcal{Y}^{-1}$, the first zero as a function of the positive strength η occurs at

$$\begin{aligned} \eta_c &= \frac{1}{\lambda_{\max}(G^{1/2}SG^{1/2})}, \\ &= \lambda_{\min}\left(G^{-1/2}\mathcal{Y}G^{-1/2}\right). \end{aligned} \tag{D.39}$$

A physical crossing occurs at a positive solution of

$$\eta(\delta_c) = \eta_c. \tag{D.40}$$

On a branch where $\eta(\delta)$ increases from zero, the first such solution is the first loss of positivity.

For $G = g\boldsymbol{I}_s$, η_c is the smallest eigenvalue of $\mathcal{Y}$ divided by g. The complete fixed-rank crossing law is therefore a smallest-eigenvalue law of an $s \times s$ Wishart matrix with the same rectangularity κ.

The rank-one case is elementary. Set

$$U = u, \qquad u^\dagger u = 1, \tag{D.41}$$

and define

$$y = \left(u^\dagger M_0^{-1} u\right)^{-1}, \qquad a_\kappa = \frac{\beta_{\mathrm{D}}}{2}(\kappa + 1). \tag{D.42}$$

Equation (D.34) with $s = 1$ gives the gamma density

$$p_y(y) = \frac{b_{\mathrm{D}}^{a_\kappa}}{\Gamma(a_\kappa)} y^{a_\kappa - 1} \mathrm{e}^{-b_{\mathrm{D}} y}, \qquad y > 0. \tag{D.43}$$

For $G = g$, one has

$$\eta_c = \frac{y}{g}. \tag{D.44}$$

Therefore

$$p(\eta_c) = \frac{(\beta_{\mathrm{D}} g/4)^{a_\kappa}}{\Gamma(a_\kappa)} \eta_c^{a_\kappa - 1} \exp\left[-\frac{\beta_{\mathrm{D}} g}{4}\eta_c\right], \qquad \eta_c > 0. \tag{D.45}$$

Its mean and variance are

$$\mathbb{E}\,\eta_c = \frac{2(\kappa+1)}{g}, \qquad \mathrm{Var}(\eta_c) = \frac{8(\kappa+1)}{\beta_{\mathrm{D}} g^2}. \tag{D.46}$$

For fixed $t > 0$,

$$\Pr\left(\eta_c < \frac{t}{m}\right) = \frac{\gamma\left(a_\kappa, \frac{\beta_{\mathrm{D}} g t}{4m}\right)}{\Gamma(a_\kappa)}. \tag{D.47}$$

As $m \to \infty$,

$$\Pr\left(\eta_c < \frac{t}{m}\right) \sim \frac{1}{\Gamma(a_\kappa + 1)} \left(\frac{\beta_{\mathrm{D}} g t}{4m}\right)^{a_\kappa}.$$

Thus a rank-one direction fixed independently of M_0 has an $O(1)$ crossing strength in the normalization of Eq. (D.22). Its probability of crossing already on the microscopic m^{-1} hard-edge scale is suppressed as m^{-a_κ}.

The same rank-one update gives exact source formulas. The determinant ratio is

$$\frac{\det M(\delta)}{\det M_0} = 1 - \frac{\eta(\delta)}{\eta_c}. \tag{D.48}$$

For a fixed source vector $\mathbf{b}$,

$$\mathbf{b}^\dagger M(\delta)^{-1}\mathbf{b} = \mathbf{b}^\dagger M_0^{-1}\mathbf{b} + \frac{\eta(\delta) g \left|u^\dagger M_0^{-1}\mathbf{b}\right|^2}{1 - \eta(\delta)/\eta_c}. \tag{D.49}$$

At $\eta(\delta_c) = \eta_c$, the determinant vanishes. The source contraction has a pole precisely when

$$u^\dagger M_0^{-1}\mathbf{b} \neq 0.$$

The quadratic integral then develops a zero direction, and its leading nonzero higher-order vertex controls the local saddle integral.

The distribution in Eq. (D.45) uses the independence of u and M_0. A physical perturbation whose orientation is determined by the same microscopic data as M_0 requires the joint law of

$$(M_0, u, g).$$

Equations (D.48) and (D.49), however, remain exact for every realization.

I finally compare the deformation strength with the microscopic hard edge. In the normalization of Eq. (D.22), the bulk eigenvalues are $O(m)$, whereas the smallest positive eigenvalues occur on the scale

$$\lambda_{\mathrm{hard}}(m) \sim m^{-1}, \qquad m \to \infty, \quad \kappa \text{ fixed.} \tag{D.50}$$

Equivalently, the normalized matrix $m^{-1}M_0$ has hard-edge scale m^{-2}.

For a general correction define

$$\chi(\delta) = \frac{\|M(\delta) - M_0\|_{\mathrm{op}}}{\lambda_{\mathrm{hard}}(m)}. \tag{D.51}$$

If $\chi(\delta) \to 0$ in probability, Weyl's eigenvalue bound makes the perturbation negligible on the microscopic hard-edge scale. When $\chi(\delta) = O(1)$, the matrix elements of the correction in the endpoint eigenbasis become leading data. Its norm alone no longer determines the shifted edge. The rank, orientation, and correlations with M_0 must then be kept.

This distinction is particularly sharp for fixed rank. A fixed subspace independent of M_0 has the $O(1)$ threshold derived above even though the smallest eigenvalues of M_0 are $O(m^{-1})$. A microscopic crossing at strength $O(m^{-1})$ therefore requires an atypically small compressed eigenvalue or a perturbation correlated with the hard-edge eigenvectors.

For comparison, the exactly solvable full-rank downward shift

$$M(\delta) = M_0 - g\eta(\delta)\boldsymbol{I}, \qquad g > 0, \tag{D.52}$$

moves every eigenvalue by the same amount. The number of negative eigenvalues is exactly

$$n_-(\delta) = \#\left\{a : \lambda_a(M_0) < g\eta(\delta)\right\}. \tag{D.53}$$

Its zero crossings are therefore governed directly by the hard-edge counting process.

The full-rank downward shift and the fixed-rank subtractive model are spectral diagnostics. The homogeneous transverse deformation derived in Appendix C instead has a positive endpoint derivative on its soft physical subspace. The physical sign, rank, strength, and orientation must therefore be taken from the radial and boundary calculation before any endpoint spectral average is performed.

E Statistics and bulk spectrum

E.1 Spectral averages and microscopic measure

I first fix the charge sector, saddle branch, boundary conditions, and reduction data. For each realization of the microscopic data, the reduced matrix has the matched expansion

$$M_{\boldsymbol{\nu}}(\delta) = M_{0,\boldsymbol{\nu}} + \sum_{\alpha} \eta_\alpha(\delta) D_{\alpha,\boldsymbol{\nu}} + \cdots .$$

Ordinary radial terms have $\eta_\alpha(\delta) = \delta^k$. A resonant term has $\eta_\alpha(\delta) = \delta^k \log(\delta/\delta_0)$. I reserve $D_{1,\boldsymbol{\nu}}$ for the coefficient of the linear term in δ,

$$D_{1,\boldsymbol{\nu}} = \left.\frac{\mathrm{d}M_{\boldsymbol{\nu}}}{\mathrm{d}\delta}\right|_{0^+}.$$

Higher-order and resonant matrices remain separate from D_1.

The physical origin of D_1 is fixed before any statistical average is taken. Let e_a be fixed coordinates in the reduced endpoint space and let

$$\Psi_a = \mathfrak{J}_0 e_a$$

be their stationary endpoint extensions. Differentiating the complete reduced quadratic form gives

$$\begin{aligned}(D_{1,\boldsymbol{\nu}})_{ab} &= \int_{\mathcal{M}} \mathrm{d}\mu(x)\, \mathcal{I}_{1,ab}(x) + (D_1^{\partial})_{ab}, \\ \mathcal{I}_{1,ab} &= \dot{\Psi}_a^{\dagger} A_1 \dot{\Psi}_b + \dot{\Psi}_a^{\dagger} B_1 \Psi_b \\ &\quad + \Psi_a^{\dagger} B_1^{\dagger} \dot{\Psi}_b + \Psi_a^{\dagger} C_1 \Psi_b.\end{aligned} \tag{E.1}$$

For the radial formulation, $\mathrm{d}\mu = \mathrm{d}\tau$ with the radial weights already included in A_1, B_1, C_1. The integral covers the complete solved region. The term D_1^{∂} contains the derivative of the physical boundary form and the contributions induced by a varying boundary basis.

The stationary extensions already include the response of fields eliminated by their equations of motion. Their first variations therefore produce no additional relaxation term in Eq. (E.1). Any inner–outer decomposition must sum back to the same physical matrix D_1.

I now specify the fixed-charge microscopic ensemble. Let $\mathbb{E}_{\boldsymbol{\nu}}$ denote its normalized expectation and define

$$\overline{D}_{1,\boldsymbol{\nu}} = \mathbb{E}_{\boldsymbol{\nu}} D_{1,\boldsymbol{\nu}}, \qquad \Xi_{\boldsymbol{\nu}} = D_{1,\boldsymbol{\nu}} - \overline{D}_{1,\boldsymbol{\nu}}. \tag{E.2}$$

For a Hermitian reduced matrix, the entry covariance is

$$\mathcal{C}_{\boldsymbol{\nu};ab,cd} = \mathbb{E}_{\boldsymbol{\nu}} \left[(\Xi_{\boldsymbol{\nu}})_{ab} \overline{(\Xi_{\boldsymbol{\nu}})_{cd}} \right]. \tag{E.3}$$

The covariance need not be isotropic.

The endpoint matrix and its finite-radius deformation are generated by the same microscopic data. Their joint connected generator is

$$\mathcal{W}_{\boldsymbol{\nu}}^{\mathrm{joint}}[J_0, J_1] = \log \mathbb{E}_{\boldsymbol{\nu}} \exp\left[i\mathrm{Tr}(J_0 M_{0,\boldsymbol{\nu}}) + i\mathrm{Tr}(J_1 D_{1,\boldsymbol{\nu}}) \right]. \tag{E.4}$$

Mixed derivatives with respect to J_0 and J_1 measure correlations between the endpoint matrix and its deformation. Replacing their joint law by independent samples removes precisely these mixed cumulants.

Equation (E.1) also gives the covariance in terms of the local response density. Taking the connected covariance of the complete expression gives

$$\begin{aligned}\mathcal{C}_{\boldsymbol{\nu};ab,cd} = &\int_{\mathcal{M}^2} \mathrm{d}\mu(x)\mathrm{d}\mu(y)\, \left\langle \mathcal{I}_{1,ab}(x) \overline{\mathcal{I}_{1,cd}(y)} \right\rangle_c \\ &+ \mathcal{C}^{\partial}_{\boldsymbol{\nu};ab,cd}.\end{aligned} \tag{E.5}$$

Here $\mathcal{C}^{\partial}$ collects every term containing D_1^{∂}: the boundary–boundary covariance and the two bulk–boundary cross covariances. If the stationary extensions Ψ_a fluctuate under the microscopic measure, those fluctuations are part of $\mathcal{I}_1$. The required input is therefore the joint law of the bulk coefficients, boundary data, and stationary extensions.

I next state a sufficient regime in which the deformation matrix itself approaches a Gaussian matrix law. Suppose

$$\Xi_{\boldsymbol{\nu}} = \frac{1}{\sqrt{L}} \sum_{\alpha=1}^{L} X_{\boldsymbol{\nu}}^{(\alpha)}, \qquad \mathbb{E} X_{\boldsymbol{\nu}}^{(\alpha)} = 0. \tag{E.6}$$

For an independent triangular array, require convergence of the covariance for every fixed finite set of real matrix coordinates and the Lindeberg condition

$$\frac{1}{L}\sum_{\alpha=1}^{L}\mathbb{E}\left[\left\|X_{\boldsymbol{\nu}}^{(\alpha)}\right\|_F^2\,\mathbf{1}_{\{\left\|X_{\boldsymbol{\nu}}^{(\alpha)}\right\|_F>\epsilon\sqrt{L}\}}\right]\longrightarrow 0\qquad(\epsilon>0).\tag{E.7}$$

Then every fixed finite collection of matrix entries obeys the ordinary multivariate central limit theorem.

For independent identically distributed contributions with finite connected moments,

$$\begin{aligned}&\left\langle(\Xi_{\boldsymbol{\nu}})_{a_1b_1}\cdots(\Xi_{\boldsymbol{\nu}})_{a_pb_p}\right\rangle_c\\&\quad=L^{1-p/2}\left\langle(X_{\boldsymbol{\nu}}^{(1)})_{a_1b_1}\cdots(X_{\boldsymbol{\nu}}^{(1)})_{a_pb_p}\right\rangle_c.\end{aligned}\tag{E.8}$$

Thus all connected cumulants with $p\geq 3$ vanish as $L\to\infty$.

The same scaling extends to sufficiently weakly correlated contributions. For every fixed set of matrix coordinates, impose

$$\sup_{\alpha_1}\sum_{\alpha_2,\ldots,\alpha_p}\left|\kappa_p\left((X^{(\alpha_1)})_{a_1b_1},\ldots,(X^{(\alpha_p)})_{a_pb_p}\right)\right|\leq C_p,\qquad p\geq 2,\tag{E.9}$$

with C_p independent of L. The sum over α_1 then contributes one factor of L, while the normalization in Eq. (E.6) contributes $L^{-p/2}$. Hence the p-th cumulant is $O(L^{1-p/2})$. Together with tightness and moment determinacy, these bounds give the same finite-coordinate Gaussian limit. A dominant contribution or a non-summable long-range correlation lies outside this regime.

The fixed-charge ensemble and variation across different charge sectors are distinct statistical operations. Different sectors may nevertheless share the same compactification data. Their joint microscopic law therefore contains the cross covariance

$$\mathcal{C}_{\boldsymbol{\nu},\boldsymbol{\mu};ab,cd}=\mathbb{E}\left[(\Xi_{\boldsymbol{\nu}})_{ab}\overline{(\Xi_{\boldsymbol{\mu}})_{cd}}\right].\tag{E.10}$$

These cross-sector correlations retain information that is lost if each charge sector is sampled independently.

I also consider variation across a finite shell in the charge lattice. This is a second ensemble, distinct from $\mathbb{E}_{\boldsymbol{\nu}}$. Let

$$G_q=L_q^TL_q,\qquad \boldsymbol{q}=L_q\boldsymbol{\nu},$$

and define

$$\mathcal{S}_{R,\Delta}=\left\{\boldsymbol{\nu}\in\mathbb{Z}^r:R^2-\Delta\leq\boldsymbol{\nu}^TG_q\boldsymbol{\nu}\leq R^2+\Delta\right\}.\tag{E.11}$$

This is an equal-action shell only when the classical action depends on the same quadratic invariant. The product model generally does not satisfy that condition.

For a local quadratic approximation in $\boldsymbol{q}$, write

$$D_1(\boldsymbol{q})=D_0+\sum_{i,j}q_iq_jX_{ij},\qquad X_{ij}=X_{ji}.\tag{E.12}$$

The continuum approximation replaces the lattice shell by the sphere $S^{r-1}(R)$. Using

$$\mathbb{E}q_iq_j=\frac{R^2}{r}\delta_{ij},$$

one obtains

$$\mathbb{E}_{S^{r-1}(R)}D_1=D_0+\frac{R^2}{r}\sum_i X_{ii}.\tag{E.13}$$

The fourth moment

$$\mathbb{E}q_iq_jq_kq_l = \frac{R^4}{r(r+2)}\left(\delta_{ij}\delta_{kl} + \delta_{ik}\delta_{jl} + \delta_{il}\delta_{jk}\right)$$

gives

$$\mathrm{Cov}_{S^{r-1}(R)}(D_1) = \frac{2R^4}{r(r+2)}\left[\sum_{i,j} X_{ij} \otimes \overline{X_{ij}} - \frac{1}{r}\left(\sum_i X_{ii}\right) \otimes \overline{\left(\sum_j X_{jj}\right)}\right]. \tag{E.14}$$

The finite lattice-shell moments are instead exact finite sums over $\mathcal{S}_{R,\Delta}$. They measure variation across charge sectors. They are not the fixed-charge microscopic covariance in Eq. (E.3).

Under the finite-coordinate convergence assumptions above, $\Xi_{\boldsymbol{\nu}}$ approaches a centered Gaussian matrix in every fixed finite collection of entries. For a fixed Hermitian test matrix J,

$$\log \mathbb{E}_{\boldsymbol{\nu}} \exp\left(i\mathrm{Tr}J\Xi_{\boldsymbol{\nu}}\right) = -\frac{1}{2}\mathfrak{C}_{\boldsymbol{\nu}}[J,J] + o(1), \tag{E.15}$$

where $\mathfrak{C}_{\boldsymbol{\nu}}[J,J]$ is the variance of $\mathrm{Tr}(J\Xi_{\boldsymbol{\nu}})$ obtained by contracting Eq. (E.3) with J. The covariance remains anisotropic unless the microscopic ensemble supplies an additional invariance.

This Gaussian limit concerns finitely many matrix coordinates. It does not imply independence from $M_{0,\boldsymbol{\nu}}$, unitary invariance, or a large-matrix spectral law. The mixed cumulants in Eq. (E.4) remain part of the endpoint problem. A growing-matrix limit therefore requires a separate joint spectral analysis of M_0 and its finite-radius deformation.

E.2 Large-matrix limit and spectral correlations

The finite-coordinate Gaussian limit of the preceding subsection does not determine a growing-matrix spectral law. Two distinct large-matrix regimes arise. In the first, the retained block grows with m and requires a matrix-scale normalization and a joint local law. In the second, the external block remains finite while the internal bulk dimension diverges.

The Gaussian matrix in the representation $M_{0,\boldsymbol{\nu}} = Z_{\boldsymbol{\nu}}^\dagger Z_{\boldsymbol{\nu}}$ has entries of order one. Its bulk eigenvalues are therefore of order m. Define

$$\widetilde{Z}_{\boldsymbol{\nu}} = m^{-1/2} Z_{\boldsymbol{\nu}}, \qquad \widetilde{M}_{0,\boldsymbol{\nu}} = m^{-1} M_{0,\boldsymbol{\nu}}. \tag{E.16}$$

Then

$$\widetilde{M}_{0,\boldsymbol{\nu}} = \widetilde{Z}_{\boldsymbol{\nu}}^\dagger \widetilde{Z}_{\boldsymbol{\nu}}.$$

For the linear finite-radius deformation write

$$\widetilde{M}_{\boldsymbol{\nu}}(\delta) = \widetilde{M}_{0,\boldsymbol{\nu}} + \delta \widetilde{D}_{1,\boldsymbol{\nu}} + O(\delta^2), \qquad \widetilde{D}_{1,\boldsymbol{\nu}} = m^{-1} D_{1,\boldsymbol{\nu}}. \tag{E.17}$$

Decompose

$$\widetilde{D}_{1,\boldsymbol{\nu}} = \overline{\widetilde{D}}_{1,\boldsymbol{\nu}} + \widetilde{\Xi}_{\boldsymbol{\nu}}, \qquad \mathbb{E}_{\boldsymbol{\nu}}\widetilde{\Xi}_{\boldsymbol{\nu}} = 0.$$

The dense regime considered here assumes centered entries of $\widetilde{\Xi}_{\boldsymbol{\nu}}$ of order $m^{-1/2}$, bounded rescaled moments, and sufficiently weak correlations. These assumptions are stronger than the finite-coordinate central limit assumptions of the preceding subsection.

The sample-covariance structure has the exact Hermitian linearization

$$\widetilde{\mathbb{B}}_{\boldsymbol{\nu}}(z) = \begin{pmatrix} \delta\overline{\widetilde{D}}_{1,\boldsymbol{\nu}} + \delta\widetilde{\Xi}_{\boldsymbol{\nu}} - z\boldsymbol{I}_m & \widetilde{Z}_{\boldsymbol{\nu}}^{\dagger} \\ \widetilde{Z}_{\boldsymbol{\nu}} & -\boldsymbol{I}_{m+\kappa} \end{pmatrix}. \tag{E.18}$$

Taking the Schur complement of the lower-right block gives

$$[\widetilde{\mathbb{B}}_{\boldsymbol{\nu}}(z)^{-1}]_{11} = \left[\widetilde{M}_{0,\boldsymbol{\nu}} + \delta\widetilde{D}_{1,\boldsymbol{\nu}} - z\boldsymbol{I}_m\right]^{-1}. \tag{E.19}$$

Thus the upper-left block of the linearized resolvent is exactly the resolvent of the normalized reduced matrix.

The two hard-edge normalizations are now explicit. For fixed κ,

$$\lambda_{\min}(M_{0,\boldsymbol{\nu}}) = O(m^{-1}),$$

whereas

$$\lambda_{\min}(\widetilde{M}_{0,\boldsymbol{\nu}}) = O(m^{-2}).$$

The first scale is the one used in the fixed-rank formulas of Section D.2. The second is the microscopic hard-edge scale of the normalized sample-covariance matrix.

To state a matrix Dyson equation, separate deterministic and centered parts:

$$\widetilde{\mathbb{B}}_{\boldsymbol{\nu}}(z) = \widetilde{\mathbb{A}}_{\boldsymbol{\nu}}(z) + \widetilde{\mathbb{X}}_{\boldsymbol{\nu}},$$

with

$$\widetilde{\mathbb{A}}_{\boldsymbol{\nu}}(z) = \begin{pmatrix} \delta\overline{\widetilde{D}}_{1,\boldsymbol{\nu}} - z\boldsymbol{I}_m & 0 \\ 0 & -\boldsymbol{I}_{m+\kappa} \end{pmatrix},$$

and

$$\widetilde{\mathbb{X}}_{\boldsymbol{\nu}} = \begin{pmatrix} \delta\widetilde{\Xi}_{\boldsymbol{\nu}} & \widetilde{Z}_{\boldsymbol{\nu}}^{\dagger} \\ \widetilde{Z}_{\boldsymbol{\nu}} & 0 \end{pmatrix}.$$

The joint distribution of $\widetilde{Z}_{\boldsymbol{\nu}}$ and $\widetilde{\Xi}_{\boldsymbol{\nu}}$ must be retained. Define the covariance operator

$$\widetilde{\mathbb{S}}_{\boldsymbol{\nu}}[R] = \mathbb{E}_{\boldsymbol{\nu}}\left[\widetilde{\mathbb{X}}_{\boldsymbol{\nu}} R \widetilde{\mathbb{X}}_{\boldsymbol{\nu}}\right]. \tag{E.20}$$

Assume that this correlated block ensemble satisfies a local law and that the associated self-consistent solution is stable on the spectral domain under consideration. The deterministic approximation then obeys

$$-\widetilde{\mathbb{G}}_{\boldsymbol{\nu}}(z)^{-1} = -\widetilde{\mathbb{A}}_{\boldsymbol{\nu}}(z) + \widetilde{\mathbb{S}}_{\boldsymbol{\nu}}[\widetilde{\mathbb{G}}_{\boldsymbol{\nu}}(z)]. \tag{E.21}$$

The hypotheses required for such matrix Dyson equations are given in Refs. [21, 22]. The present linearization is bipartite: its lower-right block is deterministic and the covariance operator is degenerate in the same sense as for ordinary sample-covariance matrices. Correlations between $\widetilde{Z}_{\boldsymbol{\nu}}$ and $\widetilde{\Xi}_{\boldsymbol{\nu}}$ add further covariance channels and must enter the same local-law estimate.

The undeformed central Gaussian ensemble provides a normalization check. Set

$$c_{\mathrm{asp}} = \frac{m+\kappa}{m}.$$

In the convention of Eq. (D.17),

$$\mathbb{E}|\widetilde{Z}_{ia}|^2 = \frac{2}{m}.$$

For the isotropic solution write the two diagonal blocks of $\widetilde{\mathbb{G}}$ as

$$m_1 \boldsymbol{I}_m, \qquad m_2 \boldsymbol{I}_{m+\kappa}.$$

Equation (E.21) becomes

$$-m_1^{-1} = z + 2c_{\mathrm{asp}} m_2, \qquad -m_2^{-1} = 1 + 2m_1. \tag{E.22}$$

Eliminating m_2 gives

$$2z m_1^2 + [z - 2(c_{\mathrm{asp}} - 1)] m_1 + 1 = 0. \tag{E.23}$$

The physical branch satisfies

$$m_1(z) \sim -\frac{1}{z}$$

at large z and $\operatorname{Im} m_1(z) > 0$ for $\operatorname{Im} z > 0$. For fixed κ, $c_{\mathrm{asp}} \to 1$, and the limiting bulk support is

$$[0, 8]$$

in this variance convention. This check fixes the normalization of the linearization.

I next extract two observables from the large-matrix law. Let $\widetilde{\rho}_{\boldsymbol{\nu},\delta}$ denote the limiting empirical spectral density of $\widetilde{M}_{\boldsymbol{\nu}}(\delta)$. Assume uniform integrability of $\log|\lambda|$ for the two spectral measures. Then

$$\begin{aligned} \frac{1}{m} \log \left| \frac{\det M_{\boldsymbol{\nu}}(\delta)}{\det M_{0,\boldsymbol{\nu}}} \right| &= \frac{1}{m} \log \left| \frac{\det \widetilde{M}_{\boldsymbol{\nu}}(\delta)}{\det \widetilde{M}_{0,\boldsymbol{\nu}}} \right| \\ &\longrightarrow \int \log|\lambda| \, \widetilde{\rho}_{\boldsymbol{\nu},\delta}(\lambda) \mathrm{d}\lambda \\ &\quad - \int \log|\lambda| \, \widetilde{\rho}_{\boldsymbol{\nu},0}(\lambda) \mathrm{d}\lambda. \end{aligned} \tag{E.24}$$

The logarithmic integrability assumption is essential at the hard edge.

For the source response, define

$$\widetilde{\mathbf{b}}_{\boldsymbol{\nu}}^{\mathrm{eff}} = m^{-1/2} \mathbf{b}_{\boldsymbol{\nu}}^{\mathrm{eff}}.$$

Then the normalization is exact:

$$(\mathbf{b}_{\boldsymbol{\nu}}^{\mathrm{eff}})^\dagger M_{\boldsymbol{\nu}}^{-1} \mathbf{b}_{\boldsymbol{\nu}}^{\mathrm{eff}} = (\widetilde{\mathbf{b}}_{\boldsymbol{\nu}}^{\mathrm{eff}})^\dagger \widetilde{M}_{\boldsymbol{\nu}}^{-1} \widetilde{\mathbf{b}}_{\boldsymbol{\nu}}^{\mathrm{eff}}.$$

Under the corresponding anisotropic local law,

$$(\widetilde{\mathbf{b}}_{\boldsymbol{\nu}}^{\mathrm{eff}})^\dagger \widetilde{M}_{\boldsymbol{\nu}}(\delta)^{-1} \widetilde{\mathbf{b}}_{\boldsymbol{\nu}}^{\mathrm{eff}} \longrightarrow (\widetilde{\mathbf{b}}_{\boldsymbol{\nu}}^{\mathrm{eff}})^\dagger [\widetilde{\mathbb{G}}_{\boldsymbol{\nu}}(0)]_{11} \widetilde{\mathbf{b}}_{\boldsymbol{\nu}}^{\mathrm{eff}}, \tag{E.25}$$

whenever $z = 0$ belongs to a stable domain of the local law. If zero lies at the hard edge, one must retain a spectral regulator and control its removal with an edge local law and the inverse-moment bounds of Section D.2. A bulk local law alone does not determine the inverse exactly at the hard edge.

The large-m limit above keeps the retained block itself macroscopic. A different spectral regime arises when the external dimension is held fixed while a large internal block is eliminated. This second limit produces a finite-dimensional reaction matrix rather than a hard-edge sample-covariance law.

Let the external dimension be m and the internal dimension be N. At a real spectral parameter z, write

$$\mathcal{H}_{\boldsymbol{\nu}}(z) = \begin{pmatrix} H_{\boldsymbol{\nu},\mathrm{ext}} - z\boldsymbol{I}_m & \Gamma_{\boldsymbol{\nu}}^\dagger \\ \Gamma_{\boldsymbol{\nu}} & H_{\boldsymbol{\nu},\mathrm{int}} - z\boldsymbol{I}_N \end{pmatrix}. \tag{E.26}$$

Eliminating the internal block gives

$$M_{\boldsymbol{\nu}}(z) = H_{\boldsymbol{\nu},\mathrm{ext}} - z\boldsymbol{I}_m - \Gamma_{\boldsymbol{\nu}}^{\dagger}(H_{\boldsymbol{\nu},\mathrm{int}} - z\boldsymbol{I}_N)^{-1}\Gamma_{\boldsymbol{\nu}}. \tag{E.27}$$

Define the internal reaction matrix

$$R_{\boldsymbol{\nu}}(z) = \Gamma_{\boldsymbol{\nu}}^{\dagger}(z\boldsymbol{I}_N - H_{\boldsymbol{\nu},\mathrm{int}})^{-1}\Gamma_{\boldsymbol{\nu}}. \tag{E.28}$$

Then

$$M_{\boldsymbol{\nu}}(z) = H_{\boldsymbol{\nu},\mathrm{ext}} - z\boldsymbol{I}_m + R_{\boldsymbol{\nu}}(z).$$

The same Schur complement gives

$$\det \mathcal{H}_{\boldsymbol{\nu}}(z) = \det(H_{\boldsymbol{\nu},\mathrm{int}} - z\boldsymbol{I}_N) \det M_{\boldsymbol{\nu}}(z), \tag{E.29}$$

and

$$[\mathcal{H}_{\boldsymbol{\nu}}(z)^{-1}]_{\mathrm{ext,ext}} = M_{\boldsymbol{\nu}}(z)^{-1}. \tag{E.30}$$

The matrix-Cauchy law belongs to this second, bulk regime. Consider the unitary equivalent-channel ensemble of Ref. [18]. Take $N \to \infty$ at fixed external dimension m and evaluate z at a point where the internal limiting density is positive. After centering and scaling the reaction matrix, its limiting density is

$$\mathcal{P}(R) \propto \det\left[\lambda_{\mathrm{C}}^2 \boldsymbol{I}_m + (R - \epsilon_{\mathrm{C}}\boldsymbol{I}_m)^2\right]^{-m}, \qquad \lambda_{\mathrm{C}} > 0. \tag{E.31}$$

The center ϵ_{C} and width λ_{C} are fixed by the internal spectral density and the channel coupling.

This distribution is a bulk reaction-matrix law. It is distinct from the BPS hard-edge ensemble in Eq. (D.22). The latter describes small positive eigenvalues of an endpoint square. Equation (E.31) instead describes the response of finitely many channels to a large internal spectrum at a point of positive bulk density.

Define the centered and rescaled reaction matrix

$$\widetilde{R} = \frac{R - \epsilon_{\mathrm{C}}\boldsymbol{I}_m}{\lambda_{\mathrm{C}}}. \tag{E.32}$$

Its Cayley transform is

$$\mathcal{U} = (\boldsymbol{I}_m - i\widetilde{R})(\boldsymbol{I}_m + i\widetilde{R})^{-1}. \tag{E.33}$$

Equivalently,

$$\mathcal{U} = [\lambda_{\mathrm{C}}\boldsymbol{I}_m - i(R - \epsilon_{\mathrm{C}}\boldsymbol{I}_m)][\lambda_{\mathrm{C}}\boldsymbol{I}_m + i(R - \epsilon_{\mathrm{C}}\boldsymbol{I}_m)]^{-1}.$$

Since $\widetilde{R}$ is Hermitian, $\mathcal{U}$ is unitary. If x_a are the eigenvalues of $\widetilde{R}$ and $\mathrm{e}^{i\theta_a}$ are the corresponding eigenvalues of $\mathcal{U}$, then

$$x_a = -\tan\frac{\theta_a}{2}.$$

Under this change of variables, the eigenvalue density generated by

$$\det(\boldsymbol{I}_m + \widetilde{R}^2)^{-m}$$

becomes the circular-unitary eigenvalue density. The full unitarily invariant matrix-Cauchy measure therefore maps to Haar measure on $U(m)$.

The Cayley map makes the angular structure of the bulk response explicit, but it does not supply correlations between different charge sectors. To apply the bulk reaction-matrix law across the charge lattice one needs the full family

$$\boldsymbol{\nu} \longmapsto (H_{\boldsymbol{\nu},\mathrm{int}}, \Gamma_{\boldsymbol{\nu}}, H_{\boldsymbol{\nu},\mathrm{ext}})\,. \tag{E.34}$$

For each sector,

$$R_{\boldsymbol{\nu}}(z) = \Gamma_{\boldsymbol{\nu}}^{\dagger}(z\boldsymbol{I}_N - H_{\boldsymbol{\nu},\mathrm{int}})^{-1}\Gamma_{\boldsymbol{\nu}}.$$

The joint law must retain correlations of the internal operators, channel couplings, external subspaces, and charge dependence. Equation (E.31) supplies a one-sector marginal under the stated bulk assumptions. It does not determine the joint charge-sector law.

The two large-matrix limits therefore probe different structures. The normalized Wishart problem resolves the BPS hard edge and its finite-radius deformation. The fixed-channel reaction-matrix problem resolves a bulk internal spectrum and maps its Hermitian response to a compact unitary variable. Combining charge dependence with either spectral regime requires their joint microscopic law rather than independent sampling of the charge weights, endpoint matrices, and response matrices.

F Finite matrix identities

The identities in this section are finite-dimensional algebraic statements. Their continuum use requires the common operator domains, measures, regulators, and determinant prescription of Appendix B.

I begin with bosonic block elimination. Let

$$H = \begin{pmatrix} A & B \\ C & D \end{pmatrix}, \qquad D \text{ invertible}, \qquad M = A - BD^{-1}C. \tag{F.1}$$

No Hermiticity assumption is needed for the following factorization:

$$H = \begin{pmatrix} I & BD^{-1} \\ 0 & I \end{pmatrix} \begin{pmatrix} M & 0 \\ 0 & D \end{pmatrix} \begin{pmatrix} I & 0 \\ D^{-1}C & I \end{pmatrix}. \tag{F.2}$$

Both triangular matrices have determinant one. Hence

$$\det H = \det D \, \det M. \tag{F.3}$$

If M is also invertible, inversion of Eq. (F.2) gives

$$H^{-1} = \begin{pmatrix} M^{-1} & -M^{-1}BD^{-1} \\ -D^{-1}CM^{-1} & D^{-1} + D^{-1}CM^{-1}BD^{-1} \end{pmatrix}. \tag{F.4}$$

Split a row source and a column source according to the same block decomposition,

$$x^{\dagger} = (x_P^{\dagger}, x_Q^{\dagger}), \qquad y = \begin{pmatrix} y_P \\ y_Q \end{pmatrix}.$$

Equation (F.4) then gives

$$\begin{aligned} x^{\dagger}H^{-1}y = {} & x_Q^{\dagger}D^{-1}y_Q \\ & + \left(x_P^{\dagger} - x_Q^{\dagger}D^{-1}C\right) M^{-1} \left(y_P - BD^{-1}y_Q\right). \end{aligned} \tag{F.5}$$

For Hermitian H, the left effective source is the Hermitian conjugate of the right effective source. For a general complex bilinear problem, the ordered row and column in Eq. (F.5) remain distinct.

The same structure follows directly from a bosonic Gaussian integral. Take H real symmetric and positive and write the variables as (x, u). With linear source

$$\sum_i J_i \left(b_{i,P}^T x + b_{i,Q}^T u\right),$$

define

$$\widetilde{u} = u + D^{-1}Cx - D^{-1}\sum_i J_i b_{i,Q}. \tag{F.6}$$

Completing the square separates the complementary Gaussian. Its integration produces the factor

$$(\det D)^{-1/2},$$

and leaves the Schur complement

$$M = A - BD^{-1}C.$$

The source coupled to the retained variable becomes

$$b^{\text{eff}}_{i,P} = b_{i,P} - BD^{-1}b_{i,Q}, \tag{F.7}$$

while the eliminated block produces the direct source response

$$G^{ij}_Q = b^T_{i,Q}D^{-1}b_{j,Q}. \tag{F.8}$$

The remaining Gaussian contributes

$$(\det M)^{-1/2}$$

and the retained response

$$(b^{\text{eff}}_{i,P})^T M^{-1} b^{\text{eff}}_{j,P}. \tag{F.9}$$

Thus the complementary determinant, effective source, and contact response arise from one Gaussian elimination and must be retained together.

With normalized Lebesgue measure

$$\frac{\mathrm{d}^n x}{(2\pi)^{n/2}},$$

the standard Gaussian contains no additional powers of 2π. A different measure carries its normalization explicitly. Under contour continuation, the quadratic form and its source are continued together.

I next record the fermionic analogue. Let

$$\mathcal{D} = \begin{pmatrix} A & B \\ -B^T & D \end{pmatrix}, \qquad A^T = -A, \qquad D^T = -D, \qquad M_F = A + BD^{-1}B^T, \tag{F.10}$$

where both antisymmetric diagonal blocks have even dimension and D is invertible. Define

$$\mathcal{T} = \begin{pmatrix} I & 0 \\ D^{-1}B^T & I \end{pmatrix}. \tag{F.11}$$

Direct multiplication gives

$$\mathcal{T}^T\mathcal{D}\,\mathcal{T} = \begin{pmatrix} M_F & 0 \\ 0 & D \end{pmatrix}, \qquad \det\mathcal{T} = 1. \tag{F.12}$$

Using

$$\mathrm{Pf}(\mathcal{T}^T\mathcal{D}\,\mathcal{T}) = \det\mathcal{T}\,\mathrm{Pf}\mathcal{D}$$

therefore gives

$$\mathrm{Pf}\mathcal{D} = \mathrm{Pf}M_F\,\mathrm{Pf}D. \tag{F.13}$$

The Berezin orientation is fixed by this ordered block decomposition. Extracted exact modes retain their own insertion and measure factors. Equations (A.28), (A.29), and (A.33) are the determinant, Pfaffian, and source identities on the compatible reduced spaces.

Finally, let $K(\delta)$ be an invertible differentiable finite matrix. Differentiating $KK^{-1} = I$ gives

$$\partial_\delta K^{-1} = -K^{-1}(\partial_\delta K)K^{-1}. \tag{F.14}$$

Differentiating the determinant gives

$$\partial_\delta \log\det K = \mathrm{Tr}\big(K^{-1}\partial_\delta K\big)\,. \tag{F.15}$$

For an invertible antisymmetric matrix $\mathcal{D}(\delta)$ on a fixed Pfaffian branch,

$$\partial_\delta \log \mathrm{Pf}\mathcal{D} = \frac{1}{2}\mathrm{Tr}\big(\mathcal{D}^{-1}\partial_\delta \mathcal{D}\big)\,. \tag{F.16}$$

These identities give the matrix derivatives used in Appendices B and D.

References

[1] S.-J. Rey, "Type IIB Axion–Dilaton Wormholes and the BPS Limit Hessian," arXiv:2607.01221 [hep-th] (2026).

[2] S.-J. Rey, "Charge-Sector Construction of the Type-IIB Axion–Dilaton Wormhole Partition Function," arXiv:2607.05385 [hep-th] (2026).

[3] S.-J. Rey, "The Chiral Random-Matrix Ensemble of the Type-IIB Axion–Dilaton Wormhole Partition Function," arXiv:2607.06566 [hep-th] (2026).

[4] A. Kehagias, and A. Riotto, "Scalar Gauss-Bonnet Wormholes and the Imaginary Distance Bound." arXiv preprint arXiv:2609.28456 [hep-th] (2026).

[5] S.-J. Rey, "The Confining Phase of Superstrings and Axionic Strings," Phys. Rev. D **43** (1991) 526–538.

[6] T. Hertog, M. Trigiante, and T. Van Riet, "Axion Wormholes in AdS Compactifications," JHEP **06** (2017) 067, arXiv:1702.04622 [hep-th].

[7] T. Cheon and T. Shigehara, "Scale Anomaly and Quantum Chaos in the Billiards with Pointlike Scatterers," Phys. Rev. E **54** (1996) 3300–3303, arXiv:hep-th/9512162.

[8] H. E. Camblong and C. R. Ordóñez, "Anomaly in conformal quantum mechanics: From molecular physics to black holes," Phys. Rev. D **68** (2003) 125013, arXiv:hep-th/0303166.

[9] I. Tsutsui, T. Fülöp, and T. Cheon, "Connection Conditions and the Spectral Family under Singular Potentials," J. Phys. A **36** (2003) 275–287, arXiv:quant-ph/0209110.

[10] N. Reshetikhin and B. Vertman, "Combinatorial Quantum Field Theory and Gluing Formula for Determinants," Lett. Math. Phys. **105** (2015) 309–340, arXiv:1403.6170.

[11] R. Forman, "Functional determinants and geometry," Invent. Math. **88** (1987) 447–494.

[12] D. Burghelea, L. Friedlander, and T. Kappeler, "Meyer–Vietoris type formula for determinants of elliptic differential operators," J. Funct. Anal. **107** (1992) 34–65; "On the determinant of elliptic boundary value problems on a line segment," Proc. Amer. Math. Soc. **123** (1995) 3027–3038.

[13] M. F. Atiyah, V. K. Patodi, and I. M. Singer, "Spectral Asymmetry and Riemannian Geometry. I," Math. Proc. Cambridge Philos. Soc. **77** (1975) 43–69.

[14] X. Dai and D. S. Freed, "Eta-Invariants and Determinant Lines," J. Math. Phys. **35** (1994) 5155–5194.

[15] A. Altland and M. R. Zirnbauer, "Nonstandard Symmetry Classes in Mesoscopic Normal-Superconducting Hybrid Structures," Phys. Rev. B **55** (1997) 1142–1161.

[16] J. J. M. Verbaarschot and T. Wettig, "Random Matrix Theory and Chiral Symmetry in QCD," Annu. Rev. Nucl. Part. Sci. **50** (2000) 343–410.

[17] H. Leutwyler and A. Smilga, "Spectrum of Dirac operator and role of winding number in QCD," Phys. Rev. D **46** (1992) 5607–5632.

[18] Y. V. Fyodorov, B. A. Khoruzhenko, and A. Nock, "Universal K-matrix distribution in $\beta = 2$ ensembles of random matrices," J. Phys. A **46** (2013) 262001, arXiv:1304.4368 [math-ph].

[19] P. W. Brouwer, "Generalized circular ensemble of scattering matrices for a chaotic cavity with non-ideal leads," Phys. Rev. B **51** (1995) 16878, arXiv:cond-mat/9501025.

[20] K. Życzkowski and H.-J. Sommers, "Truncations of random unitary matrices," J. Phys. A **33** (2000) 2045–2057, arXiv:chao-dyn/9910032.

[21] O. Ajanki, L. Erdős, and T. Krüger, "Stability of the Matrix Dyson Equation and Random Matrices with Correlations," Probab. Theory Relat. Fields **173** (2019) 293–373, arXiv:1604.08188 [math.PR].

[22] L. Erdős, "The Matrix Dyson Equation and Its Applications for Random Matrices," in *Random Matrices*, IAS/Park City Math. Ser. **26** (2019), arXiv:1903.10060 [math-ph].

[23] R. J. Muirhead, *Aspects of Multivariate Statistical Theory*, Wiley, New York (1982), Secs. 3.2–3.3.